



TECHNISCHE
UNIVERSITÄT
WIEN

DISSERTATION

Dynamics of quantum-correlated one-dimensional Bose gases

*ausgeführt zum Zwecke der Erlangung des akademischen Grades eines Doktors
der technischen Wissenschaften*

unter Leitung von

Univ.Prof. Dipl.-Ing. Dr. techn. Hannes-Jörg Schmiedmayer
E141-Atominstitut

eingereicht an der

Fakultät für Physik
Technische Universität Wien

von

M.Sc. Tiantian Zhang

Wien, September 2023

T. Zhang

H.-J. Schmiedmayer

P. Treutlein

O. Hosten

Abstract

Bosonic Josephson junctions (BJJs) have been realised across various platforms and their dynamics have been extensively studied since their first discovery in the 1990s. While prior studies have predominantly delved into the mean-field dynamics of BJJ, we focus on the dynamics of quantum-correlated states in the BJJ with an emphasis on fluctuations. Our specific BJJ involves a pair of one-dimensional (1D) Bose gases trapped in a double well on an atom chip. In order to prepare the many-body system in the strongly quantum-correlated regime, we employ a splitting procedure that protects dynamics in the relative degree of freedom between the two 1D Bose gases from the thermal noises which otherwise dominate over the quantum noises at finite temperatures. Furthermore, we show how to optimise the quantum correlations in the multimode BJJ and demonstrate how the improved correlations prolong the phase coherence in the spatially extended 1D system. Our work provides new ways for engineering correlations and entanglement in the external degree of freedom of interacting many-body systems.

Zusammenfassung

Bosonische Josephson-Kontakte (BJJ) wurden bisher in verschiedensten physikalischen Systemen realisiert und deren Dynamik seit ihrer Entdeckung in den 1990er Jahren eingehend untersucht. Während frühere Studien sich hauptsächlich mit der Betrachtung von Mean-Field Effekten beschäftigten, konzentrieren wir uns auf die Dynamik von quanten-korrelierten Zuständen der BJJ wobei ein Schwerpunkt auf Fluktuationen gesetzt wird. Im speziellen handelt es sich bei unserer BJJ um ein Paar eindimensionaler (1D) Bose-Gase, die auf einem Atom-Chip in einem Double-Well Potential gehalten werden. Um das Quantenvielteilchensystem in einem Regime starker Quantenkorrelationen setzen wir ein Trennungsverfahren ein, das die Dynamik der relativen Freiheitsgrade unseres Systems vor thermischem Rauschen schützt, welches ansonsten bei endlichen Temperaturen das Quanten-Rauschen dominieren würde. Darüber hinaus zeigen wir, wie sich die Quantenkorrelationen im Multimode-BJJ optimieren lassen und wie die so verbesserten Korrelationen zu einer Verlängerung der Phasenkohärenz im räumlich ausgedehnten 1D-System führen. Unsere Arbeit weist neue Wege auf, um gezielt Korrelationen und Verschränkung der externen Freiheitsgrade wechselwirkender Vielteilchensysteme herbeizuführen und deren Dynamik zu untersuchen.

Acknowledgements

I am deeply grateful to my supervisor, Jörg Schmiedmayer, for giving me the opportunity to work in his group and for his support during this PhD thesis. My colleagues for their camaraderie shared challenges, and motivating conversations made this journey both academically rewarding and enjoyable. Completing this journey would not have been possible without the support, encouragement, and contributions of many individuals. While the list is extensive, I would like to express my gratitude to the following:

- My teammates on RbII. A special thanks to Mira Maiwöger who taught me everything about the experiment. Without her devotion to the machine, especially with the vacuum opening, it would not have been up and running again. Maximilian Prüfer for his expertise and for being a super reliable coworker who made my life lots easier in the latter half of my PhD.
- My colleagues who saved me from my misery: Camille Lévêque for being a great friend and big help in setting up the MCTDHB simulation; Amin Tajik (my partner in crime with thesis writing) for his encouraging words when I needed them most; João Sabino for bringing his sweetness (all the way from Lisbon); Andrew Kanagin for being a great listener and all the delish BBQs. Wenzel Kersten (an artist) for offering help with his amazing German skills; Thomas Schweigler for sharing his code and insight about the Fermi experiment; Stephan Schneider for making our everyday life so smooth at ATI.
- RuGway Wu, Maximilian Prüfer, and Sebastian Erne for taking the time to proofread most parts of this thesis and Igor Mazets for his comments on the last chapter.
- My thesis committee members, Onur Hosten and Philipp Treutlein, for their valuable feedback that has contributed to the refinement of this work.

Contents

Abstract	iii
Zusammenfassung	v
Acknowledgements	vii
1 Introduction	1
2 Bose–Einstein condensates in a double well	3
2.1 Generic two-mode model	3
2.1.1 Two-mode Bose-Hubbard model	6
2.1.2 Multi-configurational time-dependent Hartree method for bosons ($M = 2$)	8
2.2 Spin representation	9
2.2.1 Collective spin picture	9
2.2.2 Spin squeezing	9
2.3 1D quasicondensates	11
2.3.1 1D weakly interacting Bose gases	11
2.3.2 Effective field theory	12
2.3.2.1 Single quasicondensates	12
2.3.2.2 Quasicondensates in a double well	15
3 Experimental system and readout	19
3.1 BEC production	19
3.1.1 Experimental sequence	19
3.1.2 Radio frequency dressed double wells	21
3.2 Imaging systems	24
3.2.1 Absorption imaging system	24
3.2.2 Fluorescence imaging system	25
3.3 BECs in double well readout	26
3.3.1 Relative number readout	27
3.3.2 Relative phase readout	29
3.4 Double well characterisation	33
3.4.1 Comparison with trap simulation	33
3.4.2 Symmetric double well calibration	35
3.4.2.1 Double well trap bottom spectroscopy	35
3.4.2.2 Relative imbalance	38
3.4.3 Optimize number squeezing readout	39
3.4.3.1 Optimize kick amplitude	39

3.4.3.2	Optimize imbalance	41
4	Preparation of BECs in double wells	45
4.1	Direct cooling	45
4.2	BEC splitting	49
5	Mean-field dynamics in bosonic Josephson junction	53
5.1	Global Josephson oscillations	53
5.2	Density dependent Josephson oscillations	56
6	Quantum fluctuation dynamics in bosonic Josephson junction	61
6.1	Squeezing oscillations	61
6.2	Simulation on squeezing oscillations	63
6.2.1	Semiclassical two-mode BH	63
6.2.2	MCTDHB simulation	66
6.2.3	Tuning squeezing oscillations	68
6.3	Modulated tunnel coupling	70
6.3.1	Induced interclouds motion	71
6.3.2	Driven squeezing oscillations	72
7	Optimised spin-squeezed states	77
7.1	Optimisation with two-step	77
7.1.1	Two-step with number readout	78
7.1.2	Two-step with phase readout	80
7.2	Suppressed phase diffusion	81
7.3	Protected spatial phase correlations	85
7.3.1	Evolution in decoupled double well	85
7.3.2	Short term dynamics: prethermalisation	87
7.3.3	Long term evolution	93
8	Towards resolving mode dynamics	97
8.1	Effective imaging resolution	97
8.2	Local number squeezing estimation	98
8.3	Local relative density fluctuations	101
8.4	Outlook	103
A	Double well characterisation	105
A.1	Two trap configurations	105
A.2	Double well trap bottom spectroscopy (OCT)	105
B	Induced longitudinal motion	107
	Bibliography	109

*To my family for your immense support and
unconditional love. . .*

Chapter 1

Introduction

The world of quantum physics continually unveils remarkable opportunities to understand fundamental phenomena and develop cutting-edge technologies. Within this landscape, the exploration of quantum-correlated states has captivated us with their distinct quantum behaviours. Since the pioneering experimental achievements [1, 2], squeezed states have been realized in diverse experimental systems, especially with Bose-Einstein condensates (BECs) [3–5]. In particular, spin squeezing [6] has attracted considerable attention due to its implications for enhancing the precision of quantum measurements beyond classical limits. These states hold great promise for quantum metrology [7, 8] and quantum sensing [9] applications, where improved sensitivity is crucial. Employing the controlled interactions within complex many-body systems, spin-squeezed states exhibit enhanced measurement precision, which enables breakthroughs in fields ranging from atomic clocks [10] to gravitational wave detection [11].

The computational challenges posed by simulating the emergent dynamics in complex many-body systems are substantial. Rapidly growing entanglement [12–15] and complex higher-order quantum correlations [16] make such simulations computationally demanding. The introduction of experimental systems as quantum simulators [17–20] offers a novel approach to address these challenges. In this thesis, we intend a structured exploration into the generation and evolution of spin-squeezed states with our experimental framework of 1D Bose gases. Within the limit of our experimental capabilities, we hope to develop some grasp of the relaxation and thermalization processes in a pair of initially correlated 1D quantum gases [16, 21, 22]. This not only enriches our comprehension of complex quantum behaviours but hopefully also paves the way for harnessing these phenomena to advance quantum metrology, quantum sensing, and the broader quantum technology landscape.

We start by experimentally initialising a pair of 1D Bose gases in a double well along the transversal direction, which realises an elongated bosonic Josephson junction [23, 24]. The system can be well described as a generic two-mode model [25], as the system energetically only occupies the two lowest single-particle states (modes). Preparing them by splitting up a single gas into two is a simple yet effective way to engineer correlations between them, in terms of number squeezing [3]. By investigating closely the exact splitting procedure, we

can control the level of imprinted correlations. From here, we make a connection to the inherent multimode nature of the 1D Bose gas and seek agreement with low-energy effective field theories, such as Tomonaga Luttinger Liquid [26–28] and sine-Gordon model [16, 29, 30]. This experimental work intends to bridge the two-mode models at zero temperature and 1D field theories that cover 1D systems at finite temperatures.

The remainder of this thesis is organized as follows:

Chapter 2 provides a brief review of the theoretical foundations of the bosonic Josephson junction and spin squeezing and the framework of one-dimensional Bose gases in the weakly interacting quasicondensate regime and the low-energy field theory models.

Chapter 3 presents the experimental system of 1D BECs trapped in a double well and its readout, including characterization and calibration of symmetric double wells.

Chapter 4 demonstrates two different approaches to the preparation of BECs in a double well with a focus on the resulting noises in the relative degree of freedom of quantum or thermal origins.

Chapter 5 delves into the mean-field dynamics of tunnel-coupled BECs. We explore the frequency scaling in Josephson oscillations of both the global observables and the local observables.

Chapter 6 discusses the observation of oscillatory dynamics of the quantum fluctuations between BECs in double wells with finite tunnel coupling and examines the tunability of these oscillations.

Chapter 7 optimises spin-squeezed states and presents the following dynamics in a decoupled double well as a result of different levels of spin squeezing.

Chapter 8 envisions future directions of investigation built on the current experimental findings.

Chapter 2

Bose–Einstein condensates in a double well

This theory chapter delves into the mathematical framework and models used to understand the rich dynamics of tunnel-coupled Bose-Einstein condensates (BECs) in extended one dimension (1D). We begin by introducing the two-mode models, which provide a simple yet powerful description of the coherent tunnelling dynamics between the two tunnel-coupled BECs. These models allow us to gain valuable insights into Josephson oscillations and later the dynamical evolution of quantum fluctuations observed in the system.

Furthermore, we identify the regime of the 1D interacting Bose gases in the experiment and introduce effective field theory describing the properties of the 1D Bose gases. This theoretical framework provides a good foundation for understanding the emerging dynamics in one-dimensional quasicondensates in double wells.

2.1 Generic two-mode model

The section is dedicated to describing BECs in a double well as a macroscopic coherent system, which only occupy the two lowest single-particle states. This is typically known as the two-mode model ($M = 2$). The finite temperature effect is left out of the picture for now. A good review of the two-mode model can be found in Dalton et al. [25]. This first model is the well-known Bose-Hubbard (BH) model, which focuses on solving Hamiltonian with time-independent orbitals. The second model is the multi-configurational time-dependent Hartree approach for bosons (MCTDHB) [31–33]. MCTDHB is a many-body simulation method that solves the time-dependent Schrödinger equation. Lastly, I will connect to the spin representation and introduce the critical quantities in quantum metrology relevant to understanding the experimental results in this thesis work.

For many body systems of indistinguishable particles, second quantization (field quantization) is a more suitable way to express the quantum state, where only the number of particles occupying a certain quantum state is important. For a

single-component BEC in a double well, the full Hamiltonian is written as

$$\hat{H} = \int d\mathbf{r} \left(\frac{\hbar^2}{2m} \nabla \hat{\Psi}^\dagger \cdot \nabla \hat{\Psi} + \hat{\Psi}^\dagger V \hat{\Psi} + \frac{g}{2} \hat{\Psi}^\dagger \hat{\Psi}^\dagger \hat{\Psi} \hat{\Psi} \right), \quad (2.1)$$

where V is the external trapping potential and g is the coupling constant and when restricted to the s -wave scattering with scattering length a_s is given by

$$g = \frac{4\pi^2 \hbar^2 a_s}{m}. \quad (2.2)$$

In its most general format, the field operator is expressed as

$$\begin{aligned} \hat{\Psi}(\mathbf{r}, t) &= \sum_{i=1}^M \hat{a}_i(t) \psi_i(\mathbf{r}, t), \\ \hat{\Psi}^\dagger(\mathbf{r}, t) &= \sum_{i=1}^M \hat{a}_i^\dagger(t) \psi_i^*(\mathbf{r}, t), \end{aligned} \quad (2.3)$$

where the occupancy $\hat{a}_i(t)$ and modes $\psi_i(\mathbf{r}, t)$ are both time-dependent and fulfill the commutation relations

$$\begin{aligned} \int d\mathbf{r} \psi_i^*(\mathbf{r}, t) \psi_j(\mathbf{r}, t) &= \delta_{ij}, \\ \sum_i \psi_i(\mathbf{r}, t) \psi_i^*(\mathbf{r}', t) &= \delta(\mathbf{r} - \mathbf{r}'), \\ [\hat{a}_i, \hat{a}_j^\dagger] &= \delta_{ij}. \end{aligned} \quad (2.4)$$

A state vector in the complete orthonormal Fock basis of M one-particle wave functions referred to as modes or orbitals (in MCTDHB language), is expressed as

$$\begin{aligned} |\mathbf{n}; t\rangle &= |n_1, n_2, \dots, n_M; t\rangle \\ &= \frac{1}{\sqrt{n_1! n_2! \dots n_M!}} \left(\hat{a}_1^\dagger(t) \right)^{n_1} \left(\hat{a}_2^\dagger(t) \right)^{n_2} \dots \left(\hat{a}_M^\dagger(t) \right)^{n_M} |0\rangle, \end{aligned} \quad (2.5)$$

where $\mathbf{n} = (n_1, n_2, \dots, n_M)$ represents the configuration and $\hat{a}_i(t)^\dagger$ creates a particle in the i th mode. We can then express a pure quantum state as a sum over all configurations of mode occupancy numbers

$$|\Psi(t)\rangle = \sum_{\mathbf{n}} C_{\mathbf{n}}(t) |\mathbf{n}; t\rangle, \quad (2.6)$$

where $C_{\mathbf{n}}$ is the time-dependent coefficient of each configuration. In the case $M \rightarrow \infty$, this expression is exact. However, the computation is then exponentially more expensive. To describe BECs in a double well, as we will introduce in the upcoming subsections, we use up to $M = 2$ modes.

Generally, we can define the p -th order density matrix to extend the representation to include mixed states

$$\rho^{(p)}(\mathbf{r}_1, \mathbf{r}_2, \dots, \mathbf{r}_p | \mathbf{r}'_1, \mathbf{r}'_2, \dots, \mathbf{r}'_p; t) = \frac{N!}{(N-p)!} \int \Psi(\mathbf{r}_1, \mathbf{r}_2, \dots, \mathbf{r}_p, \mathbf{r}_{p+1}, \dots, \mathbf{r}_N; t) \Psi^*(\mathbf{r}'_1, \mathbf{r}'_2, \dots, \mathbf{r}'_p, \mathbf{r}'_{p+1}, \dots, \mathbf{r}'_N; t) d\mathbf{r}_{p+1} \dots d\mathbf{r}_N, \quad (2.7)$$

where the diagonal of the matrix is the p -body probability distribution, and the off-diagonal elements determine the p -th order coherence. Equivalently, we can express it using the wave function in the spatial space $|\Psi(\mathbf{r})\rangle = \langle r | \Psi \rangle$

$$\rho^{(p)}(\mathbf{r}_1, \dots, \mathbf{r}_p | \mathbf{r}'_1, \dots, \mathbf{r}'_p; t) = \langle \Psi(t) | \hat{\Psi}^\dagger(\mathbf{r}'_1) \dots \hat{\Psi}^\dagger(\mathbf{r}'_p) \hat{\Psi}(\mathbf{r}_p) \dots \hat{\Psi}(\mathbf{r}_1) | \Psi(t) \rangle, \quad (2.8)$$

and similarly expressing it with wave function in the momentum space $|\Psi(\mathbf{k})\rangle$. Suppose only a single eigenvalue of the reduced density matrix is macroscopic (significant). In that case, the system can be well described with GPE, and we need only $M = 1$ mode to characterize the quantum mechanical picture of the system. On the other hand, if more than one eigenvalue is macroscopic, the condensates are fragmented [34], and $M > 1$ modes are needed.

From hereon, we assume that BECs in a double well only occupy the two lowest modes, $M = 2$. In the limiting case, where only a single mode is occupied, the system can be described by the mean-field theory ($M = 1$), for instance, the Gross-Pitaevskii equation (GPE). With the two-mode model, one can capture the essential features of many body systems, such as correlations. In addition to tunnel-coupled BECs (single component BEC in double wells), the two-mode model can also describe BEC with two internal states in a single well, such as two-component BEC [4, 35, 36] and spin BECs [5, 37]. In the next, we will delve into two different two-mode models, where the main difference between

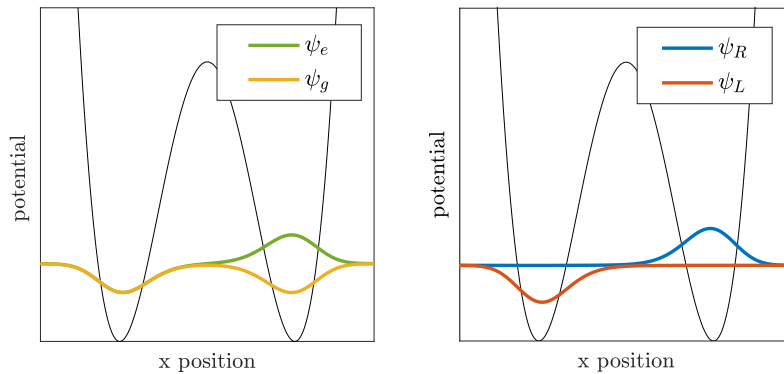


FIGURE 2.1: **Two modes for BEC in a double well** Left panel: two modes constitute of ground state ψ_g and first-excited state ψ_e Right panel: two modes constitute of left-localised state ψ_L and right-localised state ψ_R . They are interconvertible according to Eq. (2.10).

BH and MCTDHB is that the modes ψ_i (in Eq.(2.3)) are time-independent in the Bose-Hubbard model and time-dependent in MCTDHB.

2.1.1 Two-mode Bose-Hubbard model

A widely known two-mode model is the Bose-Hubbard (BH) model [38]. The modes in the BH model are time-independent. The Hamiltonian of a two-mode BH model can then be approximated as

$$\hat{H} = -J(\hat{a}_L^\dagger \hat{a}_R + \hat{a}_R^\dagger \hat{a}_L) + \frac{U}{2} \sum_{i=L,R} \hat{a}_i^\dagger \hat{a}_i^\dagger \hat{a}_i \hat{a}_i, \quad (2.9)$$

where annihilation \hat{a}_i and creation operator \hat{a}_i^\dagger on the spatially localized modes ψ_L and ψ_R in the left and right well respectively

$$\begin{aligned} \psi_L(\mathbf{r}) &= \frac{\psi_g(\mathbf{r}) + \psi_e(\mathbf{r})}{\sqrt{2}}, \\ \psi_R(\mathbf{r}) &= \frac{\psi_g(\mathbf{r}) - \psi_e(\mathbf{r})}{\sqrt{2}}, \end{aligned} \quad (2.10)$$

as a superposition of the single particle ground state Ψ_g and first excited state Ψ_e (see Fig. 2.1). So that the general field operator (defined in Eq. (2.3)) within $M = 2$ mode model (consisting of ψ_L and ψ_R) is expressed

$$\hat{\Psi}(\mathbf{r}) = \hat{a}_L \psi_L(\mathbf{r}) + \hat{a}_R \psi_R(\mathbf{r}). \quad (2.11)$$

The inter-particle interaction energy U and the tunnel coupling energy J is obtained

$$\begin{aligned} U &\equiv 2g \int d^3\mathbf{r} |\psi_L(\mathbf{r})|^2 |\psi_R(\mathbf{r})|^2, \\ J &\equiv \int d^3\mathbf{r} \left[\frac{\hbar^2}{2m} \nabla \psi_L^*(\mathbf{r}) \nabla \psi_R(\mathbf{r}) + \psi_L^*(\mathbf{r}) V(\mathbf{r}) \psi_R(\mathbf{r}) \right], \end{aligned} \quad (2.12)$$

where $V(\mathbf{r})$ is the trapping potential and g is the inter-particle interaction strength. The corresponding Fock basis for solving the two-mode BH Hamiltonian in Eq. (2.9) is

$$\{|N_L, N_R\rangle\}, \text{ where } N_L + N_R = N, \text{ and } N_{L,R} \in [0, N], \quad (2.13)$$

here N_L and N_R represent the atom number in each of the spatial modes and the total atom number N is conserved. To achieve a semiclassical mean-field approximation, we define the creation and annihilation operators for each mode as follows [39]

$$\hat{a}_i = \sqrt{\hat{N}_i} e^{i\hat{\Phi}_i}, \quad (2.14)$$

$$\hat{a}_i^\dagger = e^{-i\hat{\Phi}_i} \sqrt{\hat{N}_i}, \quad (2.15)$$

Here $i = L$ or R for each mode. Conversely, one can express the number operator as

$$\hat{N}_i = \hat{a}_i^\dagger \hat{a}_i \quad (2.16)$$

And the phase operator $\hat{\Phi}_i$ fulfils the commutation relation,

$$[\hat{\Phi}_i, \hat{N}_i] = i, \quad (2.17)$$

where we pick the definition by Dirac, et. al. [40]. Note that the phase operator $\hat{\Phi}$ definition is not very rigorous and breaks down for larger phase fluctuation [41]. The coherent state can be expressed as [42]

$$|\Psi\rangle = \frac{1}{\sqrt{N!}} \left(a_L^\dagger + a_R^\dagger \right)^N |0\rangle, \quad (2.18)$$

with $|0\rangle$ representing the vacuum state. This is an eigenstate for the limiting case where $U = 0$. To derive a more general description, we define the conjugate observables in the relative degree of freedom between two BECs, respectively the relative number, \hat{N}_- , and relative phase, $\hat{\Phi}$, as

$$\hat{N}_- = \hat{N}_L - \hat{N}_R, \quad (2.19)$$

$$\hat{\Phi} = \hat{\Phi}_L - \hat{\Phi}_R. \quad (2.20)$$

Using the convention that

$$\cos \hat{\Phi} = \frac{\exp(i\hat{\Phi}) + \exp(-i\hat{\Phi})}{2}, \quad \text{and} \quad \hat{n} = \frac{\hat{N}_-}{N}, \quad (2.21)$$

we can re-express the BH Hamiltonian in Eq.(2.9) as

$$\hat{H} = -2J\sqrt{1 - \hat{n}^2} \cos \hat{\Phi} + \frac{UN}{4}(1 - \hat{n}^2) - \frac{U}{2}, \quad (2.22)$$

In the continuous limit, $N \rightarrow \infty$, one can omit the last term and treat all operators as classical fields

$$H = -2J\sqrt{1 - n^2} \cos \Phi + \frac{UN}{4}(1 - n^2). \quad (2.23)$$

The time evolution of relative number N_- or relative phase Φ can be computed using the Heisenberg equation of motion

$$-i\hbar \frac{\partial N_-}{\partial t} = [H, N_-], \quad \text{and} \quad -i\hbar \frac{\partial \Phi}{\partial t} = [H, \Phi], \quad (2.24)$$

which is useful to derive mean-field dynamics of experimentally accessible observables in Chpt. 5 and semiclassical simulations in Sec. 6.2.1. Improved two-mode BH models such as including a time-dependent tunnel coupling [43] have been developed. But within the scope of this thesis, only the simplest version of the BH model (Eq. (2.9)) is used.

2.1.2 Multi-configurational time-dependent Hartree method for bosons ($M = 2$)

To capture the full quantum mechanical picture of BECs in double well, in terms of quantifying correlations and coherence, we can consult with two-mode MCTDHB [31–33]. Here modes refer to the single-particle eigenstates. This method is at its core a wavepacket propagation method, which can be broken down into three parts: the initialisation of the wavepacket, the propagation of the wavepacket and the analysis of the wavepacket. MCTDHB method is an efficient many-body simulation method that solves the time-dependent Schrödinger equation using a variational method based on multi-configurational wavefunction ansatz.

With the configured quantum state expressed in Fock basis (Eq.(2.6)), the key for solving the time-dependent Schrödinger equation

$$\hat{H}|\Psi\rangle = i\partial_t|\Psi\rangle, \quad (2.25)$$

is to use Eq.(2.6) as an Ansatz and apply the time-dependent variational method. We define an action functional

$$S = \int dt \left\{ \langle \Psi(t) | \hat{H} - i \frac{\partial}{\partial t} | \Psi(t) \rangle - \sum_{k,j=1}^M \mu_{kj} [\langle \psi_k | \psi_j \rangle - \delta_{kj}] \right\}, \quad (2.26)$$

and look for a stationary S with respect to variation of the coefficients C_n and orbitals ψ_k to allocate the ground state $|\Psi\rangle$ with ensured orthonormal basis.

Within the scope of this thesis, $M = 2$ in Eq. (2.5) is sufficient to capture the physics of a macroscopic bosonic Josephson junction. By picking the two lowest single-particle eigenstates ψ_1 and ψ_2 as the two natural orbitals with opposite parity, we can express the state of a N -body system as

$$|\Psi(t)\rangle = \sum_{i=1}^{N+1} C_i(t) |n_1^i, n_2^i; t\rangle, \quad n_1^i, n_2^i \in [0, N], \quad n_1^i + n_2^i = N. \quad (2.27)$$

To best resemble typical cold atom experimental readout of single shot images, projective measurement can be performed in either real space $|\psi(\mathbf{r}, t)|^2$ or momentum space $|\psi(\mathbf{k}, t)|^2$. More details can be found in a colloquium by A. Lode, et. al. [33]. Correlations can be shown in the variance of operators

$$\Delta \hat{A}^2 = \langle \hat{A}^2 \rangle - \langle \hat{A} \rangle^2, \quad (2.28)$$

which has contributions from the two-body operators. We can apply this to estimate the variance in spatial and momentum space. The correlation is a many-body feature that is ignored in mean-field theories.

2.2 Spin representation

In this section, we introduce concepts in quantum metrology, such as spin squeezing and many-body entanglement. These concepts clarify the main motivation of this thesis work, which is to optimise spin squeezing in BEC in a decoupled double well serving as an input state with the quantum-enhanced sensitivity of an interferometer. The majority of this section is inspired by a review of quantum metrology with nonclassical states [8].

2.2.1 Collective spin picture

To model the tunnel-coupled BECs on the Bloch sphere, we can treat the N -boson system as a collective spin system of $1/2$ spin particles. The total spin angular momentum length is equal to $S = N/2$. The Hamiltonian of the symmetric two-mode BH model in Eq.(2.9) can be re-expressed in the pseudo-spin picture as

$$\hat{H} = U\hat{S}_z^2 - 2J\hat{S}_x, \quad (2.29)$$

where U is the interaction energy, Ω is the coupling energy and the Schwinger pseudo-spin operators are defined as,

$$\hat{S}_x = \frac{1}{2}(\hat{a}_1^\dagger\hat{a}_2 + \hat{a}_2^\dagger\hat{a}_1) \quad (2.30)$$

$$\hat{S}_y = \frac{1}{2i}(\hat{a}_1^\dagger\hat{a}_2 - \hat{a}_2^\dagger\hat{a}_1), \quad (2.31)$$

$$\hat{S}_z = \frac{1}{2}(\hat{a}_1^\dagger\hat{a}_1 - \hat{a}_2^\dagger\hat{a}_2) \quad (2.32)$$

which fulfill the angular momentum commutation relation $[\hat{S}_i, \hat{S}_j] = \epsilon_{ijk}\hat{S}_k$ and commute with $\hat{N} = \hat{a}_1^\dagger\hat{a}_1 + \hat{a}_2^\dagger\hat{a}_2$. Even though \hat{S}_y does not appear in this particular Hamiltonian, but is defined for completeness. \hat{S}_z^2 is a nonlinear term accounting for the atom-atom interaction.

2.2.2 Spin squeezing

The ground state of a bosonic Josephson junction with repulsive interactions, $U > 0$, can be categorized according to the interplay factor [44]

$$\Lambda = \frac{UN}{2J}. \quad (2.33)$$

In the limit $0 < \Lambda \ll 1$, known as the Rabi regime, the ground state of the BJJ is a spin coherent state, $\propto (\hat{a}_1^\dagger + \hat{a}_2^\dagger)^N|0\rangle$, where the binomial occupation of each mode yields

$$(\Delta\hat{S}_y)^2 = (\Delta\hat{S}_z)^2 = \frac{N}{4}. \quad (2.34)$$

This corresponds roughly to the noninteracting case $U = 0$. The phase coherence $\langle\hat{S}_x\rangle \approx N/2$, signifies a well-defined relative phase between the modes. As Λ increases, the number fluctuations between the two modes become less

favourable (due to the preferred minimization of energy). In the limit $\Lambda \gg N^2$, the phase distribution is almost completely uniform, namely wrapped around 2π . The ground state of BJJ approaches the twin Fock state with vanishing number fluctuations ($\Lambda \rightarrow \infty$), which is represented with

$$\begin{aligned} (\hat{a}_1^\dagger)^N (\hat{a}_2^\dagger)^N |0\rangle &= \left| \frac{N}{2}, \frac{N}{2} \right\rangle, \quad \text{with even } N, \\ &= \frac{1}{\sqrt{2}} \left(\left| \frac{N+1}{2}, \frac{N-1}{2} \right\rangle + \left| \frac{N-1}{2}, \frac{N+1}{2} \right\rangle \right), \quad \text{with odd } N. \end{aligned} \quad (2.35)$$

In the Josephson regime $1 \ll \Lambda \ll N^2$, the number and phase fluctuation can be approximated to be

$$\Delta \hat{S}_y^2 \approx \frac{N\sqrt{\Lambda}}{4}, \quad \Delta \hat{S}_z^2 \approx \frac{N}{4\sqrt{\Lambda}}. \quad (2.36)$$

The spin-squeezed state is a class of metrologically useful entangled states. Whereby the metrological spin squeezing factor is defined as [45]

$$\xi_S^2 = \frac{N(\Delta \hat{S}_z)^2}{\langle \hat{S}_x \rangle^2}. \quad (2.37)$$

The state is metrologically spin squeezed if $\xi_S^2 < 1$ is fulfilled. The ground state of BJJ with positive nonlinearity, $U > 0$, is spin squeezed with expectation value $\xi_S^2 = \frac{1}{\sqrt{1+\Lambda}}$ in the Rabi and Josephson regime and $\xi_S^2 = \frac{2}{N+2}$ (even N) in the Fock regime.

Now let us draw a direct connection to the earlier definition of the conjugate variables \hat{N}_- and $\hat{\Phi}$ in the two-mode BH model. The spin operator \hat{S}_z represents the population imbalance between the left and right condensate with its first momentum and the variance as defined in Eq. (2.28) equal to

$$\langle \hat{N}_- \rangle = 2\langle \hat{S}_z \rangle, \quad \Delta \hat{N}_-^2 = 4\Delta \hat{S}_z^2. \quad (2.38)$$

If the spin vector aligns with the x -axis on the Bloch sphere (this is the case with a well-defined phase in the Rabi regime), the corresponding analogy of the relative phase can be approximated to be

$$\hat{\Phi} = \arctan \left(\frac{\langle \hat{S}_y \rangle}{\langle \hat{S}_x \rangle} \right), \quad \Delta \hat{\Phi}^2 = \frac{\Delta \hat{S}_y^2}{|\langle \hat{S}_x \rangle|}. \quad (2.39)$$

The uncertainty principle is defined as

$$\Delta \hat{N}_-^2 \Delta \hat{\Phi}^2 \geq 1. \quad (2.40)$$

Whereas the standard quantum limit (SQL), corresponding to fluctuations of the spin coherent state, is

$$\Delta \hat{N}_-^2 = N, \quad \text{and} \quad \Delta \hat{\Phi}^2 = \frac{1}{N}. \quad (2.41)$$

and the Heisenberg limit is

$$\Delta\hat{N}_-^2 = N^2, \quad \text{and} \quad \Delta\hat{\Phi}^2 = \frac{1}{N^2}, \quad (2.42)$$

which can be reached with a genuine N -particle entangled state and can thus never be violated. We investigate later more in detail in Sec. 3.3.1 and Sec. 3.3.2 the evaluation of experimental data and estimation of number and phase squeezing factors and spin squeezing factors [6], as well as the dynamical generations of spin-squeezed state in Chpt. 6.

2.3 1D quasicondensates

In general, the full behaviour of the tunnel-coupled BECs, especially with 1D quasi-condensates, extends beyond the two-mode theories. In particular, the thermal excitations are non-negligible in the longitudinal direction. We cover here in Sec.2.3.1 the regime of our 1D Bose gas and in Sec.2.3.2 the effective field description in low energy expansion of a single 1D quasicondensate and 1D quasicondensates in a double well. The effective field theory predicts intriguing multimode dynamics in 1D quasicondensates, providing insight into our experimental observations presented in Sec. 7.3 and Chpt. 8.

2.3.1 1D weakly interacting Bose gases

In one-dimensional Bose gases, the confinement along two spatial dimensions restricts the motion of particles, resulting in enhanced interactions and a richer interplay between kinetic and potential energy. Based on the interplay between the different terms, we can categorize the 1D system into different regimes. First, the Lieb-Liniger parameter is a measure of the interaction strength per density in the system

$$\gamma = \frac{g_{1D}\rho_{1d}}{\hbar^2\rho_{1d}^2/m} = \frac{mg_{1D}}{\hbar^2\rho_{1d}}, \quad (2.43)$$

where ρ_{1d} is the longitudinal atomic density and m is the atomic mass. $\gamma \ll 1$ represents the weakly interacting regime, which is the case for our 1D Bose gases of Rubidium-87 atoms. Moreover, we find ourselves in the quasicondensate regime, if the reduced temperature $T' = T/T_d < \sqrt{\gamma}$, where the degeneracy temperature T_d is expressed as

$$T_d = \frac{\hbar^2\rho_{1d}^2}{2mk_B}, \quad (2.44)$$

indicating the temperature when the de Broglie wavelength is equal to the interparticle distance. With the typical experimental setting, we quantify our system as weakly interacting 1D quasicondensates. This regime is characterised by suppressed density fluctuations and pronounced phase fluctuations. Not that, in contrast to their higher-dimensional counterparts, 1D Bose gases do not condense to true BEC even at low enough temperatures. This originates from the dimensional dependence of the density of states $\mathcal{D}(\epsilon) \propto \epsilon^{d/2-1}$, where

d is dimensionality [46]. In $d = 1$ dimensional gases, $\mathcal{D}(\epsilon) \rightarrow \infty$ as energy approaches zeros $\epsilon \rightarrow 0$. The divergent state density prevents macroscopic occupation of a single quantum state at low temperatures, therefore the formation of true BECs in 1D is not possible.

Local observables in quasicondensates can be treated like observables in independent true condensates, while the global phase coherence is absent. The Hamiltonian with repulsive contact interaction can be expressed as

$$\hat{H} = \int dz \hat{\psi}^\dagger(z) \left[-\frac{\hbar^2}{2m} \partial_z^2 + V(z) - \mu + \frac{g_{1D}}{2} \hat{\psi}^\dagger(z) \hat{\psi}(z) \right] \hat{\psi}(z), \quad (2.45)$$

where μ is the chemical potential and $V(z)$ the potential energy and g_{1D} is the effective 1D interaction strength along the longitudinal direction

$$g_{1D} \approx 2\hbar a_s \omega_\perp, \quad (2.46)$$

where $\omega_\perp = \sqrt{\omega_x \omega_y}$ is the radial trap frequency. A more detailed expression of g_{1D} can be found in [47]. The field operator can be written in the phase-density representation

$$\hat{\psi}(z) = \sqrt{\hat{\rho}(z)} \exp(i\hat{\phi}(z)). \quad (2.47)$$

Without the trapping potential $V(z)$ in Eq. (2.45), the Hamiltonian is known as the Lieb-Liniger model and is exactly solvable [48]. However, with trapping potential included, the Lieb-Liniger model is excessive for computing the system's dynamics. Therefore we will introduce an effective model in the following section, providing a more accessible means of understanding the underlying physics within the experimental system.

2.3.2 Effective field theory

Instead of solving the complex Hamiltonian in Eq. (2.45), effective models, such as the Luttinger liquid and Bogoliubov's theory, simplify the calculation a lot by only collecting the leading terms in the Hamiltonian. As we will show later, these field descriptions in the low excitation regime can explain the dynamics of 1D Bose gases observed in the experiment. We will introduce in this section the effective field theory of a single condensate and a pair of condensates with finite or vanishing tunnel coupling.

2.3.2.1 Single quasicondensates

In weakly interacting condensates with suppressed density fluctuations, we can approximate the density operator with a mean density $\rho(z, t)$ and a density fluctuation operator $\delta\hat{\rho}(z, t)$ and express the field operator as

$$\hat{\psi}(z, t) = \sqrt{\rho(z, t) + \delta\hat{\rho}(z, t)} \exp(i\hat{\phi}(z, t)), \quad (2.48)$$

where $\hat{\phi}(z, t)$ is the spatially fluctuating phase. The bosonic commutation relation $[\delta\hat{\rho}, \hat{\phi}] = i\delta(z, z')$ is obeyed. Assuming small density fluctuation $|\delta\hat{\rho}|/\rho \ll 1$ and long wavelength phase fluctuations $|\partial_z \hat{\phi}|/\rho \ll 1$ (low energy excitations),

we insert this density-phase representation in Eq. (2.48) into the Hamiltonian in Eq. (2.45) and expand it to the second order. The zeroth order is the well-known Gross-Pitaevskii equation involving only the mean density ρ

$$\left[-\frac{\hbar^2}{2m} \left(\frac{\partial}{\partial z} \right)^2 + V(z) - \mu + g_{1D}\rho(z) \right] \sqrt{\rho(z)} = 0. \quad (2.49)$$

The first order $\hat{H}^{(1)}$ vanishes, making the second order $\hat{H}^{(2)}$ the dominant term for the fluctuations. By further applying the local density approximation, i.e. ignoring the kinetic energy of the mean density, $\partial_z^2 \sqrt{\rho(z)} \ll 1$, we express the second-order Hamiltonian as

$$\hat{H}^{(2)} = \int dz \left[\frac{\hbar^2}{8m\rho(z)} \left(\frac{\partial \delta \hat{\rho}}{\partial z} \right)^2 + \frac{g_{1D}}{2} \delta \hat{\rho}^2 + \frac{\hbar^2 \rho(z)}{2m} \left(\frac{\partial \hat{\phi}}{\partial z} \right)^2 \right]. \quad (2.50)$$

The first term is known as the quantum pressure term. At the long wavelength limit, $\partial_z \delta \rho \ll 1$, which corresponds to the low energy regime, the first term is much smaller than the second term. We can thus simplify the second-order Hamiltonian $H^{(2)}$ to the Tomonaga-Luttinger liquid Hamiltonian [26–28]

$$\hat{H}_{TLL} = \int dz \left[\frac{g_{1D}}{2} \delta \hat{\rho}^2 + \frac{\hbar^2 \rho(z)}{2m} \left(\frac{\partial \hat{\phi}}{\partial z} \right)^2 \right]. \quad (2.51)$$

This model is an important low-energy description of 1D problems and is used to describe most of the experimental findings in this thesis. Since the mean density $\rho(z)$ depends on the trap $V(z)$, the exact solution of the Tomonaga-Luttinger liquid depends on the trap geometry [49].

The simplest case is assuming a box potential of length L , leading to homogeneous atomic density, $\rho(z) = \rho_{1d}$. We can then expand the phase and number fluctuation operators with wave numbers $k_j = j\pi/L$,

$$\begin{aligned} \hat{\phi}(z) &= \sqrt{2/L} \sum_{j=1}^{\infty} \cos(k_j z) \hat{\phi}_j + \frac{\hat{\phi}_0}{\sqrt{L}}, \\ \delta \hat{\rho}(z) &= \sqrt{2/L} \sum_{j=1}^{\infty} \cos(k_j z) \delta \hat{\rho}_j + \frac{\delta \hat{\rho}_0}{\sqrt{L}}, \end{aligned} \quad (2.52)$$

and feeding this into the Hamiltonian from Eq.(2.51) with enforced Neumann boundary conditions typical for a hard-wall box potential,

$$\frac{\partial \hat{\phi}}{\partial z} \Big|_{z=0,L} = \frac{\partial \delta \hat{\rho}}{\partial z} \Big|_{z=0,L} = 0, \quad (2.53)$$

we obtain the quadratic Hamiltonian¹

$$\hat{H}_{TLL}^{(2)} = \sum_{j=1}^{\infty} \left[\frac{g_{1D}}{2} \delta \hat{\rho}_j^2 + \frac{\hbar^2 k_j^2}{2m} \rho_{1d} \hat{\phi}_j^2 \right] + \frac{g_{1D}}{2} \delta \hat{\rho}_0^2. \quad (2.54)$$

Note that the $j = 0$ mode in the relative phase field $\hat{\phi}_0$ does not enter the Hamiltonian. $\hat{\phi}_0$ corresponds to the global phase of the single quasicondensate. Furthermore, by introducing creation and annihilation operators for the phonon excitations [46]

$$\begin{aligned} \hat{b}_j &= \frac{1}{\sqrt{2}} \left(\sqrt{g_{1D}} \delta \hat{\rho}_j + i \frac{\hbar k_j \sqrt{\rho_{1d}}}{m} \hat{\phi}_j \right), \\ \hat{b}_j^\dagger &= \frac{1}{\sqrt{2}} \left(\sqrt{g_{1D}} \delta \hat{\rho}_j - i \frac{\hbar k_j \sqrt{\rho_{1d}}}{m} \hat{\phi}_j \right) \end{aligned} \quad (2.55)$$

we can rewrite the Hamiltonian in Eq.(2.54) for $k \neq 0$ modes as a set of independent harmonic oscillators

$$\hat{H}_{TLL}^{(2)} = \sum_{j \neq 0}^{\infty} \hbar \omega_j \left(\hat{b}_j^\dagger \hat{b}_j + \frac{1}{2} \right), \quad (2.56)$$

where in the full Bogoliubov spectrum the eigenenergy is expressed as $\epsilon_j = \hbar \omega_j$ with

$$\omega_j = ck_j \sqrt{1 + \xi_h^2 k_j^2 / 4}, \quad (2.57)$$

with the healing length²

$$\xi_h = \frac{\hbar}{\sqrt{g_{1D} \rho_{1d} m}} \quad (2.58)$$

and the phonon speed

$$c = \sqrt{\frac{g_{1D} \rho_{1d}}{m}}. \quad (2.59)$$

In typical experimental conditions, $\xi_h k \ll 1$, we can safely restrict ourselves to a linear dispersion regime $\omega_j = ck_j$. At thermal equilibrium, the mode occupation follows the Bose statistics $n_j = 1/[\exp(\hbar \omega_j / k_B T) - 1]$ and in the high occupation regime ($n_j \gg 1$) can be approximated as

$$n_j = \langle \hat{b}_j^\dagger \hat{b}_j \rangle = \frac{k_B T}{\hbar \omega_j}, \quad (2.60)$$

where T is the thermal temperature in the quasicondensate. From here, we will treat $\delta \rho$ and ϕ as classical fields, since $n_j \gg 1$ in the experimentally accessible regime³. From the thermal density distribution and by using the quadratic Hamiltonian in Eq (2.54), one can derive that the Gaussian thermal states are

¹ $\delta \hat{\rho}_j$ and $\hat{\phi}_j$ fulfill the commutation relation $[\delta \hat{\rho}_j, \hat{\phi}_k] = i \delta_{j,k}$

²Note that in some other works, the healing length sometimes is defined with an additional factor $1/\sqrt{2}$. In that case, the Eq. (2.57) is redefined accordingly.

³For general references, $\hbar \omega_1 / k_B \approx 0.5$ nK.

fully characterised by the fluctuation amplitudes

$$\langle \phi_j^2 \rangle = \frac{mk_B T}{\hbar^2 \rho_{1d} k_j^2}, \quad \langle \delta \rho_j^2 \rangle = \frac{k_B T}{g_{1D}}. \quad (2.61)$$

At thermal equilibrium, the first-order phase coherence between two spatial points z and z' in a single quasi-condensate

$$\mathcal{C}(z, z') = \frac{\langle \hat{\psi}^\dagger(z) \hat{\psi}(z') \rangle}{\langle \hat{\psi}^\dagger(z) \hat{\psi}(z) \rangle \langle \hat{\psi}^\dagger(z') \hat{\psi}(z') \rangle}, \quad (2.62)$$

decays exponentially over the thermal coherence length λ_T

$$\mathcal{C}(z, z') = \exp(-|z - z'|/\lambda_T), \quad (2.63)$$

where

$$\lambda_T = \frac{2\hbar^2 \rho_{1d}}{mk_B T}. \quad (2.64)$$

For reference, the thermal coherence length is $\lambda_T \approx 11 \mu\text{m}$ with temperature $T = 50 \text{ nK}$ and peak density $\rho_{1d}(z = 0) = 50 \mu\text{m}^{-1}$ in the typical magnetic traps used in this thesis.

In the case of a harmonic trap $V(z) = \frac{1}{2}m\omega_z z^2$, where the mean density is spatially dependent, the expansion basis in Eq. (2.52) should be replaced by Legendre polynomials [50] and the mode energies are

$$\omega_j = \omega_z \sqrt{\frac{j(j+1)}{2}}, \quad (2.65)$$

which are not equally spaced and incommensurate. As we will see in Sec. 2.3.2.2 and Chpt. 7, this spectrum and inhomogeneity in the mean density make comparison to the observed dynamics in the decoupled traps more challenging. Furthermore, we should note that including higher order expansion of the Hamiltonian breaks the integrability and couplings between the modes as described in Eq. (2.56) are present.

The presented Bogoliubov transformation and the effective model in this section can be easily extended for describing 1D quasicondensates in a double well with finite or vanishing tunnel coupling. The observables in the relative degree of freedom between the two condensates are directly accessible in the experiment, making them highly relevant for experimental studies.

2.3.2.2 Quasicondensates in a double well

Now let us consider a pair of tunnel-coupled 1D quasicondensates. Built on the effective field theory of a single quasicondensate in Sec. 2.3.2.1, we first introduce the Hamiltonian for describing the tunnel-coupled condensates can be simply expressed as

$$\hat{H} = \hat{H}_L + \hat{H}_R + \hat{H}_t, \quad (2.66)$$

where \hat{H}_L and \hat{H}_R are the Hamiltonian for each of the condensates expressed as in Eq. (2.45) and

$$\hat{H}_t = -\hbar J \int dz \left[\hat{\psi}_L^\dagger(z) \hat{\psi}_R(z) + \hat{\psi}_R^\dagger \hat{\psi}_L(z) \right] \quad (2.67)$$

governs the dynamics between the two tunnel-coupled condensates. To trans-

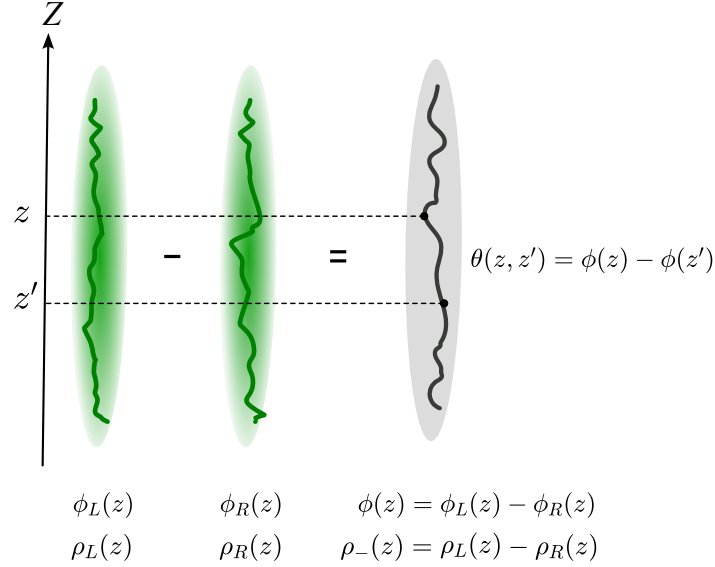


FIGURE 2.2: **Spatial relative observables definition** Each quasicondensate presents locally fluctuating phase $\phi_L(z)$ and $\phi_R(z)$. We define the relative phase between the two condensates $\phi(z) = \phi_L(z) - \phi_R(z)$. To study beyond zero momentum mode, we investigate the spatial distant relative phase $\theta(z, z')$ between two spatial points in the relative phase field.

form into a more convenient basis⁴, we define the local conjugate observables in the relative degree of freedom between the two condensates as depicted in Fig. 2.2

$$\begin{aligned} \hat{\rho}_-(z) &= \hat{\rho}_L(z) - \hat{\rho}_R(z), \\ \hat{\phi}_-(z) &= \hat{\phi}_L(z) - \hat{\phi}_R(z), \end{aligned} \quad (2.68)$$

and the common degree of freedom as

$$\begin{aligned} \hat{\rho}_+(z) &= \hat{\rho}_L(z) + \hat{\rho}_R(z), \\ \hat{\phi}_+(z) &= \hat{\phi}_L(z) + \hat{\phi}_R(z). \end{aligned} \quad (2.69)$$

Assuming balanced condensates, $\rho_L(z) = \rho_R(z) = \rho_0(z)$, we can then rewrite the Hamiltonian of BECs in a double well as

$$\hat{H} = \hat{H}_+ + \hat{H}_- + \hat{H}_t, \quad (2.70)$$

decomposed into Hamiltonian in the relative degree of freedom (–) and common degree of freedom (+) and the tunneling term H_t . Similarly to Eq. (2.48), using

⁴We define the operators to best match with our experimental analysis. With our definition, the commutation relations need to be modified with an additional factor of 2.

the relative density fluctuations representing the density fluctuations subtracted from the mean relative density field $\delta\hat{\rho}_-(z) = \hat{\rho}_-(z) - \rho_-(z)$, we can express the \hat{H}_\pm as the Tomonaga-Luttinger liquid Hamiltonian

$$\hat{H}_\pm^{(2)} = \int dz \left[\frac{g_{1D}}{4} \delta\hat{\rho}_\pm^2(z) + \frac{\hbar^2 \rho_0(z)}{4m} \left(\frac{\partial\hat{\phi}_\pm}{\partial z} \right)^2 \right]. \quad (2.71)$$

In decoupled double wells ($J = 0$), the Hamiltonian is simply

$$\hat{H}^{(2)} = \hat{H}_+^{(2)} + \hat{H}_-^{(2)}. \quad (2.72)$$

The relative and common DoF are completely independent of each other in the case of balanced and decoupled condensates. Furthermore, we take note that $\delta\hat{\rho}_- = (\hat{\rho}_L - \hat{\rho}_R) - (\rho_L - \rho_R) = \hat{\rho}_-$. Thus we can simply plugging $\langle\delta\rho_-^2\rangle = \langle\rho_-^2\rangle$ into Eq. (2.73) and obtain density fluctuation amplitudes for each mode as

$$\langle\rho_{-,j}^2\rangle = \langle\delta\rho_{-,j}^2\rangle = \frac{2k_B T}{g_{1D}}, \quad \langle\phi_{-,j}^2\rangle = \frac{2}{\lambda_T k_j^2} \quad (2.73)$$

where ρ_{1d} denotes the atomic density in each of the condensates. From here we will drop the minus sign in the relative phase $\hat{\phi}_-$ and simply use $\hat{\phi}$. One can derive that the variance of the phase difference between two spatial points in the relative phase field $\theta(z, z') = \phi(z) - \phi(z')$ is expressed as

$$\langle\theta(z, z')^2\rangle = \frac{|z' - z|}{\lambda_T}, \quad \text{where } \theta(z, z') = \phi(z) - \phi(z'), \quad (2.74)$$

thereby we recover the two-point phase correlation function of the relative phase, similar to what previously is shown in Eq. (2.63) for a single condensate,

$$\mathcal{C}(z, z') = \langle\cos\theta(z, z')\rangle = \exp\left(-\frac{\langle\theta(z, z')^2\rangle}{2}\right) = \exp\left(-\frac{|z - z'|}{2\lambda_T}\right). \quad (2.75)$$

Note that there is a factor of 2 in front of the thermal coherence length here compared to for a single condensate in Eq. (2.64).

Now let us turn to the case of finite tunnel coupling and simplify the tunnelling term in Eq. (2.67). We can neglect density fluctuations in the tunnelling Hamiltonian, namely use the expression $\hat{\psi}_i = \sqrt{\rho_0(z)} \exp(i\hat{\phi}_i(z))$, $i \in [L, R]$ in Eq. (2.67). This is valid in the low excitation regime, thus we obtain the following expression for the tunnelling term

$$\hat{H}_t = -2\hbar J \int dz \rho_0(z) \cos(\hat{\phi}(z)). \quad (2.76)$$

Together with the Hamiltonian in the relative DoF in Eq (2.71), we have derived the well known sine-Gordon Hamiltonian [16, 29, 30]

$$\hat{H}_{SG} = \hat{H}_-^{(2)} - \int dz 2\hbar J \rho_0(z) \cos(\hat{\phi}(z)). \quad (2.77)$$

In the context of the sine-Gordon model for tunnel-coupled BECs, the interplay between thermal fluctuations and the nonlinear interactions described by the sine-Gordon equation is crucial in characterizing the system's behaviour at finite temperatures. This is in principle relevant to the experimental findings in Chpt. 6. But as we restrict the measurements to the global observables, i.e. global relative number N_- and global phase Φ , in tunnel-coupled double wells (see Chpt. 6), we will spare further discussion on the sine-Gordon model here. For the main experimental observations of the 1D dynamics in the decoupled trap presented in Sec. 7.3, we will describe the time evolution of non-equilibrium states accordingly in the same chapter.

Chapter 3

Experimental system and readout

As the experimental setup has been described in detail by previous PhD theses [51–53], we only provide a concise description to stage this thesis within context. First, we will briefly cover the production of BEC from Rubidium vapours in ultra-high vacuum and its trapping with magnetic fields created with an atom chip. Then, we explain the radio frequency (RF) dressing technique used to smoothly transform the transversal trap from a single well to a double well. Thereafter, we introduce the imaging systems and the experimental readouts, in particular, the evaluation of fluctuations of experimentally accessible observables in a double well configuration highly relevant for Chpt. 4 and Chpt. 6.

3.1 BEC production

In this section, we provide a concise overview of the experimental process for producing BECs in an elongated trap from hot Rubidium vapours. We refer to previous theses [51–53] for more details. Additionally, we introduce the use of the RF dressing technique, which is employed to transform the magnetic trap in one axial direction. This technique is closely aligned with the primary scientific focus of this thesis, where we employ BECs in a double well as matter-wave interferometry.

3.1.1 Experimental sequence

We use a single ultra-high vacuum chamber¹ for cooling and trapping of the Rubidium-87 atoms. The entire experiment is controlled with an ADwin system² offering 32 analogue and 64 digital channels with time resolution $25 \mu\text{s}$ which are all controlled with a "home-built" user interface in MATLAB. Each experimental cycle takes 34.3 s. We divide the experimental cycle into different phases.

The first stage is often referred to as the Magneto-Optical Trap (MOT) phase. In our setup, we use a mirror-MOT configuration standard for atom chip experiments with only two pairs of counter-propagating laser beams. We laser cool [54]

¹at pressure $\approx 3 \cdot 10^{-11}$ mbar measured with ion gauge

²Jäger ADwin Pro

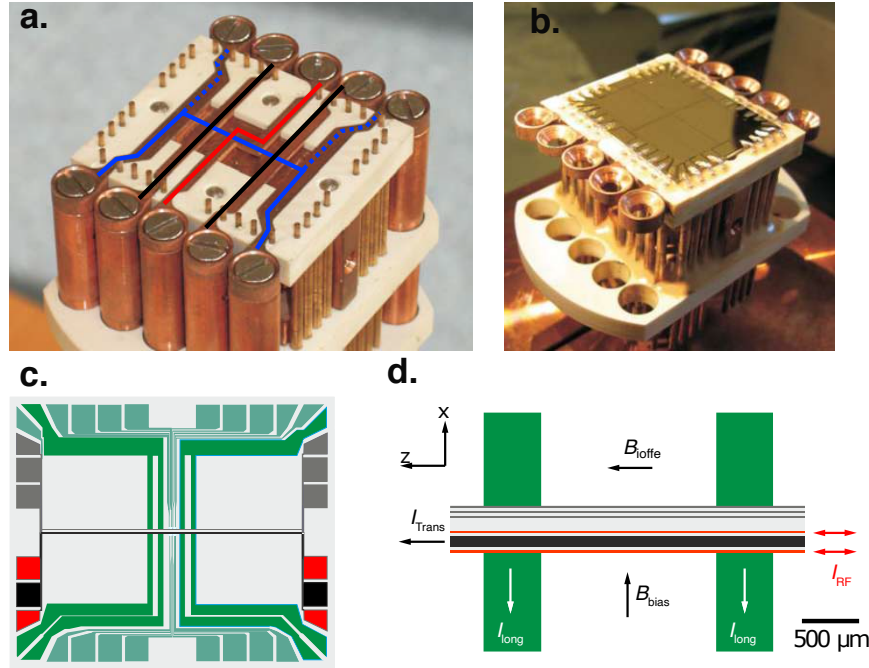


FIGURE 3.1: **Magnetic trap configurations** **a** Copper structures for creating rough magnetic Z-trap (red), U-trap (blue) and two I-wires for Stern-Gerlach separation. **b.** picture of atom chip used in this experiment. **c.** Layout of wires on the atom chip. Pads on the outer region are connectors. Black, dark green and red wires and pads are used in the experiment. **d.** Zoomed-in region of **c** including all the active wires on the atom chip used for creating the final trap of the experiment together with external magnetic fields from the coils. The black wire is the main trapping wire for radial confinement, internally referred to as $80\ \mu\text{m}$ wire. Two red wires are used for radio frequency (RF) dressing. Green wires create an H-trap for the longitudinal confinement. The figure is adapted from [51].

and trap the Rubidium-87 atoms in a quadrupole magnetic trap created by U-shaped copper wire lying above the atom chip in the vacuum chamber, as shown in Fig. 3.1a. We refer to literature for more details on techniques, such as laser cooling [54] and magnetic trapping of Rubidium atoms [55, 56]. At the end of the MOT phase, the atoms are optically pumped into state $|F = 1, m_F = -1\rangle$, where F is the total angular momentum and m_F is the component along the local magnetic field. The potential energy of neutral atoms in a static magnetic field is expressed by

$$V_s(\mathbf{r}) = m_F g_F \mu_B |\mathbf{B}_s(\mathbf{r})|, \quad (3.1)$$

where μ_B is the Bohr magneton and $\mathbf{B}_s(\mathbf{r})$ is the local static magnetic field. The Landé factor is $g_F \approx -1/2$ for the $F = 1$ hyperfine state, and m_F is the quantum number along the local magnetic field. The $|F = 1, m_F = -1\rangle$ state is thus a low field seeker, $V(\mathbf{r}) < 0$, making it a magnetically trappable state at local field minimum.

After the MOT stage, which prepares the atomic cloud to the temperature at milliKelvin level, we load the atoms into a magnetic Z-trap (created by the copper wire shown in Fig. 3.1a). In this "macro" Z-trap, we perform evaporative cooling by sending radio-frequency (RF) through the U-wire (see Fig. 3.1a) to

couple out hotter atoms, to lower the temperature after thermalization [57] further. From there, we transfer the cloud from the Z-trap into the final elongated magnetic chip trap created using an $80\ \mu\text{m}$ wide straight wire in combination with a Bias field for tight radial confinement and an H-shaped chip wire for shallow axial confinement. Chip wire layouts and homogeneous field orientations are shown in Fig. 3.1d. The evaporation cooling sequence is also performed during the trap loading phase. The exact sweeping frequencies and shapes can be found in other PhD theses[53]. The final experimental system consists of magnetically trapped elongated BECs with an aspect ratio of the radial and axial trap ~ 100 .

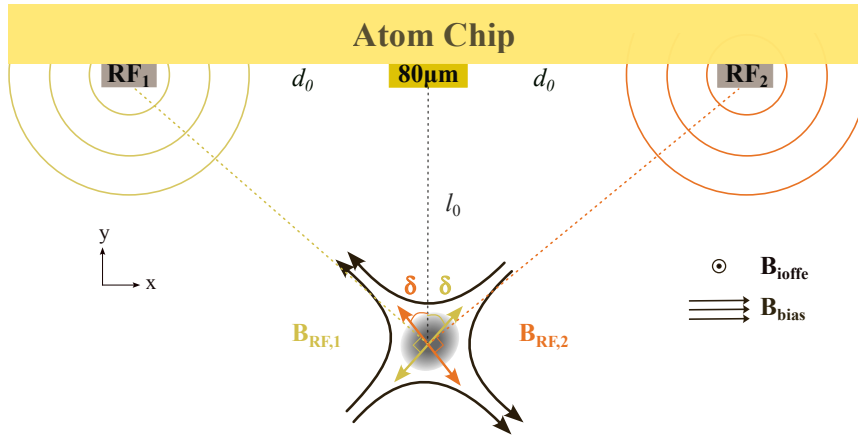


FIGURE 3.2: **Magnetic trap created by atom chip.** In addition to the static trap created with the main trapping wire (gold rectangle) and external Bias field which traps a single condensate. Radiofrequency (RF) is applied through the two symmetrically positioned RF wires (dark rectangle) around the trap wire to enable the creation of an RF-dressed double well along the transversal direction, x -direction, which is orthogonal to gravity. With two BECs, we can read out the relative observables between them: the relative phase Φ inferred from the interference pattern formed after long time-of-flight and the relative atom number N_- which is obtained by kicking the condensates apart before trap release so that they are spatially separated after TOF.

3.1.2 Radio frequency dressed double wells

In addition to forming a single elongated magnetic trap with static magnetic field, we can employ the RF dressing technique [58, 59] to allow a precise modulation of the transversal trapping potential and enable a smooth transition from a single well to a double well. RF dressing makes use of coupling of atomic state to an oscillating field which together with the static field, yields new eigenstates and eigenenergies [58]. The Hamiltonian of an atom in the superimposed fields of static and oscillatory fields can be described by

$$H = g_F \mu_B \mathbf{F} \cdot [\mathbf{B}_s(\mathbf{r}) + \mathbf{B}_o(\mathbf{r})], \quad (3.2)$$

where the static magnetic field can be expressed as

$$\mathbf{B}_s(\mathbf{r}) = -Gr(\sin \epsilon \hat{\mathbf{x}} + \cos \epsilon \hat{\mathbf{y}}) + B_{\text{ioffe}} \hat{\mathbf{z}}, \quad (3.3)$$

here G is the radial field gradient, radial distance is $r = \sqrt{x^2 + y^2}$, ϵ is the polar angle in the xy -plane, and B_{Ioffe} is the homogeneous Ioffe field along axial z -direction. See Fig. 3.2 for the orientation of the coordinate system, where y -direction is parallel to the gravity, x -direction is orthogonal to the gravity and z -direction is the axial direction of the elongated trap, indicating the weak confinement direction. The origin of this polar coordinate system is set to the static trap minimum located at a distance

$$l_0 = \frac{\mu_0 I_{80}}{2\pi B_{\text{bias}}} \quad (3.4)$$

right below the $80 \mu\text{m}$ wide main trapping wire. The distance l_0 is therefore determined by the current I_{80} through the main trapping wire and the homogeneous field B_{bias} along x -direction. The oscillatory RF field can be expressed by

$$\mathbf{B}_o(\mathbf{r}, t) = \mathbf{B}_{\text{RF},1} \cos(\omega_{\text{RF}} t) - \mathbf{B}_{\text{RF},2} \cos(\omega_{\text{RF}} t + \beta), \quad (3.5)$$

where $\mathbf{B}_{\text{RF}}^{1,2}$ is RF field with frequency ω_{RF} applied through the two straight RF wires parallel to the $80 \mu\text{m}$ wire, as shown in Fig. 3.1d. By applying a unitary transformation on the Hamiltonian in Eq. (3.2) to the rotating frame of the RF field, we can express the adiabatic potential given by the combined magnetic fields as

$$V(\mathbf{r}) = \hbar m'_F \sqrt{\Delta(\mathbf{r})^2 + \Omega(\mathbf{r})^2}, \quad (3.6)$$

where m'_F is the quantum number in the dressed picture; the local RF detuning is

$$\Delta(\mathbf{r}) = \frac{g_F \mu_B}{\hbar} |\mathbf{B}_s| - \omega_{\text{RF}}; \quad (3.7)$$

and the Rabi frequency

$$\Omega(\mathbf{r}) = \frac{g_F \mu_B}{\hbar} \mathbf{B}_{\text{RF}}^\perp(\mathbf{r}) \quad (3.8)$$

is represented by the radial components of the RF field orthogonal to the local static field. Each of the RF fields at the trap centre can be decomposed into

$$\begin{aligned} \mathbf{B}_{\text{RF},1} &= |\mathbf{B}_{\text{RF},1}| (\cos \delta \hat{\mathbf{y}} - \sin \delta \hat{\mathbf{x}}), \\ \mathbf{B}_{\text{RF},2} &= |\mathbf{B}_{\text{RF},2}| (\cos \delta \hat{\mathbf{y}} + \sin \delta \hat{\mathbf{x}}), \end{aligned} \quad (3.9)$$

where $\tan \delta = l_0/d_0$ with the distance between the RF wire and $80 \mu\text{m}$ main trapping wire, $d_0 = 55 \mu\text{m}$ and l_0 depends on the exact static trap configuration based on Eq.(3.4) (see Fig. 3.2). Experimentally the two RF fields are independently controllable. By tuning the relative phase β between the two RF fields, one can realise trapping potentials such as ring trap, horizontal vertical double wells, etc. [58]. Within the framework of this thesis, we focus on the creation of horizontal double wells (perpendicular to gravity) with RF dressing.

For this purpose, we set $\beta = 0$ to create a linearly polarized RF field perpendicular to the chip surface, namely along y -direction. We can then simplify the Rabi frequency to $\Omega(\mathbf{r}) = \hat{\mathbf{s}} \times (\mathbf{B}_{\text{RF},1} - \mathbf{B}_{\text{RF},2})$, where $\hat{\mathbf{s}} = \mathbf{B}_s/|\mathbf{B}_s|$ is the unit

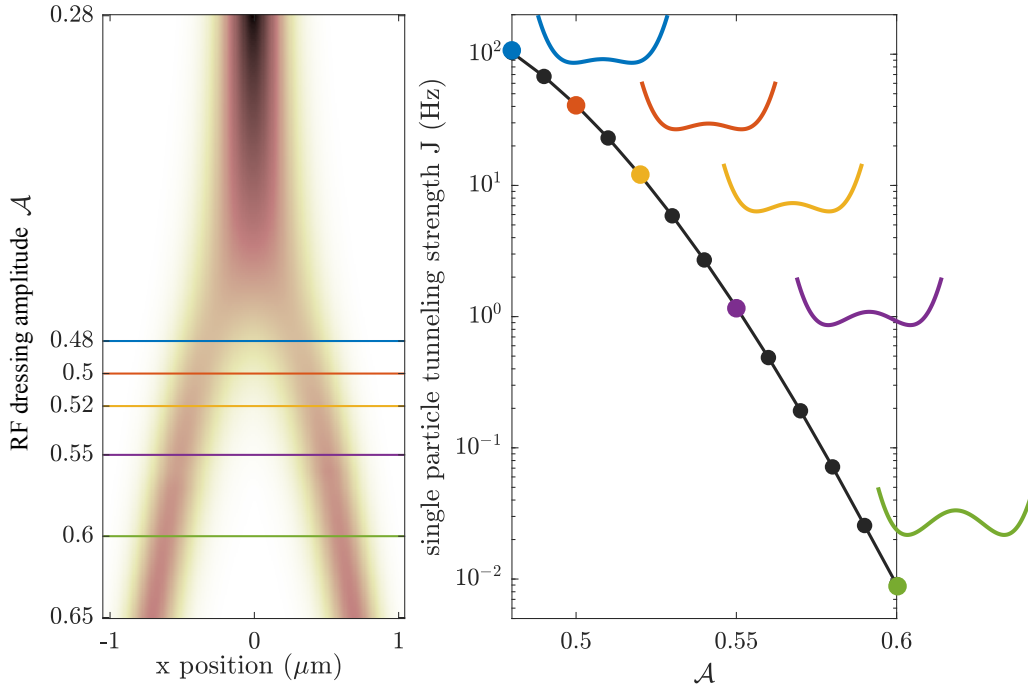


FIGURE 3.3: **Trap simulation on RF dressed double wells** **a.** transversal in-situ density as a function RF amplitude, \mathcal{A} , based on trap simulations within the rotating wave approximation. **b.** Inferred single particle tunneling strength J based on the single particle eigenenergies in Eq.(3.13).

vector of the local static field. We can rewrite it in the polar coordinates to

$$\hbar^2\Omega = \left(\frac{g_F\mu_B\mathbf{B}_{\text{RF}}}{2} \right)^2 \frac{B_{\text{ioffe}}^2 + G^2r^2 \sin(\alpha + \epsilon)^2}{|\mathbf{B}_s|^2}, \quad (3.10)$$

here α is the split angle related to the ratio between the two RF fields and ϵ is the polar angle in the static field from Eq.(3.3). To rotate the orientation of the double well in the xy -plane, we can modify the relative currents sent through the two RF wires with split angle α with

$$I_2 = I_2^0 \left(\cos \alpha + \frac{\sin \alpha}{2 \tan \delta} \right). \quad (3.11)$$

For symmetric double wells, it requires $I_1^0 = I_2^0$ and $\alpha = 0^\circ$ in ideal cases. We will get into more details in Sec. 3.4.2 on the experimental calibration of symmetric double wells.

For convenience, we rescale the amplitude of the applied RF field to its maximum current $I_{\text{max}} = 80.25$ mA and defined it as

$$\mathcal{A} = I/I_{\text{max}}. \quad (3.12)$$

This is our main control parameter for creating double wells. We show in Fig. 3.3 **a** the simulated in-trap single particle probability distribution $|\psi(x)|^2$

in the symmetric double wells as a function of the applied amplitude \mathcal{A} . In Fig. 3.3 b, we also plot the inferred single particle tunnelling strength with definition,

$$J = \frac{E_1 - E_0}{2}, \quad (3.13)$$

where $E_{0,1}$ is respectively the single particle eigenenergies of the ground and first excited state. The tunnelling strength is a highly relevant parameter for the dynamics between the BECs, as presented later in the thesis.

3.2 Imaging systems

Two independent imaging systems are used on our setup which are both destructive and take two-dimensional pictures of the atomic clouds after Time-Of-flight(TOF). One is absorption imaging and the other one is fluorescence imaging system. The main purpose of the current absorption imaging system is to estimate the total atom number, though in principle one can use it to estimate the temperature of BECs from density ripples [60]. We typically use this in combination with the fluorescence imaging system to infer the number of photons per atom collected on fluorescence images.

3.2.1 Absorption imaging system

Absorption imaging is broadly employed in ultracold atom experiments for its straightforward implementation. As the name suggests, a collimated resonant laser pulse (with duration $\sim 100 \mu\text{m}$) is shone onto the atoms after some TOF ($2 - 18 \text{ ms}$ on our setup) along the x -direction which drives the transition $F = 2 \rightarrow F' = 3$. Since the scattered photon is dictated by the dipole radiation pattern, the region of the beam passing through the atomic cloud is attenuated by

$$\frac{I_o(y, z)}{I_i(y, z)} = \exp(-\sigma_s \rho(y, z)), \quad (3.14)$$

where I_o is outgoing beam intensity; I_i is the incoming intensity; $\rho(y, z)$ is the atomic density after TOF and σ_s is the scattering cross section of driven optical transition. At the moment, we drive the σ^+ transition ($|F = 2, m_F = 2\rangle \leftrightarrow |F' = 3, m_{F'} = 3\rangle$) on the experiment.

The expected ideal cross-section in the low-intensity regime is $\sigma_s = 3\lambda_L^2/2\pi \approx 0.291 \mu\text{m}^2$ [56]. We found out that the effective scattering cross section on the experiment is smaller which is due to some imperfect alignment of the quantization axis and pumping effect. We estimate the effective cross-section to be $\sigma'_s = \sigma_s/1.2$, where 1.2 is an empirical factor measured directly on the experiment by using the technique developed in [61].

In practice, we sum up the number of atoms measured per pixel on the absorption camera³,

$$N = \sum_j n_j = \sum_j \frac{A}{\sigma'_s} \ln(S_o^j/S_i^j), \quad (3.15)$$

here $A = 2.11 \mu\text{m}$ is the pixel size in the objective plane, provided $5.5 \mu\text{m} \times 5.5 \mu\text{m}$ pixel size of the camera sensor and 3.78 magnification of the telescope. And S_o^j and S_i^j are respectively the number of photons collected on the j -th pixel in the image with and without atoms which are taken consecutively per experimental cycle.

3.2.2 Fluorescence imaging system

As mentioned in Sec. 3.2, we use the fluorescence imaging system as the main imaging system. It has a high dynamic range and a very good signal-to-noise ratio. This imaging system is usually referred to as the Light Sheet (LS) system. Its implementation is described in excellent detail in R. Bückner's diploma thesis [62, 63].

The LS system involves a pair of counter-propagating (lin- \perp -lin polarization) "vertically squeezed" plane laser beams (with vertical beam waist $2w_0 \approx 40 \mu\text{m}$), which also drive the transition $F = 2 \rightarrow F' = 3$. The beam lies $\approx 1 \text{ cm}$ below the atom chip. The TOF of LS imaging is determined by the beam position and is currently fixed at 43.4 ms. Each atom spends roughly $100 \mu\text{s}$ in the LS and the total cloud takes around 2 ms to fall through the LS beam. Shorter imaging pulses can be used to probe only a fraction of the cloud. We have for instance tried shorter imaging pulses to figure out the vertical orientation of our BECs with respect to the LS and to improve the contrast of the interference fringes.

Finally the EMCCD chip⁴ collects a small fraction (2 – 3%) of the emitted photons. The pixel size in the objective space is $4 \mu\text{m} \times 4 \mu\text{m}$. But the effective imaging resolution, especially on single atom detection is worse. This is due to the random walk of atoms inside the LS while it scatters photons. We will characterise this in Sec. 3.3.1. We usually choose $\pm 3 \text{ MHz}$ detuning from the optical resonance to minimize this "blurring" effect.

The main calibrations needed on fluorescence images are: **(1)** determining the gain factor g from the electron multiplying process of the camera chip. This is calibrated with every single experimental image by fitting the digital counts per pixel C on a reference image (taken with no light) with function $\frac{1}{g} \exp -C/g$. **(2)** correcting for the background signal b caused by either clock-induced charges (CIC) or stray light from the LS and reflection of scattered light from the atom chip surface. This is estimated by taking an atom-free region on the camera chip. **(3)** estimating the average photons per atom \bar{p} collected on camera. This is done by preparing BECs with different atom numbers and alternating between

³BASLER© acA2000-165 μm CMOS camera (CMV2000) is in use since 2019.

⁴Andor iXon+ 897 was in use until October 2022, with which all the experimental data has been taken.

fluorescence imaging (with total fluorescence signal S) and absorption imaging to obtain atom number N to extrapolate \bar{p} with the linear function $S = \bar{p}N$.

We note that both photons per atom p and the number of counts C per photon are random variables, thus their distribution will also contribute to additional noises. It was investigated in detail in [51, 62]. Assuming the variance of the detected photons is given by photon shot noise and taking into account the added noise from the electron multiplication process, one can estimate the contributed variance from shot noises $\Delta_{sn}S^2 = 2S$, where S is the primary photons. Other details on the EMCCD chip readout and noise correction for evaluating number squeezing factors are discussed in Sec. 3.3.1.

3.3 BECs in double well readout

In this section, we will introduce the experimental readout of BECs in double wells with a particular focus on statistical estimation. In the lower panel of Fig. 3.4, standard experimental images for the two experimental readouts are displayed. They are taken using our fluorescence imaging system after condensates are released from the trap and have undergone a long TOF. In the following subsections, we will study in detail the evaluation of each type of readout.

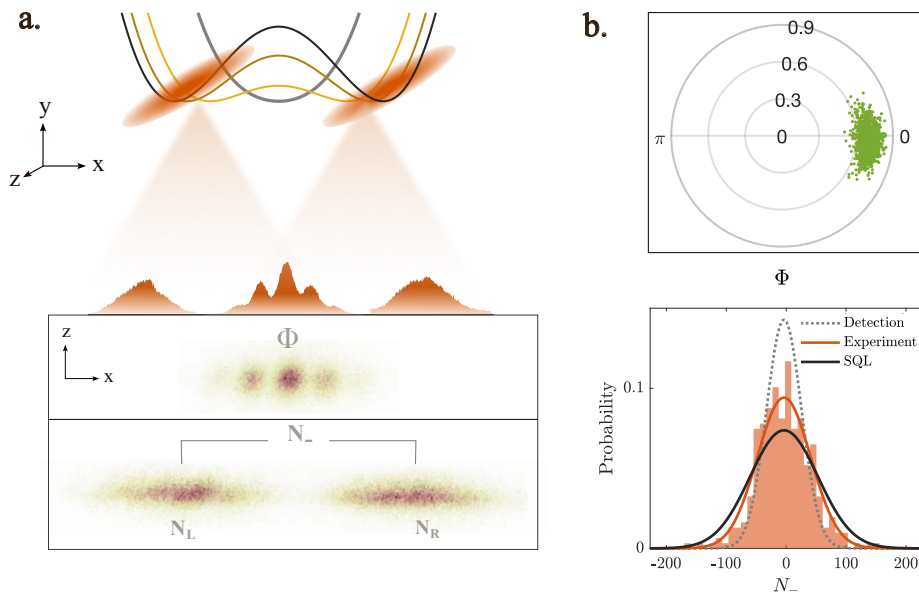


FIGURE 3.4: **Experimental readout and statistical evaluation.** (a) relative atom number, $N_- = N_L - N_R$, and relative phase, Φ , measurement of BEC in double wells after TOF expansion. We evaluate the global observables by integrating along z -direction. (b) Histogram of Φ and N_- of experimental data. A solid black line, labelled SQL, denotes the standard quantum limit which follows a binomial distribution. The dotted grey line indicates the detection noise distribution.

3.3.1 Relative number readout

The relative number measurement is obtained by raising the RF amplitude swiftly right before switching off the trap. The clouds then receive a transversal kick outwards, so that after TOF they become spatially separated on the LS image (see Fig. 3.5). Detailed tuning on the kick sequence has been investigated in Sec. 3.4.3.1 which involves the quench duration⁵, kick amplitude $\mathcal{A}_{\text{kick}}$ and final hold time in the double well at $\mathcal{A}_{\text{kick}}$.

With the obtained 2D atomic density in the xz -plane (see Fig. 3.4), for the majority of the data analysis we sum up all the detected signals within the region of interest (ROI) for each condensate and obtain photon signals S_L and S_R , such as shown in Fig. 3.5. Usually, we pre-calibrate the average collected photons per atom in LS, \bar{p} , by combining signals detected with LS and atom number directly extracted from absorption image, leading to

$$N = \frac{S}{\bar{p}}. \quad (3.16)$$

Hence we can easily deduce the atom number in each condensate N_L and N_R .

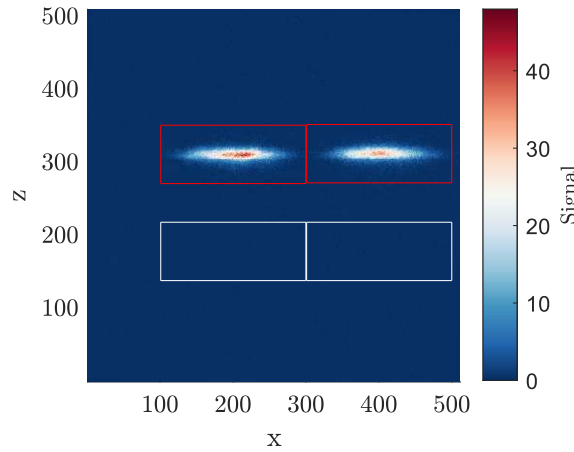


FIGURE 3.5: **Experimental image for relative number readout** The red rectangle marks the region of interrogation (ROI) with signals from atoms. The white rectangle marks ROI for background correction. Both ROIs have the same area. Signal indicates the primary photons.

If we are only interested in the mean values of relative atom number $\langle N_- \rangle = \langle N_L - N_R \rangle$, the routine is now complete. We can simply evaluate the relative imbalance

$$n = N_-/N, \quad (3.17)$$

where $N = N_L + N_R$ is the total atom number (see for instance Fig. 3.11) with a single shot or averaging over a few shots to obtain $\langle n \rangle$. However, the main topic of this thesis is to assess quantum fluctuation. We quantify it with the number squeezing factor, which is defined as the ratio between the variance of

⁵quench in this case refers to a fast ramp-up of RF dressing amplitude.

the relative atom number, ΔN_-^2 , and the variance of the binomial distribution, $\Delta N_{-,B}^2 = N$

$$\xi_N^2 = \frac{\Delta N_-^2}{\Delta N_{-,B}^2} = \frac{\Delta N_-^2}{N}. \quad (3.18)$$

Starting with the statistical variance on the detected relative photon signal, $S_- = S_L - S_R$, where we neglect for now the distribution of the emitted photons per atom and assume an average photon per atom \bar{p} and the other noises

$$\Delta S_-^2 = \Delta(\bar{p} \cdot N_-)^2 = \bar{p}^2 \Delta N_-^2 = \xi_N^2 \cdot \bar{p} \cdot S, \quad (3.19)$$

we redefine the number squeezing factor as

$$\xi_{N,\text{raw}}^2 = \frac{\Delta S_-^2}{\bar{p}S}. \quad (3.20)$$

In order to properly evaluate the number squeezing factor, we need to correct the excess detection noise by subtracting it from ΔS_-^2 . First of all, the number of photons detected from each atom and the number of electron counts caused by each primary photon are both random variables, so their contribution to the measured statistical distribution needs to be taken into account.

If we define S as the expectation value of the number of primary photons detected on a certain area of the CCD chip and \hat{S} as the random variable with expectation value S . The photon shot noise is estimated to be $\Delta_{sn}\hat{S}^2 = S$. In addition, the noise on the primary photon signal is doubled after the electron multiplication process of the EMCCD chip [64], therefore the actual photon shot noise is

$$\Delta_{sn}\hat{S}^2 = 2S. \quad (3.21)$$

Secondly, background signals, \hat{b} , originated from clock-induced charges and stray light are indistinguishable from actual signals from atom. Since they are more dominant in low-density areas, we pick an atom-free region in the LS image (see Fig. 3.5) and sum up the detected signals in this ROI to estimate \hat{b} . We then estimate the noise contribution from the background signal to be

$$\Delta b^2 \approx \Delta_{sn}\hat{b}^2 = 2b, \quad (3.22)$$

where the actual measured $\Delta\hat{b}^2$ is slightly higher than $2b$ [63]. So the total detection noise is

$$\Delta_D\hat{S}^2 = 2S + \Delta\hat{b}^2. \quad (3.23)$$

With detection noise subtracted, eq.(3.18) is revisited to

$$\xi_N^2 = \frac{\Delta S_-^2 - \Delta_D S^2}{\bar{p}S} = \frac{\Delta S_-^2 - 2S - \Delta b^2}{\bar{p}S}. \quad (3.24)$$

the error bar on ΔS_-^2 is calculated using the bootstrapping method⁶, and the

⁶*bootci* with 32% confidence interval in MATLAB

corresponding error bar on number squeezing factor is obtained by using error propagation. The exact details on extracting the primary electrons from the raw EMCCD images have been studied extensively in [63].

So far, we have assumed a perfectly symmetric splitting, namely $\langle n \rangle = 0$, for the calculation of the number squeezing factor. If we now take into account a nonzero imbalance, the formula of the number squeezing factor in Eq.(3.18) needs to be revised. We revisit the relative signal to be [3]

$$\tilde{S}_- = S_- - (2m - 1)S, \quad (3.25)$$

so that the relative signal between the left and right condensates is $\langle \tilde{S}_- \rangle = 0$. Here m is the probability of a single atom ending up in the left well,

$$m = \frac{\langle S_L \rangle}{\langle S \rangle} = \frac{1}{2} \frac{\langle S \rangle + \langle S_- \rangle}{\langle S \rangle} = \frac{1}{2} + \frac{n}{2}. \quad (3.26)$$

In other words, we define $\tilde{S}_- = S_- - nS$. In addition, we rewrite the variance of the binomial distribution with a more general definition

$$\Delta N_{-,B}^2 = 4(1 - m)mN, \quad (3.27)$$

we can then rewrite the binomial variance with the relative imbalance as

$$\Delta N_{-,B}^2 = (1 - n^2)N. \quad (3.28)$$

As one can see $\Delta N_{-,B}^2$ is at maximum with balanced BECs $n = 0$. We can revise the number squeezing factor definition from Eq. (3.18) to The revised number squeezing factor is then

$$\tilde{\xi}_N^2 = \frac{\Delta \tilde{S}_-^2 - 2S - \Delta b^2}{(1 - n^2) \cdot \bar{p}S} = \frac{\Delta (S_- - nS)^2 - 2S - \Delta b^2}{(1 - n^2) \cdot \bar{p}S}, \quad (3.29)$$

where the revised $\tilde{\xi}_N^2$ yields a correct number squeezing factor also for nonzero imbalances.

3.3.2 Relative phase readout

Matter-wave interferometry provides a unique way of accessing the quantum phase. There are different ways of reading out the relative phase between the two condensates, for instance, the adiabatic recombiner that has been used in the Mach-Zehnder interferometer project conducted on this experiment [65] or the TOF recombination procedure. Here we use the latter as it is more straightforward.

By releasing the BECs from the double well, the clouds will expand rapidly in the radial direction, overlap with each other and form interference patterns during TOF (see Fig. 3.6a). After the long TOF ($t_{\text{TOF}} \gg 1/f_{\perp}$) with LS imaging, this is equivalent to a Fourier transform of the in-trap density distribution,

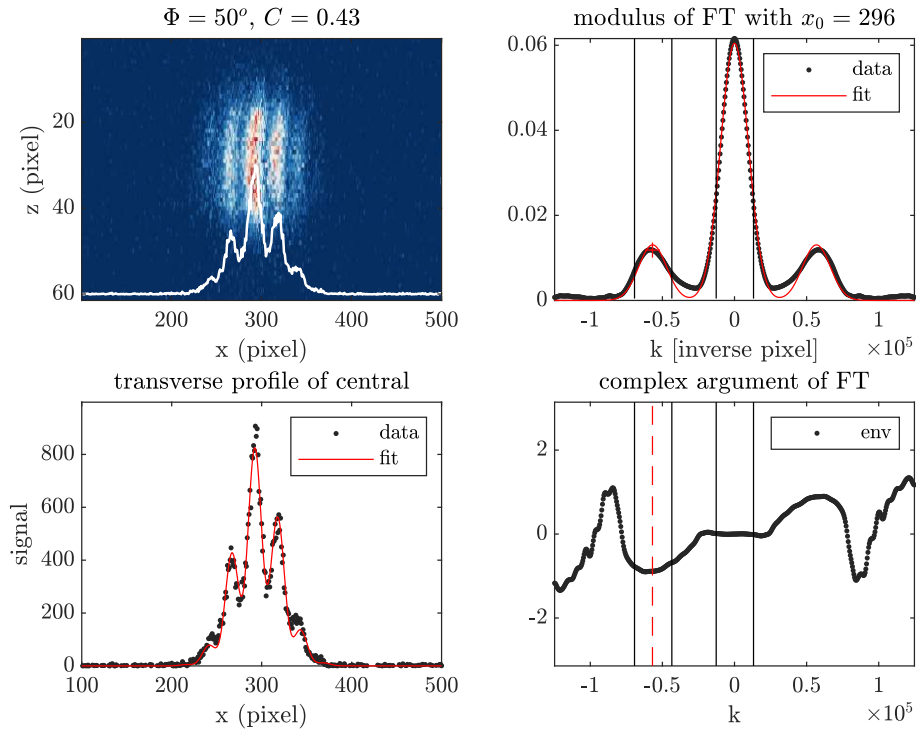


FIGURE 3.6: **Extraction of the relative phase, Φ** **a.** An example of an interference pattern with the fluorescence imaging system. The white solid line is the integrated interference pattern. **b.** Extracting relative phase from the integrated interference pattern by fitting with Gaussian envelope with cosine modulation. **c.** Modulus of Fourier transform of the integrated fringe (black) and the fit with three Gaussian peaks (red). The ratio between the central peak and the side peak represents the fringe visibility $C = |\max(k_L)/\max(k_C)|$ and + markers the momentum k_0 from Eq.(3.35). **d.** The imaginary part of the Fourier transform whose value at k_0 (red dashed line) is the relative phase Φ .

namely it represents the momentum distribution of the two condensates. An example of obtained 2D interference pattern is shown in Fig. 3.6 **a**.

To enhance the fringe visibility, we apply a weak inhomogeneous magnetic field in the longitudinal direction using "Cu-I" wires (black wires in Fig. 3.2 **a**) to spatially separate the three m_F states. This is typically referred to as the Stern-Gerlach separation. The field is turned on 1 ms after trap release to ensure the two BECs have overlapped with each other. The relative m_F state population used to fluctuate depending on the duration of the RF dressing sequence. This is caused by a mismatch of the switch-off timing between the magnetic trap and the RF dressing field. After the implementation of a new RF dressing source at the end of 2021. More details are given in Sec. 3.4.1. The state population is now stabilized over hold time. We usually pick the most populated m_F states which is $m_F = -1$ for relative phase extraction (see Sec. 3.3.2).

By evaluating a slice of fringe pattern along the longitudinal direction, we can gain information on the relative phase at each spatial position. This is very important for quasicondensates with pronounced local fluctuating phases. As

we will see in Chpt.7, the capability of reading out the local relative phase is very important. In the first iteration, we ignore the longitudinal degree of freedom and focus on the extraction of the relative phase based on integrated fringes which gives us the global relative phase. For extracting the local relative phase, the same procedure follows.

There are two extraction methods that we use. The first one is by fitting the (integrated) fringes with the function

$$n(x) = g(x - x_0) [1 + C \cos(k_0 \cdot (x - x_0) + \Phi)], \quad (3.30)$$

where Φ is the (global) relative phase, C is the fringe visibility and g is a Gaussian envelope

$$g(x - x_0) = \frac{N}{\sqrt{\pi}\sigma_T} \cdot \exp\left(-\frac{(x - x_0)^2}{2\sigma_T^2}\right) \quad (3.31)$$

with center x_0 and transversal width σ_T after TOF as fitted parameter. Assuming a ballistic expansion, we can express the transversal width as a function of TOF

$$\sigma_T(t)^2 = a_\perp^2 + \left(\frac{\hbar t}{ma_\perp}\right)^2 = a_\perp^2(1 + \omega_\perp^2 t^2), \quad (3.32)$$

here we use the Gaussian width of the in-trap wavepacket $a_\perp = \sqrt{\hbar/(m\omega_\perp)}$. To take into account interaction broadened in-trap cloud width, we can use instead $a_b = a_\perp \sqrt{1 + 2a_s \rho_{1d}}$. For more discussion and interaction-dependent TOF expansion, we refer to Rauer's PhD thesis [66]. The wave number k_0 of stationary wavepackets depends on the TOF duration t_F with the expression

$$k_0(t_F) = \frac{dm\omega_\perp^2 t_F}{\hbar(1 + \omega_\perp^2 t_F^2)} = \frac{d\omega_\perp t_F}{\sigma_T^2}, \quad (3.33)$$

where d is the intercloud distance. The wave number is related to the fringe spacing

$$\lambda_{fs} = \frac{2\pi}{k_0}, \quad (3.34)$$

which represents the distance between two neighbouring maxima within the interference pattern. We show the fit of integrated fringes based on Eq. (3.30) in Fig. 3.6 b. The fringe contrast is $0 \leq C \leq 1$, ideally, quantifying the coherence property of a matter-wave source. In reality, it is reduced by technical noises. By directly fitting on the integrated fringes, C is further lowered by spatially fluctuating relative phase along the quasicondensate.

Another relative phase extraction method is to Fourier transform along the x -direction of the 2D interference pattern (upper left panel in Fig. 3.6). We then obtain from Fourier transforming the interference pattern expressed in Eq. (3.30),

$$S(k) = \sqrt{2\pi}G(k)e^{ikx_0} * \left[\delta k + \frac{C}{2}[\delta(k - k_0)e^{i\Phi} + \delta(k + k_0)e^{-i\Phi}] \right], \quad (3.35)$$

where $G(k)$ is the Fourier transform of $g(x)$ and δk is the Dirac delta function. The modulus of integrated $S(k)$ is shown in Fig. 3.6 **c** and the complex argument of integrated $S(k)$ is plotted in Fig. 3.6 **d**. The relative phase is obtained by

$$\Phi = \text{ARG} \left[\int_{k_0-dk}^{k_0+dk} dk G(k) \right], \quad (3.36)$$

where the exact choice of integration region dk is not so crucial. And the fringe visibility is evaluated as

$$C = 2 \cdot \frac{\int_{k_0-dk}^{k_0+dk} |G(k)|}{\int_{-dk}^{dk} |G(k)|}. \quad (3.37)$$

It has been previously checked that the extraction method with Fourier transform gives more precise and robust results [53]. So this is the main method we use within the scope of this thesis. The direct fit on the fringe is mainly used to determine the centre of the Gaussian envelope, x_0 . Further discussion on fixing or fitting x_0 depends on the details of the preparation of the double well and has been investigated earlier [53].

As the relative phase is a circular variable, we introduce the circular mean to estimate the expectation value of Φ

$$\langle \Phi \rangle = \text{ARG} \left(\frac{1}{M} \sum_{j=1}^M \exp(i\Phi_j) \right) = \text{Arg}(r), \quad (3.38)$$

based on M statistical repetitions and r is referred to as resultant. Following the same concept as the number squeezing factor, which is to rescale the variance with respect to the variance of a binomial distribution $\Delta_B \Phi^2 = 1/N$ (the standard quantum limit), we define

$$\xi_\Phi^2 = \Delta \Phi^2 \cdot N, \quad (3.39)$$

as the phase squeezing factor. Here $\Delta \Phi$ is the standard deviation of a normal distribution wrapped around 2π

$$|r| = \exp \left(-\frac{\Delta \Phi^2}{2} \right), \quad (3.40)$$

thus we can estimate the standard deviation of the relative phase with

$$\Delta \Phi = \sqrt{\ln \left(\frac{1}{r^2} \right)} = \sqrt{-2 \ln |r|}. \quad (3.41)$$

For number squeezed state, $\xi_N^2 < 1$, the phase squeezing factor is always $\xi_\Phi^2 > 1$ to obey the Heisenberg uncertainty principle, $\xi_N^2 \cdot \xi_\Phi^2 \geq 1$. Combining the fluctuations in the conjugate quadratures, we introduce the spin squeezing factor ξ_S^2 [6]. Spin squeezing factor is a metrologically useful quantity and a witness

for many-body entanglement [67]. The spin squeezing factor is defined as

$$\xi_S^2 = \frac{\xi_N^2}{\langle \cos \Phi \rangle^2}, \quad (3.42)$$

where the phase coherence factor $\langle \cos \Phi \rangle$ is another measure for the phase spread and is evaluated as the statistical average of M realisations

$$\langle \cos \Phi \rangle = \frac{1}{M} \sum_{j=1}^M \cos(\Phi_j - \langle \Phi \rangle). \quad (3.43)$$

We subtract the mean value $\langle \Phi \rangle$ to get rid of the influence of a nonzero $\langle \Phi \rangle$ on the estimation of the phase coherence factor with imperfect experimental results. Note that, in case of small phase spread, $\sin \Phi \approx 0$, we can approximate $\langle \cos \Phi \rangle \approx \cos \Delta \Phi \approx 1 - \frac{\Delta \Phi^2}{2}$. The spin-squeezed state, indicated by $\xi_S^2 < 1$, is a class of entangled many-body states [8].

3.4 Double well characterisation

In reality, it is almost inevitable to encounter imperfection in experimental realisations. In the effort towards achieving a completely symmetric double well, orthogonal to gravity (which is along y -direction), we have performed different types of measurements to first compare the experimental double wells to the simulated ones and then to find the right settings for symmetric double wells. It is also worth noting that since the vacuum opening in 2017, the field alignment might have changed slightly, especially big bias and small Ioffe fields. Hence a new calibration after the vacuum opening in 2017 is much needed.

3.4.1 Comparison with trap simulation

Characterisation of a system is a first step towards controlling it. The initial scientific attempt of running an open-loop optimisation on the experiment motivates an exact mapping of the various double wells⁷. It has later been proven to be challenging to simulate the 1D experimental system using the many-body simulation MCTDHB (discussed later in Sec. 6.2.2). Nevertheless, it is beneficial to characterize the double wells and compare them to the trap simulation on RF-dressed double wells, especially for the determination of tunnel coupling strength.

A comprehensive simulation of the static and dressed trap based on the atom chip wires used in the experiment was developed earlier⁸. By plugging in the settings for OCT trap (named after historical reason) configuration (defined in Tab. A.1), the simulation gives characteristics of a 3D trap in terms trap bottom, trap frequency, barrier height, and etc. In Fig. 3.7, we compare the simulated double well potentials to the experimentally measured double wells

⁷in collaboration with Phila Rembold

⁸Developed by Aurelian Perrin

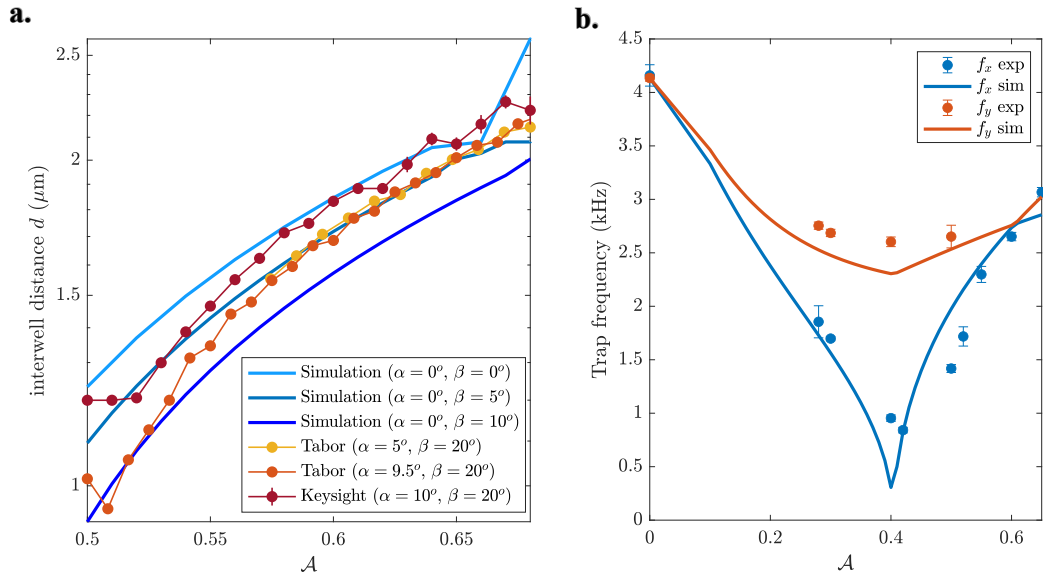


FIGURE 3.7: **Double well characterization a.** Comparison between trap simulation and experiment. Tabor and Keysight are two different AWGs used for RF dressing on the experimental setup. Split angle, α , defines the ratio of peak-to-peak voltage of the RF signals sent through the two RF dressing wires. $\alpha = 0$ indicates equal RF amplitudes through the two wires. Angle β is the relative phase between the two RF fields from the independent channels. **b.** Measured transversal trap frequency f_x and vertical trap frequency f_y in dressed double well with Keysight.

with respect to inter-well distance d , which can be experimentally inferred from the interference pattern (see Sec. 3.3.2).

During the course of this thesis work, two different Arbitrary Waveform Generators (AWGs) have been used in the experiment as RF dressing sources. We refer to them as Tabor⁹ and Keysight¹⁰. Tabor was in use until December 2021 and Keysight has been in use since then to date. As one can see in Fig. 3.7 a, Keysight AWG gives better-matched double well potentials with the trap simulation. As one can see, symmetric double wells ($\alpha = \beta = 0^\circ$ in simulation) are obtained with experimental parameters $\beta = 20^\circ$ with Keysight AWG. Split angle α results in a relatively small influence on d , as one can see in Fig. 3.10. While RF dressed double wells with Tabor match more with simulated traps at $\beta = 5^\circ$. By directly checking the output waveform with Keysight, we see more clean sine waves compared to Tabor which gives a higher harmonics component on top of the designed sine wave. Note that at large RF dressing amplitudes, $\mathcal{A} \geq 0.66$ at $\beta = 0^\circ$, the trap simulation does not work very reliably.

In Fig. 3.7 b, we plot the experimentally measured transversal trap frequency, f_x and vertical trap frequency f_y for variously dressed trap. As a comparison, we also plot the fitted trap frequencies from simulated double wells. The change in vertical trap frequency as a function of RF dressing amplitude is less significant

⁹Tabor Electronics 50MS/s Dual-Channel Arbitrary Waveform Generator WW5062

¹⁰Keysight 33600A Series Waveform generator, 120 MHz, 2-channel

compared to the transversal trap frequency. Around $\mathcal{A} = 0.42$, this is the critical point transitioning from a single well to a double well.

3.4.2 Symmetric double well calibration

To prepare BJJ at the stable fixed point of the classical phase space, i.e. $\langle n \rangle = \langle \Phi \rangle = 0$, it is very important to ensure a completely symmetric splitting. In practice, it requires at first careful calibration of the initial static trap characterized by the trap bottom and trap frequency. This is crucial since the detuning between the RF dressing frequency and trap bottom Δ_0 influences the resulting RF dressed trap. We do not get into details of calibration of the static trap, as it has been described in previous thesis work [51, 52]. Here we focus on the calibration of a symmetric double well by looking at either the energy offset between the two wells or the mean imbalance after splitting.

3.4.2.1 Double well trap bottom spectroscopy

For more precise calibration of symmetric double well with respect to the split angle α , we perform a trap bottom (TB) spectroscopy on the double well $\mathcal{A} = 0.65$ (MZI). What we refer to as "Trap Bottom" (TB) is the Larmor frequency of atoms at the trap centre. In the dressed trap, the TB can be expressed with the effective magnetic field \tilde{B} [58]

$$\nu_{TB} = \frac{g_F \mu_B}{\hbar} \cdot \tilde{B}, \quad \tilde{B} = \frac{B_{RF}}{2} \sqrt{1 + \frac{\hbar \Delta_0}{g_F \mu_B B_0}}, \quad (3.44)$$

where B_0 is the static trap at the trap centre and Δ_0 is the RF detuning at the trap centre, as defined in Eq.(3.7). This expression is only qualitatively accurate, hence we do not expect a perfect match with the experiment.

The TB spectroscopy is essentially an RF spectroscopy [68]. By applying a weak RF field¹¹ onto the atoms, we couple out the atoms from the trapped state to an untrapped state. The applied RF pulse is typically 20 ms long to cancel out the 50, Hz electronic noise from the power grid. By allowing some additional time after the RF pulse, the untrapped atoms will leave the trap early and therefore do not end up in the final image. At the resonance, namely, when the applied RF frequency is equal to ν_{TB} , the coupling is maximized and all atoms are outcoupled. For double wells, in order to read out the signals in each condensate separately, we add a kick sequence before the trap release the same way as a typical relative number readout.

In Fig. 3.8, we show the results of the double well TB spectroscopy by scanning the applied RF frequency. We perform the spectroscopy for different split angles α . By fitting the detected signals of each condensate $\langle S_L \rangle$ (Fig. 3.8 a) and $\langle S_R \rangle$ (Fig. 3.8 b) and by fitting the summed signal $\langle S_L + S_R \rangle$ (Fig. 3.8 c) with a Lorentzian function, we can extrapolate the respective TB in each well, TB_L

¹¹the same source as evaporative cooling, but significantly reduced intensity

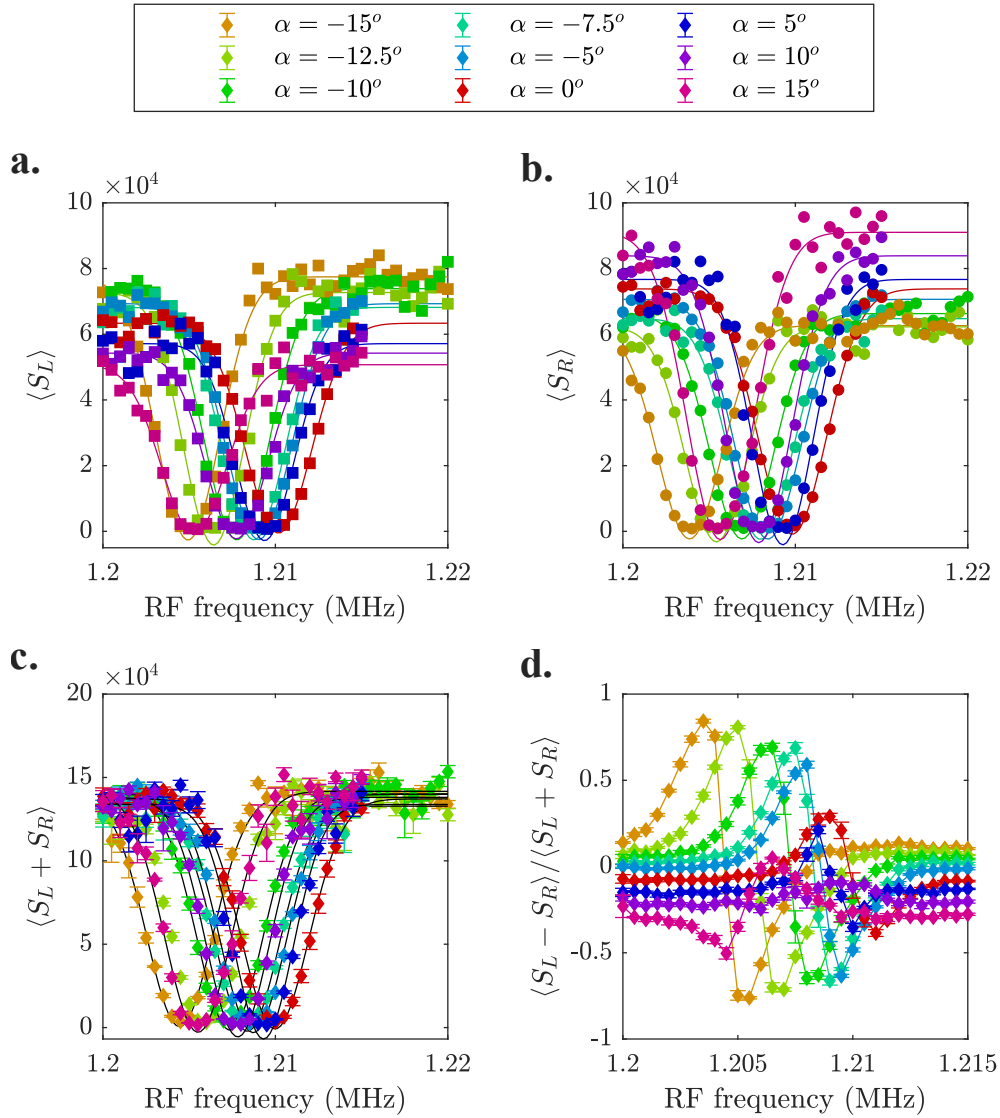


FIGURE 3.8: **Double well trap bottom spectroscopy.** Detected signal on LS as a function of RF sweeping frequency with varying α which defines the ratio of RF dressing amplitude between the two RF wires. Trap bottom spectroscopy of left well by counting signal of the left condensate $\langle S_L \rangle$ (a.) and the right condensate $\langle S_R \rangle$ (b.) and of the total signal of right condensate $\langle S_R \rangle$ (c). d. Relative imbalance, $\langle n \rangle = \langle S_L - S_R \rangle / \langle S_L + S_R \rangle$, as function of RF frequency. The lines in a-c are fitted Lorentzian functions to extrapolate the trap bottom.

and TB_R and the collective TB of the combined signal $S_L + S_R$, where

$$TB = \frac{TB_L + TB_R}{2} \quad (3.45)$$

In Fig. 3.8 d, we plot the measured relative imbalance $\langle n \rangle$ as a function of the RF frequency. We see that with increasing split angle α , the slope of $\langle n \rangle$

at the TB resonance ("jump" between the extrema) changes from negative to positive. The change is at the α which produces a symmetric double well. The RF frequency at the maximum and minimum of $\langle n \rangle$ marks the TB of each well. Inspired by producing imbalance $\langle n \rangle \approx 1$, we could for instance also use this as a means to produce BECs in double wells with strong imbalance.

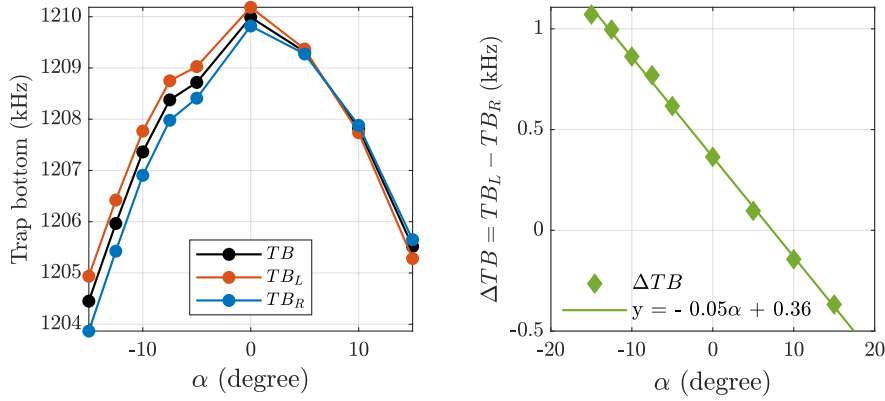


FIGURE 3.9: **Experimentally measured trap bottom as a function of split angle α in double well $\mathcal{A} = 0.65$.** Left panel: Fitted Trap bottom of left well (TB_L) and of right well (TB_R) together with the averaged TB from Fig. 3.8 as a function of split angle α which signifies the ratio between RF amplitude through the two RF wires. Right panel: the difference between left well TB_L and right well TB_R (circle marker) as a function of α together with a linear fit (solid line). A linear fit points towards a symmetric angle at $\alpha_0 \approx 7.2^\circ$.

We show in Fig. 3.9a the extrapolated trap bottoms from Fig. 3.8 with different split angles α . The TBs are symmetric around and highest at $\alpha = 0^\circ$, which matches the simulation shown in Fig. 3.10c. We show in Fig. 3.10a the simulated double well for three different values of α . The minimum of the double wells are subtracted (as shown in Fig. 3.10a).

The discrepancy between the left and right TBs,

$$\Delta TB = TB_L - TB_R, \quad (3.46)$$

shows a linear dependence on split angle, as plotted in Fig. 3.9b. A linear fit on ΔTB gives that at split angle $\alpha = 7.2^\circ$, the experimental double well is balanced in terms of energy. This is in contrast to the simulation result in Fig. 3.10d, which represents an ideal situation with perfectly balanced RF power from the two wires. The slope of ΔTB inferred from the simulation is twice as large as the experimentally probed one.

It is worth noting that for very strongly tunnel-coupled double wells, the resolution of the double well TB spectroscopy is not good enough to resolve the energy difference between the left and right well. The outcoupling RF pulse duration sets the lower bound on the frequency resolution $\Delta f = 0.05$ kHz. Other technical factors, like power broadening, also deteriorate this resolution.

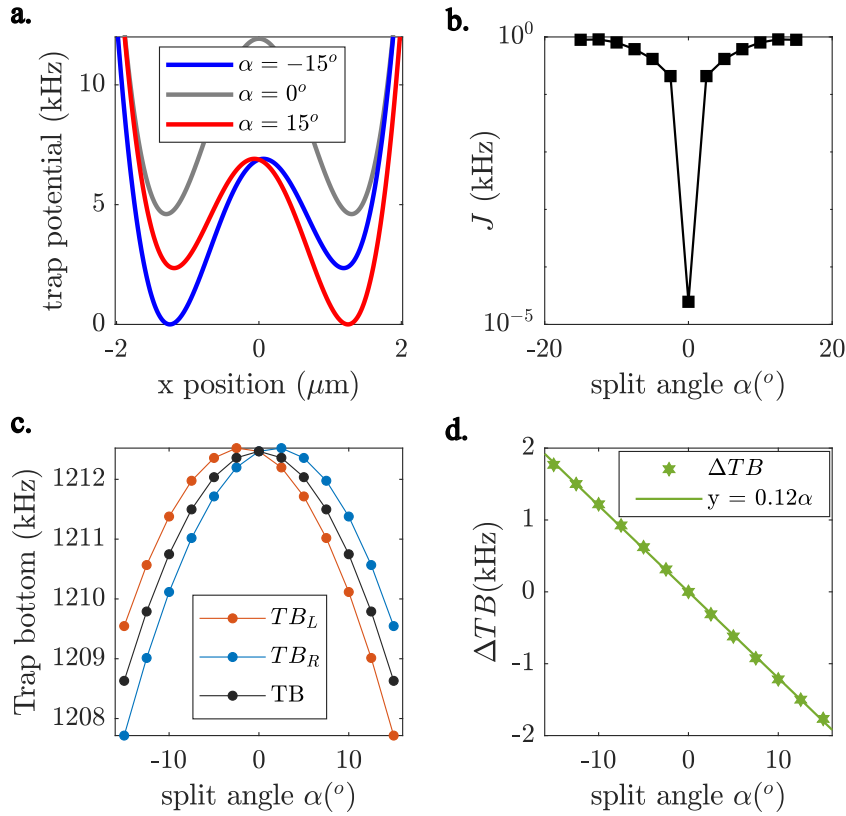


FIGURE 3.10: **Trap bottom of double well inferred from trap simulation** with $\beta = -15^\circ$ and currents through both RF wires are set to the maximal 80.25 mA. The static trap is in MZI configuration (see Tab. A.1) and dressing RF amplitude is $\mathcal{A} = 0.65$. **a.** Simulated transversal double well potentials with different split angles α (minimum energy is offset to 0). **b.** Calculated trap bottom of left (red), right well (blue) and the mean (black) as a function of α . **c.** Trap bottoms of the left well (TB_L), the right well (TB_R) and the mean TB. **d.** Trap bottom difference $\Delta TB = TB_L - TB_R$ as a function of α . As expected a symmetric double well $\Delta TB = 0$ at $\alpha = 0^\circ$.

In Fig. 3.10 **b**, we also plot the calculated tunnel coupling strength based on the two lowest single-particle eigenstates in the simulated double well. As one can see, by introducing a tilt in the decoupled double well ($J \approx 0$), one enables immediate finite tunnel coupling. This is another reason that one should also properly calibrate the double wells.

3.4.2.2 Relative imbalance

After a double well trap bottom spectroscopy which calibrates a symmetric double well in terms of equal energy minimum between the left and right well at a specific dressing amplitude \mathcal{A} . Due to experimental imperfections of the two RF wires, at different RF-dressed double wells, the split angle α_0 offering an energetically balanced double well is dressing amplitude dependent. This means that after a linear ramp-up, the α that results in zero relative imbalance $\langle n \rangle = 0$ might deviate from the estimated α_0 with a double well trap bottom spectroscopy at a particular double well.

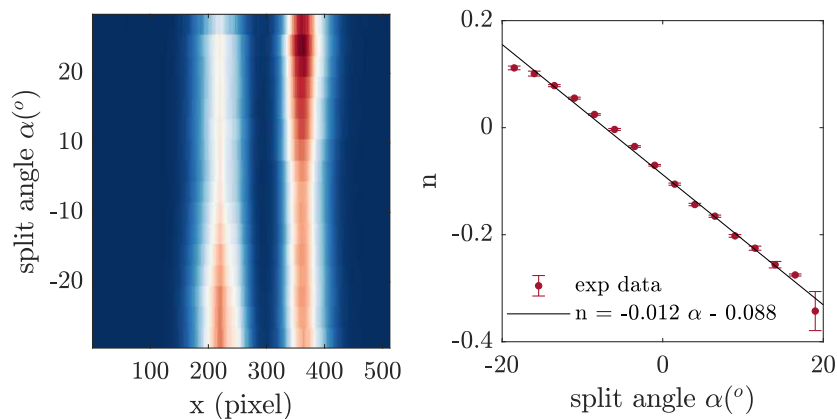


FIGURE 3.11: **Relative imbalance vs split angle** Left panel: transversal carpet with N_- readout as a result of varying split angle α Right panel: Experimentally measured relative imbalance $n = N_-/N$ as a function of α . Angle $\alpha = 7.3^\circ$ gives zero imbalance.

In Fig. 3.11 we plot the measured imbalance as a function of split angle α and its linear fit in the double well with $\mathcal{A} = 0.65$ (MZI). The linear fit estimates that $\alpha = 7.3^\circ$ gives a balanced double well $n = 0$. Here we use the same trap as the one for double well trap bottom spectroscopy in Fig. 3.9, which infers a symmetric split angle $\alpha = 7.2^\circ$. These two approaches show comparable split angles for symmetric double wells. Another way of calibrating for the symmetric double well is using the relative phase evolution over time $\langle \Phi \rangle$ whose rate is proportional to the energy difference between the two wells. The symmetric double well corresponds to a situation where $\langle \Phi \rangle$. However, this method only works for decoupled double wells, thus not suitable for the calibration of tunnel-coupled double wells. Furthermore, this calibration requires zero imbalance. More details on this can be found in Berrada's thesis [53].

3.4.3 Optimize number squeezing readout

For reading out the relative atom number, a kick sequence is applied to separate the two clouds which involves swiftly ramping up the RF amplitude right before trap release. The exact kick sequence depends on the double well that one wants to read out from. In this section, we focus on reading out from a decoupled double well¹² at $\mathcal{A} = 0.65$ and investigate how the kick amplitude influences the number squeezing factor readout and how a small imbalance affects the obtained number squeezing.

3.4.3.1 Optimize kick amplitude

The kick sequence involves 4 parameters, namely the initial double well, the rise time, the kick amplitude and the hold time in the final double well. They all play a role in the resulting transversal profile after TOF. For reading out in the relative number quadrature, we usually optimize the kick sequence with visual

¹²in the OCT trap configuration (see Tab. A.1)

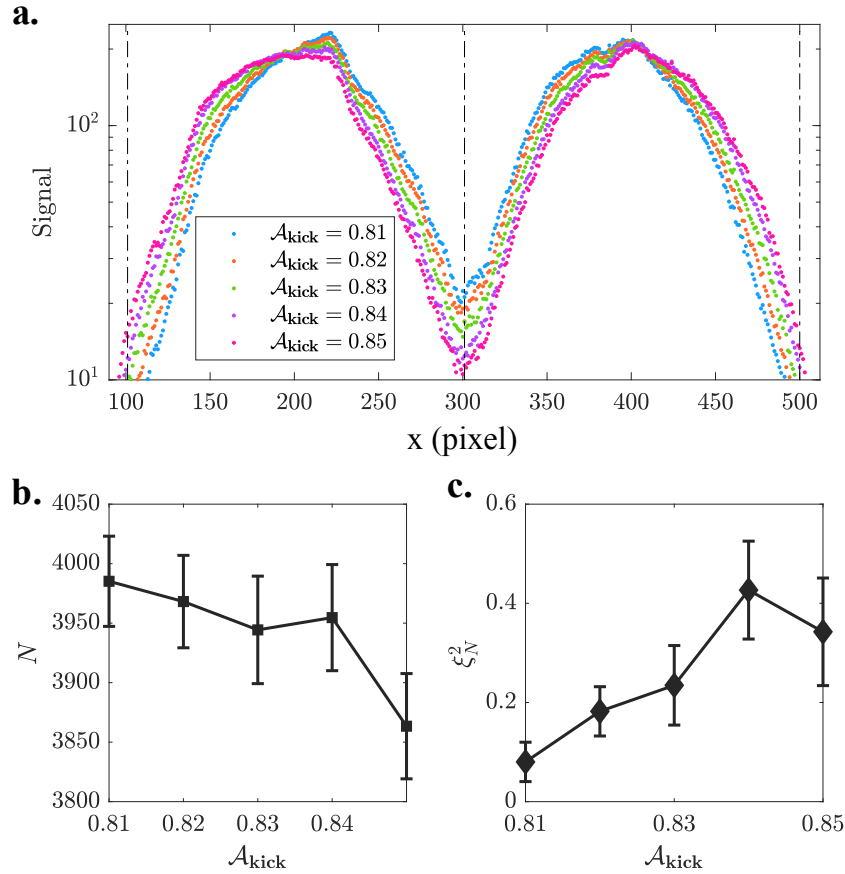


FIGURE 3.12: **Impact of kick amplitude on number squeezing factor** by evaluating on split BECs in $\mathcal{A} = 0.65$ trap with split speed $\kappa = 0.02 \text{ ms}^{-1}$. **a.** transversal profile as a function of kick amplitude $\mathcal{A}_{\text{kick}}$ which is raised up to during 0.15 ms and hold at $\mathcal{A}_{\text{kick}}$ for 0.125 ms. **b.** Total atom number within the region of interrogation. **c.** The measured global number squeezing factor, ξ_N^2 , with various $\mathcal{A}_{\text{kick}}$.

reference on the separation of the two clouds after TOF, as the parameter space is large and using the number squeezing factor as a figure of merit is very costly.

It is however not straightforward to estimate what kind of influence each parameter in the kick sequence has on the final evaluation of the number squeezing. This is especially true for strongly tunnel-coupled double wells where the overlap between the two condensates is nonnegligible. Here we investigate the influence of the kicking amplitude $\mathcal{A}_{\text{kick}}$, while the rest of the parameters are pre-calibrated. We want to emphasize that the purpose of this section is to mainly demonstrate the influence of kick sequence on the evaluation of the number squeezing factors. We do not claim that everything is fully understood.

First, we prepare BECs in a decoupled double well $\mathcal{A} = 0.65$ by splitting from a single well with speed $\kappa = 0.02 \text{ ms}^{-1}$ at a constant split angle $\alpha = 9.5^\circ$. To read out the number squeezing factors, we linearly ramp up the RF amplitude to $\mathcal{A}_{\text{kick}}$ in 0.15 ms and hold at $\mathcal{A}_{\text{kick}}$ for 0.125 ms. We show in Fig. 3.12a the averaged transversal profiles with varying kick amplitude and in **b** the detected total atom number within the ROI (marked by black vertical lines in **a**). As one

can see the clouds become more spatially separated as kick amplitude increases. At the same time, there is a slight decrease of detected atom number up until $\mathcal{A}_{\text{kick}} = 0.84$. Beyond this amplitude, the detected atom number drops suddenly. We estimate that at $\mathcal{A}_{\text{kick}} = 0.85$, around 5% of atoms land outside the field of view.

Fig. 3.12c shows the detected number squeezing factors as a function of $\mathcal{A}_{\text{kick}}$. It is surprising how the kick amplitude has such a strong influence on the final evaluation of number squeezing. A difference in the detected number squeezing factor ~ 0.3 corresponds to a difference in relative atom number variance ΔN_-^2 of ~ 1000 atoms. To rule out any other possible sources of errors, we also directly looked at the uncorrected variance of the primary photons $\Delta^2 S_-$, which shows the same trend and yields a difference of $\sim 1 \cdot 10^4$ photons (with average photons per atom $\bar{p} = 10.5$) between $\mathcal{A}_{\text{kick}} = 0.81$ and $\mathcal{A}_{\text{kick}} = 0.84$. The source of this large deviation is yet unknown. It is unlikely that the overlapped region between the two condensates in the centre can lead to such a large difference since it is only a matter of a few atoms as we can see in Fig. 3.12a.

For consistency, when reading out the relative number, especially in Chpt. 6, we always fix the kick sequence. This effect of kick sequence is also more significant for the decoupled traps, compared to tunnel-coupled traps, due to the limited field of view on the fluorescence imaging camera. To eliminate doubts about enhanced number squeezing as an artefact of the readout, we will show later other evidence of improved number squeezing such as reduced phase diffusion rates in Sec. 7.2.

3.4.3.2 Optimize imbalance

Despite careful calibration on symmetric double wells as discussed in Sec. 3.4.2, it is still experimentally challenging to achieve a complete symmetric splitting. Thus we deliberately investigate how a small imbalance influences the resulting number squeezing. We emphasize that contrary to the previous subsection on kick amplitude, where the influence is on the readout procedure, here we examine the influence of the actual quantum state.

We prepare the different imbalances by changing the split angle α when split from a single well to a decoupled double well $\mathcal{A} = 0.65$ at split speed $\kappa = 0.02 \text{ ms}^{-1}$. We show in Fig. 3.13a the resulting number squeezing factors at various split angles α . The best number squeezing is achieved at $\alpha = 9^\circ$. The corresponding imbalances $\langle n = N_-/N \rangle$ are displayed in Fig. 3.13b. From the mean imbalance n , we identify the symmetric split angle $\alpha \approx 9.3^\circ$. It is slightly puzzling since even though the imbalance at $\alpha = 9.5^\circ$ is smaller than at $\alpha = 9^\circ$, the obtained number squeezing is better at $\alpha = 9^\circ$. One of the possible reasons is that the fluorescence imaging light is inhomogeneous so that the averaged photons per atoms \bar{p} is nonconstant across the ROI. This could lead to small deviations in the calibration of imbalance. Namely, the calculated imbalance

$$n = \frac{S_L - S_R}{S_L + S_R} = \frac{\bar{p}_L N_L - \bar{p}_R N_R}{\bar{p}_L N_L + \bar{p}_R N_R} \neq \frac{N_L - N_R}{N_L + N_R}, \quad (3.47)$$

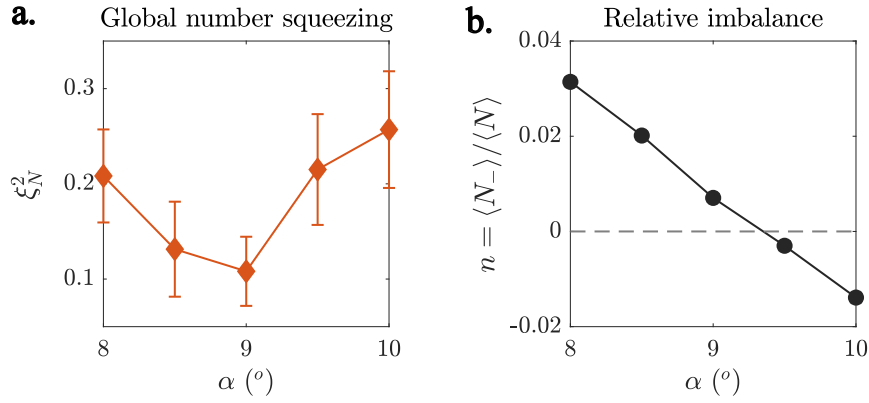


FIGURE 3.13: **Impact of relative imbalance on number squeezing** with kick amplitude $\mathcal{A}_{\text{kick}} = 0.81$ from Fig. 3.12. We prepare a slight initial imbalance, n , between the two split condensates by varying the ratio of the RF amplitudes using split angle α ,

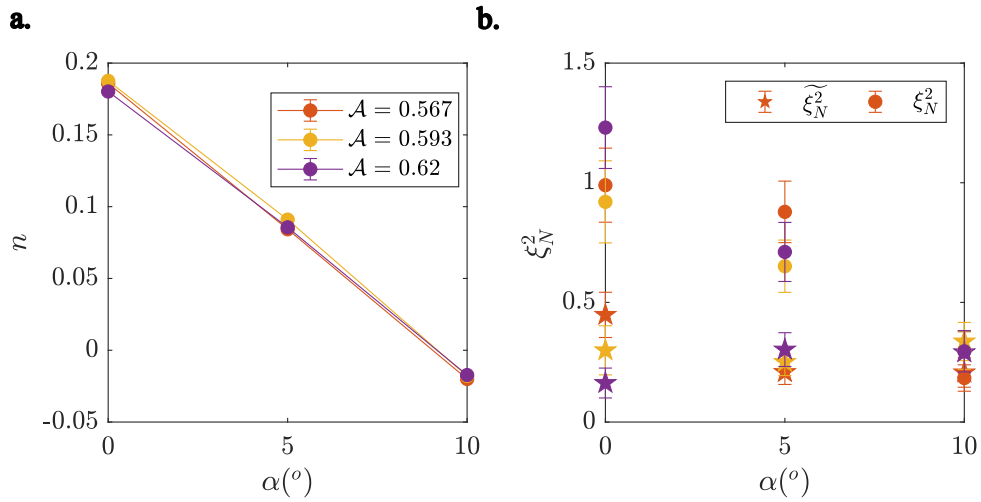


FIGURE 3.14: **Number squeezing factor with strong imbalance** **a.** Preparing states with stronger imbalance with split angle α in various tunnel-coupled double wells, denoted as \mathcal{A} . **b.** Evaluated number squeezing factors based on Eq. (3.18) (dot markers) and based on Eq. (3.29) (star markers).

since the photon per atom of the left condensate \bar{p}_L and of the right condensate \bar{p}_R is nonequal, $\bar{p}_L \neq \bar{p}_R$. Assuming a real zero imbalance at $\alpha = 9^\circ$, we estimate a difference of the photon per atom between the ROI for the left and right condensate to be $\sim 0.5\%$, which is rather insignificant. Thus we hereon disregard the influence of inhomogeneous \bar{p} on the number squeezing factor.

The presented number squeezing factors in Fig. 3.13a is calculated based on Eq. (3.18) where zero imbalance is presumed. Using the revised number squeezing formula Eq. (3.29) to calculate, we obtain very compatible results $\widetilde{\xi}_N^2 \simeq \xi_N^2$. This is possibly due to that the introduced imbalance is still too small to result in significant changes in number squeezing. But it is good confirmation that with small imbalances, Eq. (3.18) gives the right number squeezing factor

In order to check the influence of the revised number squeezing factor (defined

in Eq. (3.29)) which works for any imbalances, we prepare BECs in double wells with stronger imbalances. In Fig. 3.14 we compare estimated number squeezing factors ξ_N^2 from Eq. (3.18) and $\widetilde{\xi_N^2}$ from Eq. (3.29) of BECs with strong imbalances (up to $n \approx 0.2$) in various tunnel-coupled double wells. We see that for negligible imbalances $n \approx 0$ at split angle $\alpha = 10^\circ$, there are no visible differences between ξ_N^2 and $\widetilde{\xi_N^2}$. With larger imbalances at $\alpha = 5^\circ$ and $\alpha = 0^\circ$, the discrepancy between ξ_N^2 and $\widetilde{\xi_N^2}$ becomes more significant. We also note that the resulting number squeezing factors $\widetilde{\xi_N^2}$ in more tunnel-coupled double wells $\mathcal{A} = 0.567$ decreases with smaller imbalances.

With the previous discussion, we remark that Eq. (3.18) and Eq. (3.29) are comparable at small imbalances. We will be using Eq. (3.18) for evaluation in the remainder of the thesis, where only balanced BECs are generated.

Chapter 4

Preparation of BECs in double wells

In this chapter, we are presenting some experimental observations and the corresponding discussions on two approaches to experimental preparation of BECs in a double well (shown in Fig. 4.1). The first approach is by directly evaporative cooling into a double well. The second approach involves splitting a BEC in a single well by smoothly modifying the trapping potential to a double well.

On the contrary to Chap. 5, we aim to prepare BEC in double wells at its classical stable fixed point, namely $\langle n \rangle = \langle \Phi \rangle = 0$. We investigate the fluctuations of the observables which originate from either thermal or quantum properties. We compare the two approaches in terms of fluctuations in both conjugate observables and discuss emerging phenomena one can investigate with each approach.

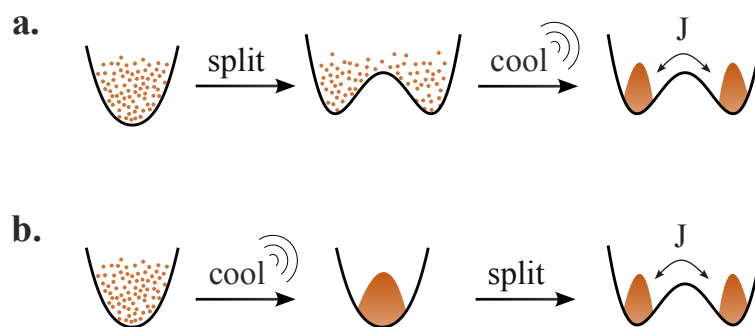


FIGURE 4.1: **Preparing BECs in a double well a.** Direct Cooling: We first transform a single well into a double well and condense the thermal cloud into BECs in a double well with evaporative cooling. **b.** BEC splitting: We first prepare a BEC in a single well with evaporative cooling and split a BEC into two by ramping up the RF dressing amplitude to transform it into a double well.

4.1 Direct cooling

The direct cooling approach implies preparing first a double well with thermal gas and performing evaporative cooling in the double well to achieve one condensate in each well (in Fig. 4.1a). With this approach, the fluctuations of the

quantum observables in the relative degree of freedom between the two condensates are dominated by thermal noises. This approach was first used in the MIT experiment [69] to demonstrate BEC as a coherent wave source.

In the experiment, in order to perform direct cooling into double wells, the evaporative cooling sequence needs to be adjusted accordingly. The evaporation sequence consists of segments of frequency sweeping while the RF power is kept constant within each segment. The evaporation shape, P , which is the exponent of the frequency sweeps, $\nu(t) \propto \nu_0 \exp(1/Pt)$, needs to be reduced compared to the standard sequence for cooling into a single well. The initial RF evaporation frequency ν_0 and the evaporation duration can also be scanned to optimise the sequence. After the optimization, we managed to cool into a range of double wells up to $\mathcal{A} = 0.6$. In principle, cooling into more decoupled double wells is also possible. But as we will see later, the fringe visibility becomes very poor for more decoupled double wells and is hard to gain information from with the current imaging resolution.

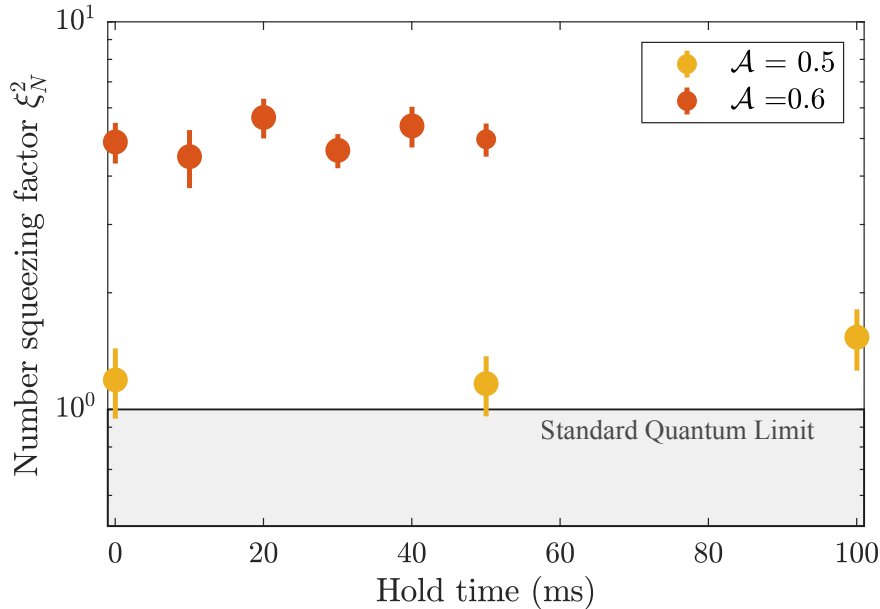


FIGURE 4.2: **Number fluctuation with direct cooling into double wells** Measured number squeezing factor, ξ_N^2 after direct cooling into double wells $\mathcal{A} = 0.5$ and 0.6 as a function of hold time after cooling.

In Fig. 4.2, we show the measured number squeezing factors with direct cooling into a strongly tunnel-coupled double well at $\mathcal{A} = 0.5$ and a weakly tunnel-coupled double well at $\mathcal{A} = 0.6$. After the initial preparation, we hold the BECs in the trap for up to 100 ms to check their stability and heating rate. As one can see, the number squeezing factors remains quite constant over the holding time. This is the first indication of the effectiveness of the direct cooling sequence.

As for the values of the obtained number squeezing factor ξ_N^2 in Fig. 4.2, we can understand this with the thermal occupation of the plasmon modes in the BJJ

at finite temperature T [70],

$$N_p = \frac{1}{\exp(\hbar\omega_p/k_B T) - 1}, \quad (4.1)$$

where N_p is the occupation number and $\hbar\omega_p$ is plasmon energy. We recall the angular frequency $\omega_p = 2\pi f_p$ with f_p representing the plasma frequency as defined in Eq. (5.3). It has been shown in [70], that the Josephson plasmon can be treated as Bogoliubov quasiparticles of the BJJ. In less tunnel-coupled double wells by employing larger RF dressing amplitude \mathcal{A} , the plasmon energy $\hbar\omega_p$ decreases. See Fig. 3.3 for exponentially decreasing tunnel coupling strength with \mathcal{A} . This means that the occupation number N_p is thus much higher in less tunnel-coupled traps at the same temperature T . The plasmon energies correspond to $\hbar\omega_p/k_B \approx 15$ nK for $\mathcal{A} = 0.5$ and 1 nK for $\mathcal{A} = 0.6$.

The relative number fluctuations between BECs at finite temperatures obey

$$\langle \Delta N_-^2 \rangle_{T>0} = (2N_p + 1) \langle \Delta N_-^2 \rangle_{T=0}, \quad (4.2)$$

where $\langle \Delta N_-^2 \rangle_{T=0}$ indicates the quantum fluctuations of the ground state in BJJ at zero temperature. From the BJJ Hamiltonian in Eq. (2.23), we can deduce the expected ground state fluctuations to be $\langle \Delta N_-^2 \rangle_{T=0} = N/\sqrt{1+\Lambda}$. Thus, the expected number squeezing factors at finite temperatures can be expressed as

$$\xi_{N,T}^2 = (2N_p + 1) \xi_{N,0}^2 = \frac{2N_p + 1}{\sqrt{1+\Lambda}}. \quad (4.3)$$

With direct cooling, the thermal noise dominates the fluctuations in the relative degree of freedom with $N_p \ll 1$. And as expected, the measured number squeezing factors from BEC with finite temperatures $\xi_{N,T}^2|_{T>0}$ in Fig 4.2 are much larger in the less tunnel-coupled double well.

Conversely, from measured plasma frequencies ω_p and analytically estimated ground state squeezing factors $\xi_{N,0}^2$ in Eq. (4.3), we can in principle infer the temperatures of BECS obtained with direct cooling. Based on the squeezing factors in Fig. 4.2, we can estimate the temperature to be $T \approx 30$ nK in the $\mathcal{A} = 0.5$ trap and $T \approx 150$ nK in the $\mathcal{A} = 0.6$ trap. Note that in order to correctly estimate $\xi_{N,0}^2$ for $\mathcal{A} = 0.6$ trap, we insert the experimentally measured plasma frequency to Eq. (5.3) to derive Λ . This is because the interaction broadened transversal profile increases tunnel coupling compared to estimated from single-particle eigenstates in Fig. 3.3. The influence of this broadening becomes more pronounced in less tunnel-coupled traps.

In Fig. 4.3, we show the measurements in the conjugate phase quadrature resulting from direct cooling. We infer quantities involving both the global phase and the local observables. First, the standard deviation of the global phase $\Delta\Phi$ estimates the distribution of the global phase. This is the complementary quantity to the number squeezing factors. With direct cooling into a strongly coupled double well $\mathcal{A} = 0.5$, the obtained average global phase squeezing factor (defined as in Eq. (3.41)) is $\xi_{\Phi}^2 \sim 100$. This is much larger than the expected ground state phase squeezing factor at zero temperature, which we attribute to

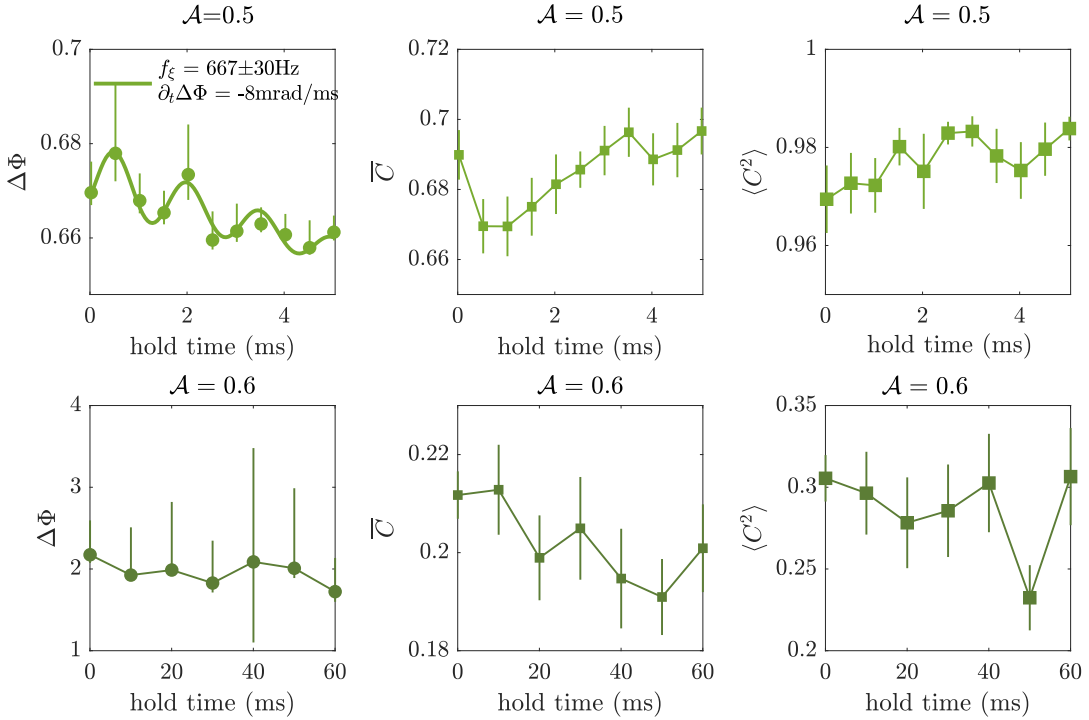


FIGURE 4.3: **Phase fluctuations with direct cooling into double wells** with $\mathcal{A} = 0.5$ (Upper panel) and $\mathcal{A} = 0.6$ trap (Lower panel). $\Delta\Phi$ is the standard deviation of the global phase. \overline{C} is the averaged single-slice fringe visibility averaged over the central region of the condensates. $\langle C^2 \rangle$ is the spatial phase coherence factor.

the thermal occupation of Josephson plasmon, similar to the number squeezing factor in Eq. (4.2). The global phase fluctuation $\Delta\Phi$ exhibits oscillatory dynamics over time after cooling into the double well. This dynamical evolution is highly interesting and will be investigated further in Chap. 6. In addition, we see that $\Delta\Phi$ decreases over time with a rate $\partial_t \Delta\Phi = -8 \text{ mrad/ms}$. This rephasing stems from the phase-locking mechanism introduced by the strong tunnel coupling. On the other hand, in the weakly tunnel-coupled double well at $\mathcal{A} = 0.6$ (lower panels in Fig. 4.3), the global phase distribution is completely randomized, characterized with $\Delta\Phi \approx 2$. This is a sign of weak tunnel coupling $J \approx 0$.

The average contrast of single-pixel interference pattern \overline{C} serves primarily as a measure of first-order phase coherence. This verifies BECs as a phase coherent matter-wave source. In the case of 1D quasicondensates, the coherence length along the single condensates, λ_T , reduces as the temperature increases (see Eq. (2.64)). At higher temperatures, λ_T falls below the imaging resolution, resulting in a decrease in the visibility of interference patterns on the single pixel level¹. For instance, we see in the middle panels in Fig. 4.3 that $\overline{C} \approx 0.2$ in the weakly coupled double well. For strongly coupled quasicondensates, the coherence length of the relative phase is restored by the tunnel coupling (see the upper middle panel in Fig. 4.3).

¹See [71] for more detail on the full distribution function of contrast.

Lastly, we infer the mean square contrast

$$\langle C^2 \rangle = \sum_{z, z'} \mathcal{C}(z, z'), \quad (4.4)$$

where the spatial phase coherence factor $\mathcal{C}(z, z')$ is defined in Eq. (2.63). $\langle C^2 \rangle$ gives an impression of the overall spatial phase coherence, which is a result of the interplay between the thermal coherence length and phase restoration length of the double well [72]. Thus it provides insight into both the BEC temperature from the direct cooling and the tunnel coupling strength of the double well. The mean squared contrast $\langle C^2 \rangle \approx 1$ in $\mathcal{A} = 0.5$ indicates a strong tunnel coupling. $\langle C^2 \rangle \approx 0.3$ in $\mathcal{A} = 0.6$ shows a weaker but non-vanishing tunnel coupling. In addition, we observe an oscillatory behaviour of $\langle C^2 \rangle$, which is connected to the evolution of non-equilibrium states (discussed more in Chap. 6).

In this section, we gain some quantitative insight into the direct cooling approach which prepares BECs in double wells at thermal equilibrium. However, with the dominant thermal noise in the relative atom number fluctuations, such an approach is not feasible for preparing strongly correlated BECs in double well at the quantum regime.

4.2 BEC splitting

The other approach is to first evaporative cool into a single well and split this initial condensate into two by ramping up the amplitude of the RF dressing linearly. We usually start with a single quadratic trap with small dressing amplitude $\mathcal{A} = 0.28$ to avoid equal energy level spacing and drastic change in longitudinal trap frequency compared to the static trap.

The BEC splitting approach is a well-known procedure [73]. When performed adiabatically, the system can follow the ground state of the time-dependent Hamiltonian. However, during the splitting process, the two lowest eigenstates become energetically degenerate at some point. Namely, $1/J$ blows up. In the many-body system, the adiabatic condition can be formulated as [74]

$$|\dot{\omega}_p| \ll \omega_p^2, \quad (4.5)$$

here again, ω_p is the plasma frequency. This means that the adiabaticity is inevitably broken when splitting to decoupled double wells, $\omega_p \approx 0$. In the case of a simple linear ramp-up of the RF dressing amplitude, a true adiabatic splitting dictates an infinitely slow splitting.

We show in Fig. 4.4 the obtained number squeezing factors in number and phase quadrature in various double wells, noted as \mathcal{A} , after a single ramp-up [75] from the single well $\mathcal{A} = 0.28$ at a constant splitting speed

$$\kappa = \frac{\delta \mathcal{A}}{\delta t} = 0.02 \text{ ms}^{-1}. \quad (4.6)$$

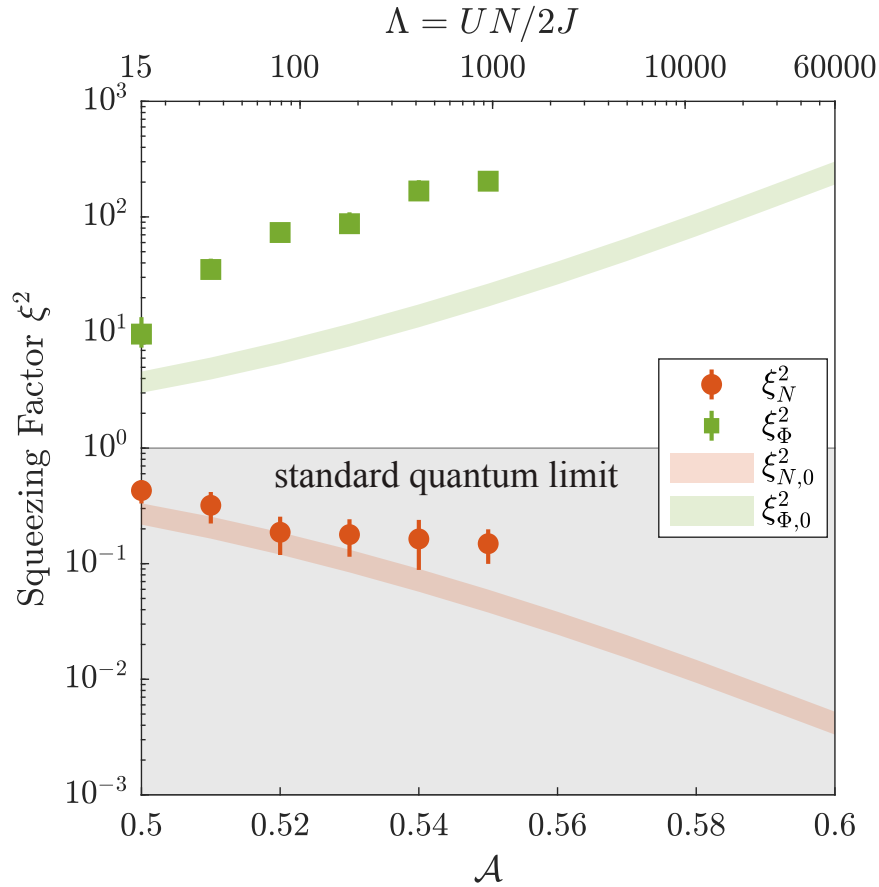


FIGURE 4.4: **Measured squeezing factors in double wells.** Squeezing factors directly measured after splitting from a single well to a double well \mathcal{A} with splitting speed $\kappa = 0.02\text{ms}^{-1}$. The standard quantum limit is marked as a solid grey line. Shaded regions represent ground state fluctuations at zero temperature with atom number $N = [2000, 5000]$.

Splitting speed here is an indirect indicator for the adiabaticity condition

$$\dot{\omega}_p \propto \dot{J} = \frac{\partial J}{\partial \mathcal{A}} \cdot \kappa. \quad (4.7)$$

When first entering the Josephson regime by transforming the double well, the adiabaticity condition in Eq. (4.5) is easy to fulfil, as $\omega_p \gg 1$. But as the tunnelling strength decreases exponentially as shown in Fig. 3.3, the adiabaticity condition is bound to be broken during the BEC splitting with a finite duration.

As we prepare our system around the stable fixed point of the phase space, $\langle N_- \rangle = 0$ and $\langle \Phi \rangle = 0$, provided small fluctuations in the lower energy states, the BH Hamiltonian in Eq. (2.23) can be further linearized and expressed in harmonic approximation as

$$H_{hc} = \frac{\hbar f_p}{2} \left(\frac{\Phi^2}{2\Delta_0 \Phi^2} + \frac{N_-^2}{2\Delta_0 N_-^2} \right), \quad (4.8)$$

where the ground state fluctuations are

$$\Delta_0 N_-^2 = \frac{N}{\sqrt{1+\Lambda}}, \quad \text{and} \quad \Delta_0 \Phi^2 = \frac{\sqrt{1+\Lambda}}{N}. \quad (4.9)$$

With this, we can estimate the expected ground state squeezing factors of BH model to be

$$\xi_{N,0}^2 = \frac{1}{\sqrt{1+\Lambda}}, \quad \text{and} \quad \xi_{\Phi,0}^2 = \sqrt{1+\Lambda}. \quad (4.10)$$

The shaded bands in Fig. 4.4 are the expected ground state squeezing factors at zero temperature [76] based on the harmonic approximation of BJJ in Eq. (2.23). The total atom numbers of the experimental results are on average ≈ 4000 . As one can see in Fig. 4.4, in more strongly coupled double wells with large plasma frequency, the obtained number squeezing factors with BEC splitting are close to the expected ground state squeezing factor $\xi_{N,0}^2$.

On the other hand, the phase squeezing factor is on average an order of magnitude above the expected phase squeezing factor $\xi_{\Phi,0}^2$. Generally, this is due to the inter-atomic interaction-induced phase diffusion during the splitting procedure. For very strongly coupled double wells, the readout error on the relative phase also inserts a lower bound on the evaluated ξ_{Φ}^2 .

With typical linear ramps, the phase space fluctuations end up larger than the Heisenberg limit, $\xi_N^2 \cdot \xi_{\Phi}^2 \gg 1$. This is first of all due to the interaction-induced phase diffusion during the ramp-up. Secondly, the adiabaticity condition is no longer fulfilled at one point during the finite ramp. However, BECs splitting still places the fluctuations in the relative degree of freedom in the quantum regime. Based on these findings, we investigate on the dynamics of quantum fluctuations of the many-body system in a finitely tunnel-coupled double well in the following chapters.

Chapter 5

Mean-field dynamics in bosonic Josephson junction

In this chapter, we study the emerging mean-field dynamics between tunnel-coupled BECs, realising an extended bosonic Josephson junction. This mirrors the well-known Josephson effect [77] observed in superconductors and other macroscopic quantum systems [78]. We delve into the experimental aspects of Josephson oscillations in tunnel-coupled BECs. In Sec. 5.1 we will treat the BEC as a macroscopic system and only consider the dynamics in the global degree of freedom. In Sec. 5.2, we investigate the local Josephson oscillations along the tunnel-coupled 1D quasicondensates to investigate their dependence on atomic density and furthermore how local Josephson oscillations along the condensates are coupled.

5.1 Global Josephson oscillations

The main experimental association of the Josephson oscillations realised with BECs is mostly restricted to the mean-field dynamics between two macroscopic quantum states. In the classical picture ($N \rightarrow \infty$), the BH Hamiltonian for asymmetric double wells can be expressed as

$$H = \frac{\Lambda}{2} n^2 - \sqrt{1 - n^2} \cos \Phi + \Delta E \cdot n, \quad (5.1)$$

where $n = N_-/N$ is the relative imbalance, Φ is the relative phase and $\Delta E = E_L^0 - E_R^0$ is the zero point energy difference between the left and right well. From this rigid pendulum equation, one can derive the time evolution of the two observables which are two coupled first-order differential equations

$$\begin{aligned} \dot{n}(t) &\approx -\frac{2J}{\hbar} \sqrt{1 - n^2} \sin \Phi(t), \\ \dot{\Phi}(t) &\approx \frac{NU}{\hbar} n(t) + \frac{2J}{\hbar} \frac{n(t)}{\sqrt{1 - n^2(t)}} \cos \Phi(t) + \Delta E. \end{aligned} \quad (5.2)$$

By introducing an initial offset with either $n(0) \neq 0$ or $\Phi(0) \neq 0$, one can observe a Josephson oscillation in both quadratures of the mean values $\langle n(t) \rangle$

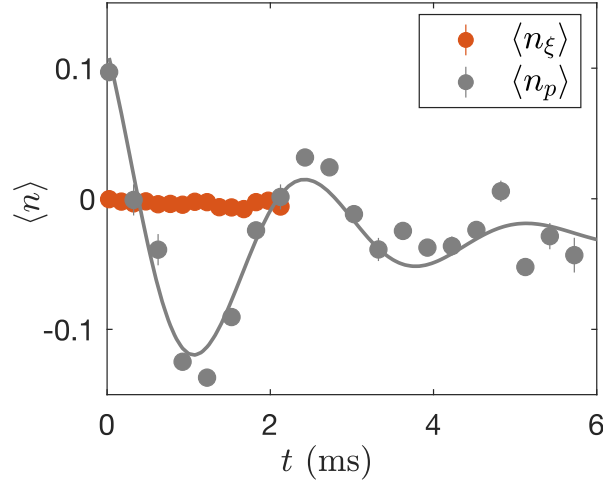


FIGURE 5.1: **Extracting plasma frequency experimentally.** Evolution of the expectation value of relative imbalance $\langle n \rangle = \langle N_-/N \rangle$ in a coupled double well. By introducing an initial imbalance $\langle n_p(0) \rangle > 0$, the mean value (grey marker) undergoes a Josephson oscillation. While for typical symmetric splitting, $\langle n_\xi \rangle$ (orange marker) remains around zero.

and $\langle \Phi(t) \rangle$. We show an exemplary measurement in Fig. 5.1 with grey markers. The oscillation frequency is expressed as

$$f_p = \frac{2J}{h} \sqrt{\cos \Phi_0 + \Lambda}, \quad (5.3)$$

where Φ_0 is the initial relative phase. This frequency f_p is usually referred to as plasma frequency [39]. Though not predicted by Eq. (5.2), we observe a relaxation of the Josephson oscillations in our tunnel coupled 1D BECs. This has been investigated to a great extent by M. Pigneur, et.al. [23], where an empirical damping term is added. Later a numerical investigation with 3D GPE simulations by J.F. Mennemann [24] was conducted. The authors found that the damping in both global and local Josephson oscillations are related to the dephasing of free quasiparticle modes in the low-energy effective sine-Gordon model. The relaxation to the phase-locked state is associated with the breakdown of the field theory. Experimentally, we simply use a damped pendulum model to fit the Josephson oscillations

$$\frac{\partial^2}{\partial t^2} \Phi(t) + \eta \frac{\partial}{\partial t} \Phi(t) + \omega_p^2 \sin \Phi(t) = 0, \quad (5.4)$$

where η is the damping factor and $\omega_p = 2\pi f_p$ is the angular frequency. The solid grey line in Fig. 5.1 is the fitted result. From the expression in Eq. (5.3), we see that the plasma frequency f_p depends on two tunable parameters: the tunnel coupling strength J and the total atom number N .

Experimentally, we can adjust J by modifying the RF amplitude \mathcal{A} . Atom number N is tuned by changing the final frequency of the evaporation cooling. We performed Josephson oscillation measurements in the OCT trap configuration by varying both the RF amplitude \mathcal{A} and atom number N . The extrapolated

plasma frequencies (circle markers) are shown in Fig. 5.2. We also plot the derived plasma frequencies based on Eq. (5.3) (solid lines) with obtained J from the trap simulation (Fig. 3.3).

It is important to note that for less tunnel-coupled double wells, a small initial imbalance could already lead to self-trapping [73]. This is identified as the mean values of imbalance oscillate around a nonzero value, $\langle n(t) \rangle \neq 0$, and the relative phase grows linearly beyond 2π . Thus very precise preparation of the initial conditions is needed to track Josephson oscillations in the less tunnel-coupled double wells. Additionally, the estimation as J based on single particle eigenenergies is not very precise, since the repulsive interactions alter effective eigenstates and the transversal swelling is total atom number dependent.

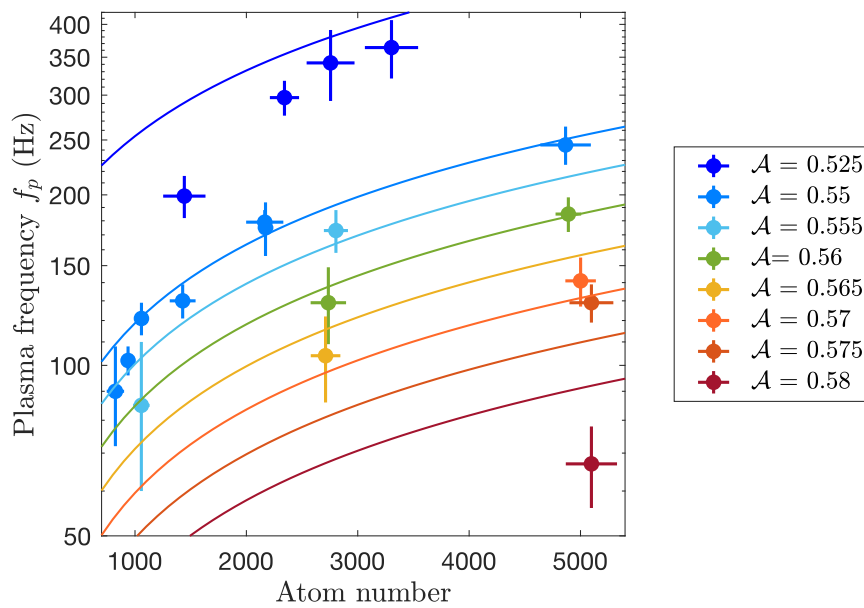


FIGURE 5.2: **Experimentally measured plasma frequencies.** The plasma frequency is measured with relative phase readout in double wells, represented by RF amplitudes \mathcal{A} , with varying atom numbers in the OCT trap configuration. Circle markers are experimental results. Solid lines are plasma frequencies from Eq. (5.3) by inserting extrapolated J from simulation with $\beta = 8.5^\circ$.

The measurements are performed with Tabor AWG as the RF dressing source. Since we know from the comparison of inter-well distance in Fig. 3.7 that Tabor AWG delivers weaker dressing, we set $\alpha = 8.5^\circ$ in the simulation to match with the experimental inter-well distance.¹ This serves as a good guideline for qualitative comparison.

In principle, we do not expect a quantitative match between the experimentally measured plasma frequencies and the approximated analytical expression in Eq. (5.3). This is mostly because the tunnel-coupling strength J used in Eq. (5.3) is based on Eq. (3.13) where single particle eigenstates are used. While

¹Ideally, one would also acquire a match in terms of trap frequencies, but this is not measured systematically on the experiment with Tabor AWG.

in reality, the interaction broadens the transversal wavefunctions, thus the real J is larger than the estimation based on Eq. (3.13). When cooling into higher final evaporation frequencies, the produced BECs are at higher thermal temperatures and potentially with larger thermal fractions. The influence of thermal temperatures on Josephson oscillations is not investigated further in this thesis. But we refer to a theoretical study on Josephson oscillation between tunnel-coupled BECs at finite temperatures [30]. There the authors showed that thermal noises lead to decreasing plasma frequencies. In addition, simulation results with 3D GPE [24] suggest that the plasma frequency scaling is not simply $f_p \propto \sqrt{N}$. Single-particle tunnel coupling J contributes additionally to the exponent. To confirm this experimentally, a larger range of atom numbers is needed, which is challenging within the current trap configurations.

5.2 Density dependent Josephson oscillations

Aside from the global Josephson oscillations, by treating the quasicondensates as arrays of individual BECs, we anticipate observing oscillations in the local observables, i.e. relative density $\rho_-(z)$ and relative phase $\phi(z)$. Without much introduction into the equation of motion of the phase field (valid in both quantum and classical picture) based on the sine-Gordon model in Eq. (2.77) (see Sec. 2.3.2.2)

$$\frac{\partial^2}{\partial t^2} \phi(z, t) - c^2(z) \frac{\partial^2}{\partial z^2} \phi(z, t) + \omega_p^2(z) \sin \phi(z, t) = 0, \quad (5.5)$$

where the local plasma frequency $\omega_p(z)$ and local phonon speed $c(z)$ are

$$\omega_p(z) = \sqrt{\frac{4Jg_{1D}\rho(z)}{\hbar}}, \quad c(z) = \sqrt{\frac{g_{1D}\rho(z)}{m}}, \quad (5.6)$$

and $\rho(z)$ is the atomic density in the split condensates (assuming $\rho_L(z) \approx \rho_R(z)$). With a harmonic magnetic trap, the longitudinal atomic density $\rho(z)$ is inhomogenous. By assuming that there is no phase gradient along the condensates, $\partial_z \phi(z, t) = 0$, we can further simplify the expression in Eq. (5.6). Moreover, we add an additional damping term as a continuation of our discussion on the relaxation of Josephson oscillations in Sec. 5.1. Thus the local Josephson oscillations can be described by

$$\frac{\partial^2}{\partial t^2} \phi(z, t) + \eta(z) \frac{\partial}{\partial t} \phi(z, t) + \omega_p(z) \sin \phi(z, t) = 0, \quad (5.7)$$

with $\eta(z)$ and $\omega_p(z) = 2\pi f_p(z)$ are independently fitted at each spatial position z . We show in Fig. 5.3a examples of the induced local Josephson oscillations in a strongly coupled double well at $\mathcal{A} = 0.5$ (MZI) at three different z positions.

The presented experimental result in Fig. 5.3 is initialised by directly cooling into a tilted double well at $\mathcal{A} = 0.5$ trap in the MZI trap configuration (see

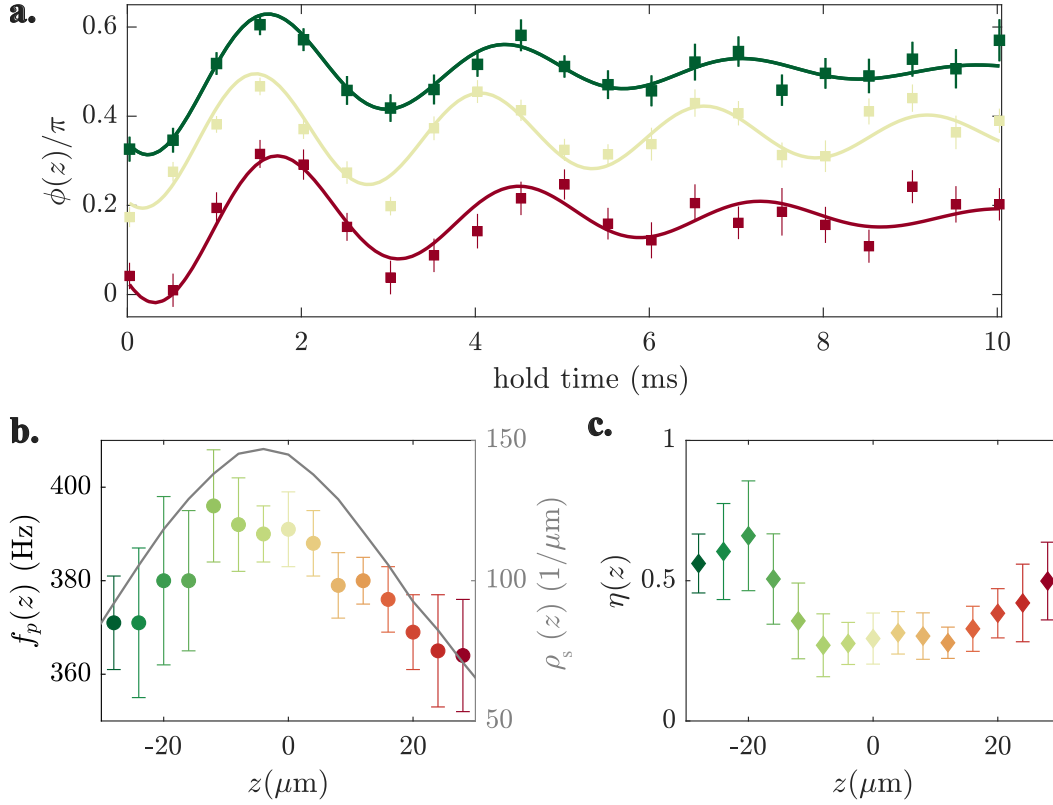


FIGURE 5.3: **Density dependent Josephson oscillations** **a.** spatially resolved Josephson oscillations in strongly coupled double well $\mathcal{A} = 0.5$ (MZI). **b.** Extracted local plasma frequencies along the condensates. $z = 0$ remarks the centre of the condensate. The grey solid line shows the total 1D atomic density profile, corresponding roughly to twice the atomic density in each condensate $\rho_s(z) \approx 2\rho(z)$. **c.** Extracted local damping rate at position z .

Tab. A.1). Thus a non-zero initial imbalance is prepared², $n \neq 0$, as shown in Fig. 5.4. Then we tilt to the symmetric double well by adjusting the split angle α (see Sec. 3.4.2 for more details) and hold in the symmetric double well for a variable time for Josephson oscillation. To read out the local relative phase with better resolution, we swiftly ramp up to the decoupled trap $\mathcal{A} = 0.68$ right before trap release.

In the weakly interacting regime, the Thomas-Fermi approximation, $\delta\rho(z)/\rho(z) \ll 1$, can be used to describe the longitudinal profile of the condensates

$$\rho(z) = \rho_0(1 - \tilde{z}^2), \quad \tilde{z} = \frac{z}{R_{TF}}, \quad (5.8)$$

where R_{TF} is the Thomas-Fermi radius. In the strongly tunnel-coupled trap $\mathcal{A} = 0.5$, the trap simulation infers a tunnel coupling strength is $J = 75$ Hz and we estimate the interaction strength $g_{1D}/h \approx 20$ Hz \cdot μm based on Eq. (2.46).

²For this measurement, the Stern-Gerlach separation routine is used. We summed up the imbalance in each mF state to estimate the imbalance n . It is not yet clear how Stern-Gerlach influences the imbalance readout, as the imbalance of each mF state after separation is very different from each other.

Inserting these into Eq. (5.6), we expect local plasma frequencies to have a dependence on the atomic density $f_p(z) \approx \sqrt{\rho(z)} \cdot 80 \text{ Hz} \cdot \mu\text{m}^{\frac{1}{2}}$. In Fig. 5.3b, the total atomic density of the two condensates is plotted as a function of the spatial position z (grey line). The atomic densities in each condensate are thus roughly half of the plotted values $\rho(z) = \rho_s(z)/2$. The fitted plasma frequencies in Fig. 5.3 show a dependence on the longitudinal atomic density. As we can see, the variation in plasma frequencies along the condensates is much smaller than the expected density dependence $f_p \propto \sqrt{\rho}$ from Eq. (5.6). This raises questions on the validity of Eq. (5.7), where one assumed no initial phase gradient. As we see in Fig. 5.3a, there is an initial phase difference of $\approx 0.3\pi$ across the condensates. This non-zero phase gradient, $\partial_z\phi(z) \neq 0$, couples the local Josephson oscillations, as the second term in Eq. (5.5) is non-negligible in this case.

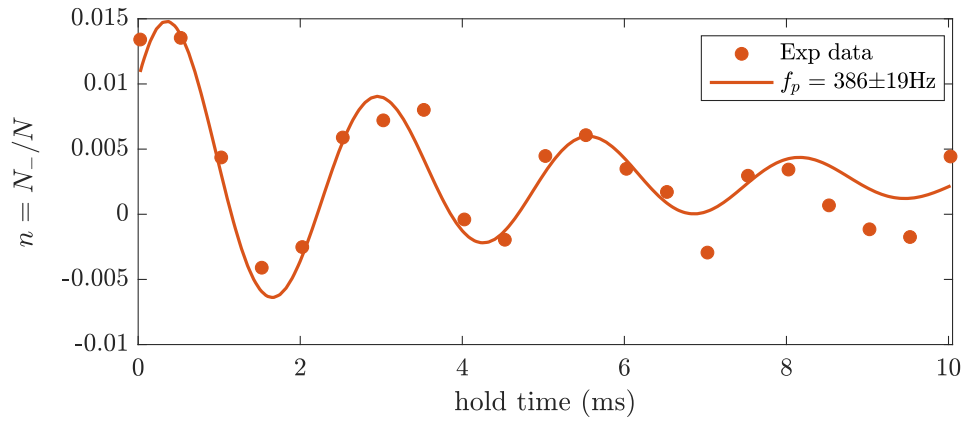


FIGURE 5.4: **Global Josephson oscillation with relative number readout** Complementary measurement as in Fig. 5.3 with exact experimental preparation routine in $\mathcal{A} = 0.5$ (MZI), except no final ramp-up to decoupled trap.

As being investigated in [72], by solving the Eq. (5.5) with fixed initial condition of zero spatial phase gradient, $\partial_z\phi(z, t)|_{t=0} = 0$, and zero imbalance, $\partial_t\phi(z, t)|_{t=0} = 0$, it was found that the solution of Eq. (5.5) yields slower Josephson oscillations in the condensate centre ($z = 0$) and faster oscillations on the edges. This means that the overall variation in plasma frequencies is suppressed compared to the formula in Eq. (5.6). This also aligns with our experimental observation in Fig. 5.3b. We should point out that the experimental results in [72] display a larger spatial variation of the plasma frequencies with respect to Eq. (5.6). The author in [72] attributes this to a density-dependent local tunnel coupling $J(z)$. As the measured plasma frequencies in our case are a few times faster than [72], namely the double well is more strongly coupled, thus we assume that the relative change of tunnel coupling strength along the condensates is not as significant.

In Fig. 5.3c, we plot the independently fitted damping rates at each spatial position. The Josephson oscillations on the edges of the condensates are more strongly damped compared to the ones around the centre. We refer to [24] for analytical insights, where the authors derived a set of linearized equations of

motion for the relative phase field $\phi(z)$ for the harmonically trapped systems

$$\frac{\partial}{\partial \tilde{z}} \left[(1 - \tilde{z}^2) \frac{\partial}{\partial \tilde{z}} \phi(z) \right] + \frac{2[\omega_n^2 - \omega_p^2(z)(1 - \tilde{z}^2)]}{\omega_z^2} \phi(z) = 0, \quad (5.9)$$

where the ω_n are the frequencies fulfilling $\phi(t) \sim \exp(i\omega_n t)$ and ω_p is defined in Eq. (5.6) and ω_z is the longitudinal trap frequency. The coupling between the local Josephson oscillations is explicitly expressed in Eq. (5.9). By solving this equation exactly (angular oblate spheroidal wave functions [79]) and expressing $\phi(z)$ and $\delta\rho_-$ with mode expansion in ω_n , one can explain the observed fast local damping (mode dephasing) and its eventual relaxation to a phase-locked state. This analytical solution (as well as the 3D GPE results Fig. 8 in [24]) confirms stronger damping on the edges of the harmonically trapped condensates, which fits with our experimental results.

Local Josephson oscillations and their relaxations in inhomogenous 1D systems are rather complex. It comprises various topics of 1D effective field models, such as coupling between relative and common degree of freedom, the integrity of 1D systems [80] and higher-order correlations [16, 81]. These are all very essential yet challenging questions, stretching beyond the scope of this thesis. The goal of this section is, first of all, to explore the capability of our imaging resolution to resolve longitudinal dynamics. For future studies on tackling the above questions, experimentally preparing initial states that are more easily comparable with numerical results would be a first step.

Chapter 6

Quantum fluctuation dynamics in bosonic Josephson junction

In this chapter, we will present the experimental observations on the dynamical evolution of quantum fluctuations in tunnel-coupled BECs after the BEC splitting process. We refer to these dynamics as squeezing oscillations. Furthermore, we demonstrate that the frequency of observed squeezing oscillation can be tuned. In Sec.6.2 we reason these dynamics with a semiclassical simulation BH model and also with 1D MCTDHB ($M = 2$) simulation. In Sec.6.3 we present an experimentally tractable approach to speed up the quantum fluctuation dynamics.

6.1 Squeezing oscillations

We will study in detail the dynamics of two spatially separated BECs in a stationary bosonic Josephson junction. By stationary, we mean that there are no obvious motional excitations between the two wavepackets. We first investigate the strongly coupled double well at $\mathcal{A} = 0.5$, where the interaction strength and tunnel coupling are comparable, $\Lambda = UN/2J \sim 10$. We symmetrically split a single BEC from a weakly dressed single well ($\mathcal{A} = 0.28$) into the double well at splitting speed $\kappa = 0.02 \text{ ms}^{-1}$. The symmetric splitting yields a prepared quantum state around the stable fixed point in the classical phase space. The stable fixed point represents the state where the mean values of the conjugate observables are both zero, $\langle N_- \rangle = 0$ and $\langle \Phi \rangle = 0$.

As described in Sec.4.2, BEC splitting results in non-equilibrium quantum states with overall quantum fluctuations different from the ground state in Eq.(4.10). As shown in Fig.4.4, the projection noise in each of the conjugate quadratures is larger than the expected ground state fluctuations from Eq.(4.10) (at zero temperature). By letting the system evolve for some time after the splitting process, we observe oscillatory dynamics in the quantum fluctuations in both relative number and relative phase quadrature [75]. We show in Fig. 6.1 the observed number and phase squeezing factors with total atom number $N = 4302(45)$ projected in the Φ quadrature and $N = 4154(35)$ projected in the N_- quadrature. We fit the oscillations in each quadrature with a simple sinusoidal function and obtain comparable squeezing oscillation frequencies of

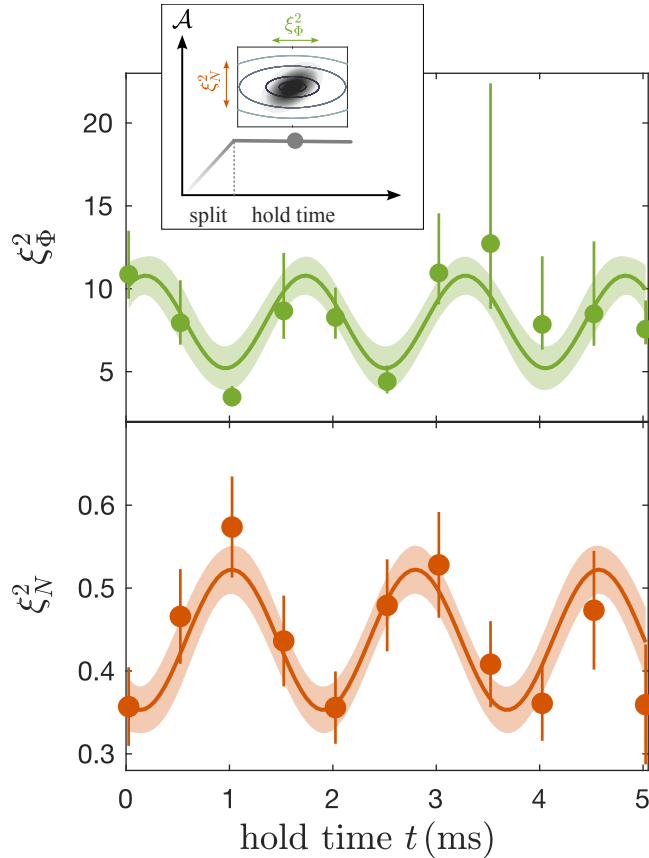


FIGURE 6.1: **Squeezing oscillations in conjugate observables.** **a.** Measured phase (green circle) and number (orange circle) squeezing factors as a function of hold time in strongly coupled double well ($\mathcal{A} = 0.5$) after a linear ramp from a single well with speed $\kappa = 0.02 \text{ ms}^{-1}$ (see inset) [75]. We observe squeezing oscillations in both quadratures with comparable frequencies and a relative phase shift of π between the oscillations. All solid lines are fitted with a sine function, and bands indicate 68% prediction confidence interval. Errorbars represent one s. e. m.

$f_\xi = 649(33) \text{ Hz}$ and $f_\xi = 567(29) \text{ Hz}$ with 68% prediction confidence interval¹. On top of this, the oscillations are π -phase shifted with respect to each other.

The measured squeezing oscillation frequency is found to originate from the plasma oscillation of each realisation of the quantum state. We illustrate quantum state evolution in Fig. 6.2. While the ground state squeezed states are expected to stay stationary, a state with different fluctuations than the ground state, the state evolves around the stable fixed point in the phase space, characterised as a rotation and deformation. But as our current readout does allow us to perform quantum state tomography, our projection is always readout in either N_- or Φ as depicted in Fig. 6.2b. In the next section, we will use simulations to provide more quantitative insights.

¹inbuilt function of `bootci()` with confidence interval $1-\alpha = 0.68$ in MATLAB and `jackknife()` give the same result.

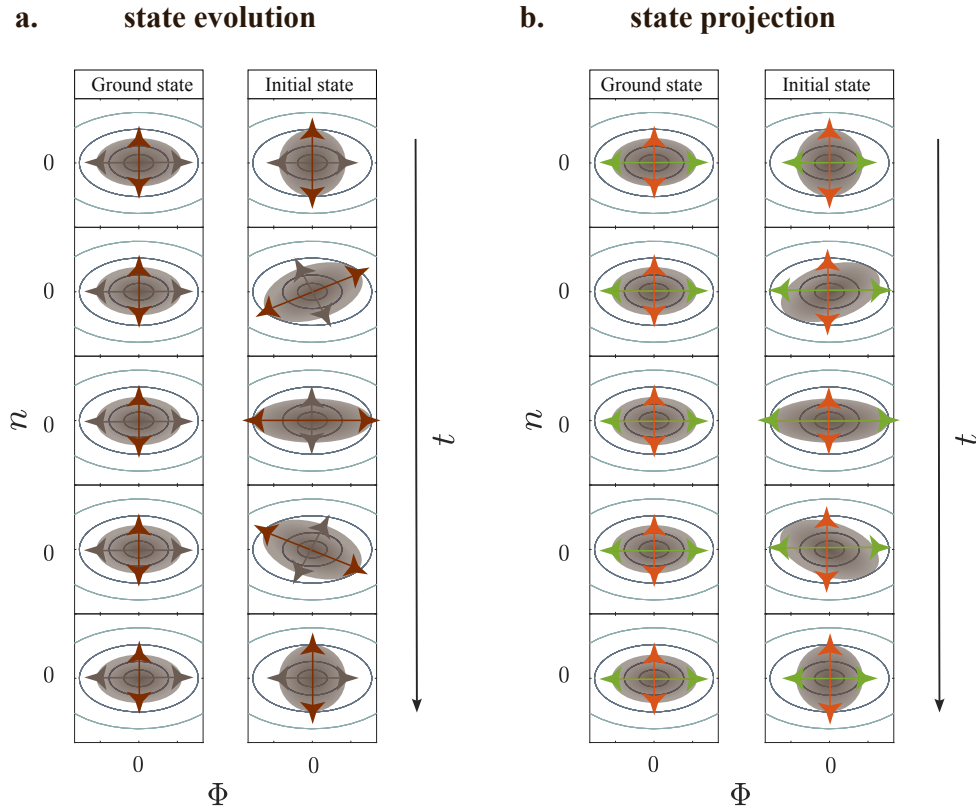


FIGURE 6.2: **Sketch on quantum state evolution in phase space** Ground state of the bosonic Josephson junction and an arbitrary initial state (non-ground state) evolve in the phase space of a bosonic Josephson junction in the Josephson regime ($\Lambda \sim 10$). Red and grey markers indicate the long and short axis of the quantum state fluctuations (variance). Orange and green markers represent the projected quantum fluctuations in the relative number (orange) and relative phase (green) quadratures.

6.2 Simulation on squeezing oscillations

In this section, we use two types of simulations to demonstrate how the observed squeezing oscillation is connected to the Josephson oscillations in the mean-values. The first approach is a semiclassical simulation based on two-mode BH model. It is easy to implement and provides good insight into the experimental findings. The second one is a many-body simulation, the MCTDHB method (see Sec. 2.1). MCTDHB gives comparable results to the semiclassical simulations in terms of squeezing oscillations. Additional results from the 1D MCTDHB simulation connected to optimisation of the spin-squeezed state (see Sec. 7.1) are also presented.

6.2.1 Semiclassical two-mode BH

To comprehend the observed squeezing oscillation in the tunnel-coupled double well $\mathcal{A} = 0.5$ (see Fig. 6.1), we set up a semiclassical simulation based on the two-mode BH model

$$H = \frac{2J}{\hbar} \left[\frac{UN}{4J} n^2 - \sqrt{1 - n^2} \cos \Phi \right], \quad (6.1)$$

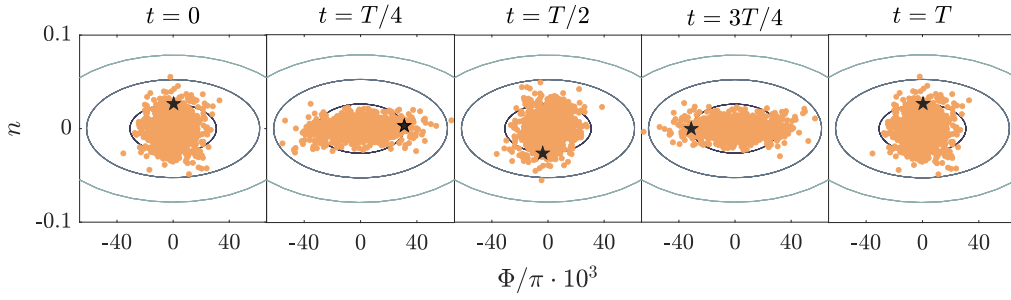


FIGURE 6.3: **Propagation of imprinted initial fluctuations in the two-mode BH model.** The start marker signifies the evolution of a single realisation, namely the mean values. A π rotation of a single realisation corresponds to a 2π rotation of the phase space distribution. Here T represents a period of Josephson oscillation.

with derived parameter values in the double well $\mathcal{A} = 0.5$: single particle tunnel coupling energy $J = 41$ Hz, interaction energy $U = 0.33$ Hz and total atom number $N = 4000$. Here J is estimated using Eq. (3.13) and N is the same as the experimentally measured atom number. In Fig. 6.3, we plot the equipotential lines in the obtained classical phase space. We estimate the expected ground state squeezing factors to be $\xi_{N,0}^2 \approx 0.24$ and $\xi_{\Phi,0}^2 \approx 4.2$ according to Eq. (4.10). We sample 1000 realisations from two normal distributions (one for each of the conjugate observables) with variances larger than the ground state fluctuations and propagate them with equations of motion deduced from Eq. (6.1) in the classical limit.

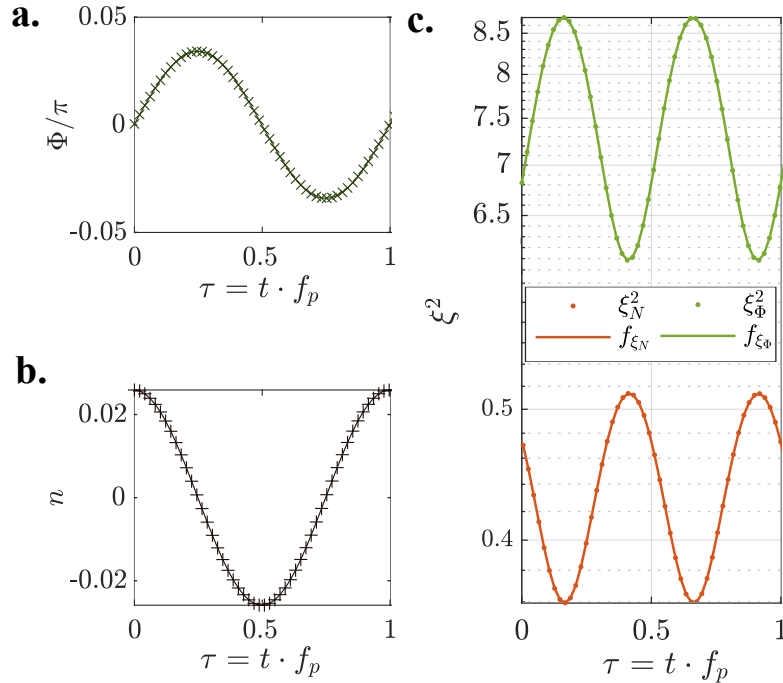


FIGURE 6.4: **Squeezing oscillation frequency** **a.** Evolution of a single realisation in Fig. 6.3 in the Φ . **b.** Evolution of a single realisation in N_- quadrature. **c.** Evolution of quantum fluctuations as squeezing factor ξ^2 in the conjugate quadratures and its fitted frequency corresponding to twice the plasma frequency f_p .

We show in Fig. 6.3 the state propagation with the imprinted initial distribution in a time span corresponding to a full period of Josephson oscillation $T = 1/f_p$. The star marker indicates a single realisation, as well as the mean values, $\langle N_- \rangle$ and $\langle \Phi \rangle$. As one can see, after a half period of the Josephson oscillation at $t = T/2$, the fluctuations of the quantum state (variance) already returned back to the original fluctuations at $t = 0$, namely,

$$\Delta N_-^2\left(t = \frac{T}{2}\right) = \Delta N_-^2(t = 0), \quad \Delta \Phi^2\left(t = \frac{T}{2}\right) = \Delta \Phi^2(t = 0). \quad (6.2)$$

We show in Fig. 6.4 the evolution of the mean values $\langle n \rangle$ and $\langle \Phi \rangle$ over time, and the evolution of the projection noises on each observable, denoted as squeezing factors. The evolution of $\langle n \rangle$ and $\langle \Phi \rangle$ are the Josephson oscillation at the plasma frequency f_p , which have been discussed in details in Chpt. 5. By fitting a sinusoidal function, we obtain that the squeezing factors oscillate at twice the plasma frequency, $f_\xi = 2f_p$. The oscillations of the projected fluctuations in the two quadratures are π -phase shifted with respect to each other. The initial fluctuations are chosen to best match the experimental results in Fig. 6.1.

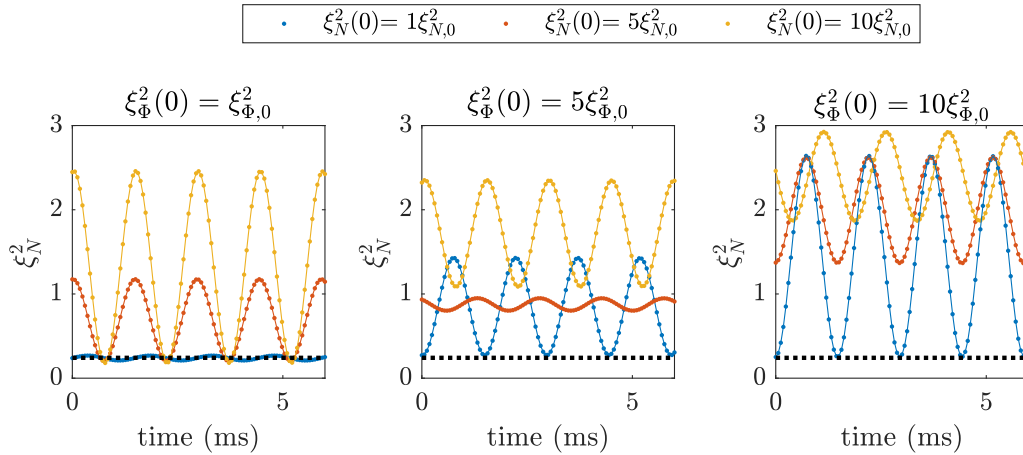


FIGURE 6.5: **Dependence on initial quantum fluctuations** Squeezing oscillation in the number quadrature in strongly coupled bosonic Josephson junction with $J = 41.0$ Hz with varying initial number squeezing factor $\xi_N^2(0)$ and fixed phase squeezing factor ξ_Φ^2 with increasing order from left to right panels, in units of the ground state squeezing $\xi_{\Phi,0}^2$. The black dotted lines indicate the ground state number squeezing factor $\xi_{N,0}^2$.

We conduct a systematic assessment with the semiclassical simulation to explore how initial fluctuations affect the resulting squeezing oscillations. We show the evolution of number squeezing factors in Fig. 6.5 as a result of different initial fluctuations. We denote the fluctuations with respect to the expected ground state squeezing factors $\xi_{N,0}^2$ and ξ_Φ^2 (Eq. (4.10)). We neglected the phase squeezed case, $\xi_\Phi^2 < 1$, in the simulation, as this is not so relevant for our experimental system.

The simulation results in Fig. 6.5 demonstrate that the minimal attainable number squeezing factors $\xi_{N,\min}^2$ during the squeezing oscillations depend on the orientation of initial phase space fluctuations and the overall fluctuations $\xi_N^2 \cdot \xi_\Phi^2$. More accurately, the minimal projection noises in the N_- or Φ quadrature correspond to the minimum of the two ratios, $\xi_N^2/\xi_{N,0}^2$ and $\xi_\Phi^2/\xi_{\Phi,0}^2$. This is a simple empirical value based on the landscape of the phase space. More generally, the best experimentally achievable number squeezing should be the minimal ratio between the initialised quantum state fluctuations and the ground state fluctuations along any axes in the phase space.

We want to remind the readers that this simulation is a simple toy model for mapping the dynamics in complex many-body systems. Many complexities are not included here, such as the relaxation of Josephson oscillations in Chpt. 5, the extended longitudinal degree of freedom and the interaction-induced phase diffusion etc. All these features need to be taken into account to experimentally observe the squeezing oscillations. Nevertheless, the simulation provides valuable insight into the oscillation and as we see in Sec. 6.2.3 means of tuning the squeezing oscillations.

6.2.2 MCTDHB simulation

For gaining a more realistic picture of the many-body dynamics of BEC in double wells with varying tunnel coupling strengths, we set up a 1D simulation with $M = 2$ orbitals in collaboration with Phila Rembold². To best compare with the experimental readout, the simulation also uses the single shot readout by projecting the wavefunction on either a spatial (relative number readout) or momentum (relative phase readout) basis. The trapping potentials used in the simulation are the calculated transversal trapping potentials from trap simulation (see Fig.3.7) and the realistic effective 1D interaction strength g_{1D} obtained by integrating over the longitudinal direction (more details can be found in van Frank's PhD thesis [52]).

By first relaxing into a single well to prepare the initial state and performing a similar splitting procedure as the experiment, the 1D MCTDHB simulation demonstrates squeezing oscillations in tunnel-coupled double well very similar to the experimental results, plotted as orange markers in Fig. 6.6. The squeezing factors in N_- and Φ quadratures oscillate at the same frequency and with a relative π -phase shift with respect to each other. This result is compatible with the semiclassical simulation in Sec. 6.2.1 and the experimental results in Fig. 6.1.

In addition, we plot in Fig. 6.6 the resulting squeezing oscillations with a two-step sequence (see Fig. 7.1). As we will discuss in Sec. 7.1, the two-step splitting aims to transfer the best number squeezing from the tunnel-coupled double well to a decoupled double well. The number squeezing oscillation in the tunnel-coupled trap (orange markers) is not altered much by the second linear ramp to the decoupled trap (blue markers). As we will show in Sec. 7.1, this does not quite agree with our experimental observations of two-step splitting, where we

²previously in Forschungszentrum Jülich, now at TU Wien

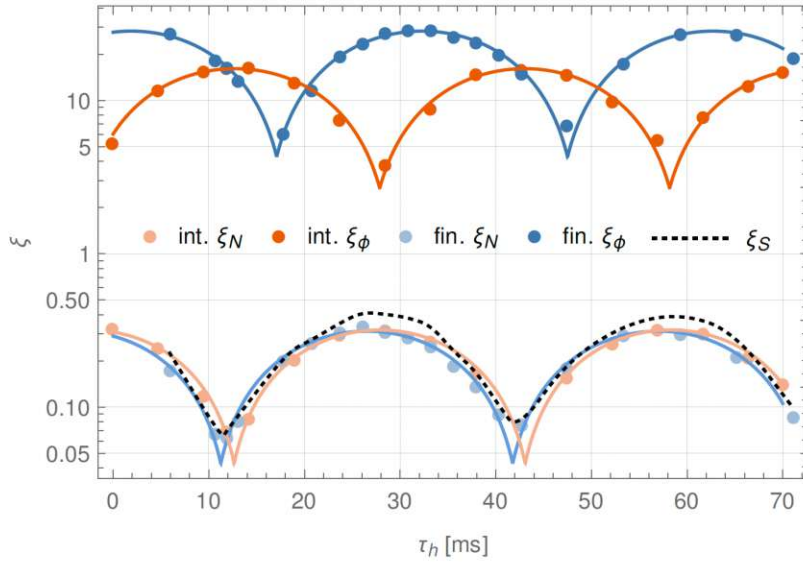


FIGURE 6.6: **Simulated squeezing oscillation and two-step with 1D MCTDHB.** The 1D simulation uses $N = 1500$ atoms and $M = 2$ orbitals. Squeezing oscillations as a function of hold time detected directly in the tunnel-coupled double well at $\mathcal{A} = 0.578$ (denoted as int. ξ , orange markers) and after two-step to the final decoupled trap (denoted as fin. ξ , blue markers). The dotted black line is the calculated spin squeezing factor. Adapted from Rembold's thesis [83].

observe an enhanced number of squeezing due to the nonlinearity in the second ramp. It is possible that since the obtained number squeezing in tunnel-coupled double well at $\mathcal{A} = 0.578$ is already so substantial, $\xi_{N,\min}^2 \sim 0.003$, such that the second linear ramp cannot contribute much. We want to remark on that the two-step sequence used to produce the simulation results in Fig. 6.6 is the optimised sequence using an open-loop optimisation [82]. However, as we will discuss later this optimised two-step sequence is not directly applicable to the experiment.

On the other hand, after the two-step, the phase squeezing oscillation is shifted by $\pi/2$ compared to results without a second ramp. This leads to a $\pi/2$ -shifted oscillation with respect to the number squeezing oscillation after two-step. There is no direct experimental verification on this phase shift of oscillations in the phase quadrature ξ_{ϕ}^2 . It, however, points towards that the fluctuations in the phase space might be distorted during the second ramp. If this is true, it means that we should not be looking for a maximal phase squeezing factor to optimise number squeezing after the two-step sequence in the experiment.

Initially, a comprehensive comparison between the MCTDHB simulation ($M = 2$ orbitals) and the experiment is intended as preparation for implementing optimal control algorithm generated ramps on the experiment to achieve optimal spin squeezed state using a two-step sequence. After comparing the experimental results to the 1D simulation, certain discrepancies have been noticed. First of all, the Josephson oscillation frequencies do not match, making an open loop

optimisation infeasible. This is because the Josephson oscillation frequency directly links to the squeezing oscillation frequency, which determines the optimal hold time in tunnel-coupled traps. Secondly, the observed decay in fringe contrast for less tunnel-coupled trap and relaxation of the Josephson oscillation, which is connected to multimode dynamics in the longitudinal degree of freedom (see Sec. 7.3), are not captured by 1D simulation at all.

Efforts have been taken by Phila Rembold to set up a 2D simulation with the help of Camille Lévêque³. With $M = 1$ orbital (mean-field), the 2D simulation nicely captures the relaxation-like dynamics of Josephson oscillations which we observe on the experiment (Chpt. 5). However, with $M = 2$ orbitals, the global phase coherence in the 2D simulation remains very high for a very long time after the BEC splitting, namely no phase diffusion at all is observed in the decoupled trap. After some investigation, we suspect the transversal dynamics to be artificially blocked to the symmetric modes. By using more orbitals and only a few atoms, the 2D simulation could eventually converge (see [83]) and the phase coherence decays sooner after the BEC splitting. But dynamics with few atoms are in a different regime from what one expects of a many-body system. Scaling up to many atoms and more orbitals presents a great challenge in computation power exceeding our current capacity.

6.2.3 Tuning squeezing oscillations

Based on experimental observation and insights from the simulations in previous subsections, we will now explore the possibility of tuning squeezing oscillations. With the established understanding that the observed squeezing oscillations are connected to the plasma oscillations and the squeezing oscillation frequency is twice the plasma frequency, we can simply tune the squeezing oscillation with the same approach as tuning the plasma frequencies. We studied in Ch. 5 exactly on how the plasma frequencies scale with the total atom number and with tunnel coupling strength (by adjusting the RF dressing amplitudes \mathcal{A}) based on Eq. (5.3).

Firstly, we will investigate whether we can observe squeezing oscillation in different double wells. As previously mentioned, with our precise controllability on the RF dressing amplitude \mathcal{A} , we can explore almost the full span of the Josephson regime, $1 < \Lambda < N^2$. Within this regime, the interplay between interaction U and tunnel coupling J demonstrates rich dynamics of the many-body quantum states. We see from Fig. 3.3b that the double well starts forming around $\mathcal{A} = 0.42$. However, in practice, for reading out the double wells, the lowest resolvable double well is around $\mathcal{A} = 0.48$ in the OCT trap. This limitation comes from that: (1) the fringe spacing becoming comparable with transversal cloud width after TOF for lower \mathcal{A} ($\lambda \sim \sigma_T$); (2) barrier height is too low, such that nonnegligible amount of atoms is under the barrier, making separation of the two clouds unreliable for relative number readout.

³Sorbonne University

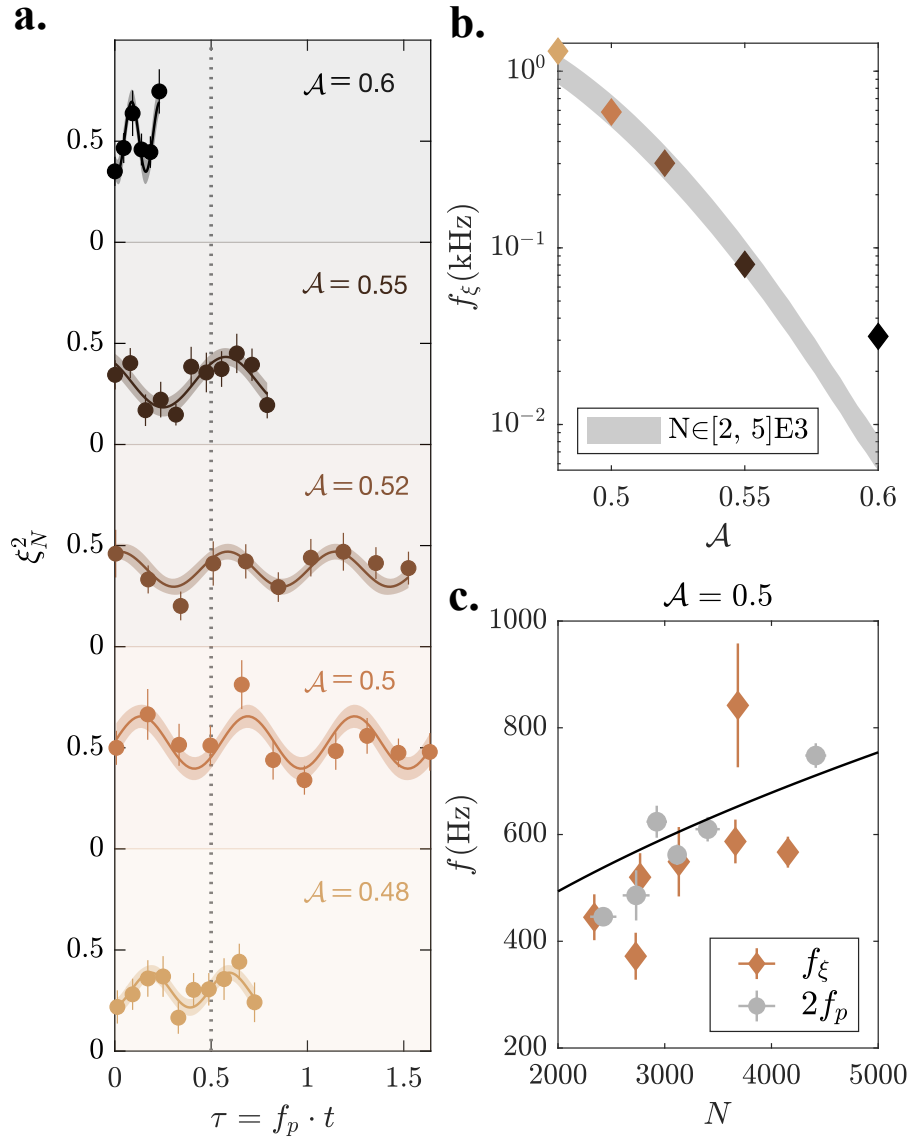


FIGURE 6.7: **Tuning squeezing oscillation frequency** **a.** Observed number squeezing factor ξ_N^2 evolution in coupled double wells with increasing RF dressing amplitude \mathcal{A} (bottom to top). The solid line is a fitted sine function with 68% simultaneous prediction bounds. **b.** The extracted squeezing frequency f_ξ (diamond) from **a.** together with the calculated prediction $2f_p$ (grey shade) with $N \in [2, 5] \cdot 10^3$ from Eq. (5.3). **c.** Dependence of f_ξ (diamond) on total atom number N in the strongly tunnel-coupled double well, $\mathcal{A} = 0.5$, and for comparison experimentally measured plasma frequencies $2f_p$ (circle) and solid line marks the inferred $2f_p$ from Eq. (5.3) with tunnel coupling strength $J = 40$ Hz.

In Fig. 6.7a, we show the observed squeezing oscillations in the number quadrature in double wells from $\mathcal{A} = 0.48$ ($\Lambda \sim 10$) to $\mathcal{A} = 0.6$ ($\Lambda \sim 5 \cdot 10^4$). The extrapolated frequencies f_ξ are plotted collectively in Fig. 6.7b. The frequencies span over an order of magnitude from 1 kHz to 30 Hz. As a comparison, twice the plasma frequency based on Eq. (5.3) with atom number $N \in [2, 5] \cdot 10^3$ are plotted as a grey band in the same figure. The overall quantitative agreement is excellent, apart from frequency measured in weakly coupled double well at

$\mathcal{A} = 0.6$. This discrepancy comes from the interaction broadened transversal profiles. The broadening leads to larger tunnel coupling than the inferred J from single-particle eigenenergies in Eq. (3.13).

Another way to tune the squeezing oscillations is with the total atom number. In Fig. 6.7c, the measured squeezing oscillation in double well $\mathcal{A} = 0.5$ are displayed as a function of total atom number. In addition, we plot measured the plasma frequencies (as in Fig. 5.1). The total atom number is tuned between $2 \cdot 10^3$ and $4.5 \cdot 10^3$ with the final frequency of the evaporative cooling. The frequency tunability with just the atom number is more limited, 400 Hz to 700 Hz. However, the agreement between the measured plasma frequencies and squeezing oscillation frequencies is very good. The outliers of f_ξ could come from either the scanning resolution of the hold time t or drift in the experiment. These measurements are based on changes in quantum fluctuations and, thus are highly sensitive.

6.3 Modulated tunnel coupling

So far, we have mainly explored how quantum fluctuations evolve in a stationary bosonic Josephson junction, where no relative motion between the two condensates is present. In this section, we explore the dynamics of quantum states in a bosonic Josephson junction with modulated tunnel coupling. The modulation comes from the induced motion of a splitting quench. Some of the emerging dynamics are unique to a modulated bosonic Josephson junction. Others still stem from the stationary bosonic Josephson junction.

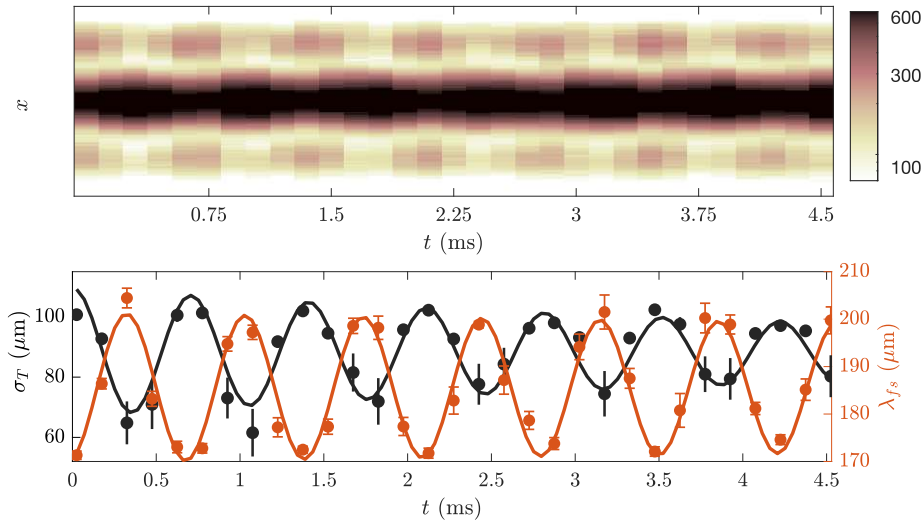


FIGURE 6.8: **Interference carpet after splitting quench.** Transversal sloshing in $\mathcal{A} = 0.5$ trap resulted from splitting quench with $\kappa = 0.085 \text{ ms}^{-1}$ from the single well. The transversal cloud width after TOF σ_T and fringe spacing λ_{fs} extracted by FT on the integrated interference pattern (top panel)

6.3.1 Induced interclouds motion

Let us investigate the induced in-trap motion of the BECs after a splitting quench. The quench is applied by splitting a BEC from a single trap to the strongly coupled double well at $\mathcal{A} = 0.5$ at a splitting speed $\kappa = 0.085 \text{ ms}^{-1}$. In Fig. 6.8 we display the resulting transversal interference pattern over hold time t in the double well. As we can see, both the fringe spacing λ_{fs} and the transversal width σ_T of the Gaussian envelope after TOF is oscillating at the transversal trap frequency, which is $f_x = 1.42(6) \text{ kHz}$ in $\mathcal{A} = 0.5$ trap.

We can infer the intercloud distance d from the fringe spacing, obtained by Fourier transforming (see Eq. (3.33)) and the fitted transversal cloud width σ_T after TOF, with the expression

$$d = \frac{2\pi\sigma_T^2}{\omega_x\lambda_{fs}t_F}, \quad (6.3)$$

where $t_F = 43.4 \text{ ms}$ is the TOF duration for the fluorescence imaging and measured transversal trap frequency ω_x (in Fig. 3.7). By assuming a stationary in-trap cloud width a_\perp and a ballistic expansion as described in Eq. (3.32) and a long TOF fulfilling $t_F^2 \gg \omega_\perp^{-2}$, the expression in Eq. (6.3) can be re-expressed as

$$d = \frac{ht_F}{m\lambda_{fs}}. \quad (6.4)$$

In Fig. 6.9 we compare the inferred in-trap intercloud distance with the expression in Eq. (6.4) (red markers) and Eq. (6.3) (grey markers). The former (red) estimates a peak-to-peak oscillation amplitude of $\approx 0.1 \mu\text{m}$ and the latter (grey) fitted an oscillation amplitude of ca. $0.6 \mu\text{m}$. This discrepancy is caused by the oscillation of cloud width σ_T after TOF (Fig. 6.8), which is out-of-phase with fringe spacing λ_{fs} . The oscillation of σ_T possibly originates from breathing induced by an abrupt change in the transversal trap frequency from the initial $\approx 2 \text{ kHz}$ in weakly dressed single well at $\mathcal{A} = 0.28$, see Fig. 3.7.

In the case of strong transversal breathing, Eq. (6.4) presents itself as a more accurate formula for inferring intercloud distances. On the other hand, Eq. (6.3) justifies the abrupt change in the overlap between the two wavepackets induced by transversal breathing, which effectively leads to a drastic change in tunnel coupling strength J as expressed in Eq. (2.12). In addition, a dispersion of the wavepackets, while they slosh around the trap minimum within each of the wells, might also contribute to a change in transversal width.

We repeat the same splitting quench as the previous section but now read out in the relative number quadrature, see Fig. 6.10. The readout is done with the following kick routine: raising RF amplitude from 0.5 to $\mathcal{A}_{\text{kick}} = 0.68$ in 0.175 ms and hold at $\mathcal{A}_{\text{kick}}$ for 0.15 ms before trap release. The resulting transversal profile after the TOF for relative number readout is shown in Fig. 6.10. One can still resolve the induced sloshing on the transversal profiles on the fitted Gaussian centres, $x_{L/R}^0$, of each cloud (lower panel). The fitted frequency of $x_{L/R}^0$ agrees very well with the inferred in-trap motion from the interference pattern of the same quench in Fig. 6.9. We are not sure of the origin of the "interference" on

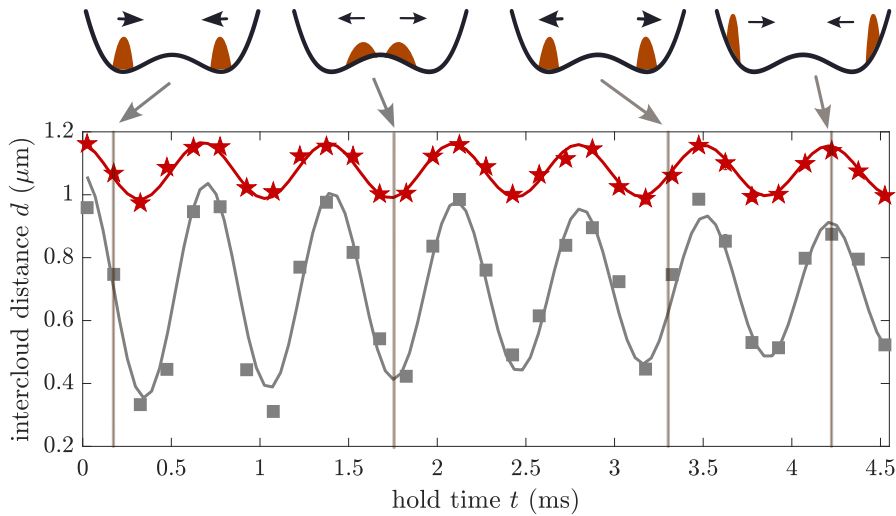


FIGURE 6.9: **Intercloud sloshing** The conjectured motion of the two condensates is illustrated (at the top). Inferred inter-condensate distance oscillates at transversal trap frequency. We use respectively Eq. (6.3) (gray squares) and Eq. (6.4) (red stars) to infer the distance d . We fit with a sinusoidal function with exponential damping and obtain an oscillation frequency $f = 1422(60)$ Hz.

top of each profile. The fringe spacing seems to coincide with what we expect from an interference pattern of a double well at $\mathcal{A}_{\text{kick}} = 0.68$. But how the interference pattern appears on the separated condensate profiles (mainly on the left condensate) is not so clear.

With the induced out-of-phase intercloud distance oscillations and the transversal breathing of each condensate, it is reasonable to deduce that the effective tunnel coupling J is modulated at the trap frequency. We will investigate in the next section how this modulated tunnel coupling influences the squeezing oscillations in both the number and phase quadrature.

6.3.2 Driven squeezing oscillations

By performing a splitting quench from a single well to a double well and letting the split BECs evolve for some time, we observe squeezing oscillations in the number quadrature at comparable frequencies as the transversal trap frequency, shown in Fig. 6.11. The time steps here are deliberately chosen to be able to resolve frequencies comparable to the transversal trap frequency f_x . A time span corresponding to $1/f_x$ is shaded in the figure for easy comparison. The double wells that we investigated in Fig. 6.11 represent a large range within the Josephson regime, from $\Lambda \approx 10$ to $\Lambda \approx 5 \cdot 10^4$, as shown in Fig. 4.4. It is therefore interesting to see how a modulated tunnel coupling influences the dynamics of quantum fluctuations in different double wells.

In previous work on optimal control of number squeezing in trapped BECs [84], one of the optimal approaches is by actively modulating tunnel coupling strength to enhance the squeezing oscillations. This approach is referred to

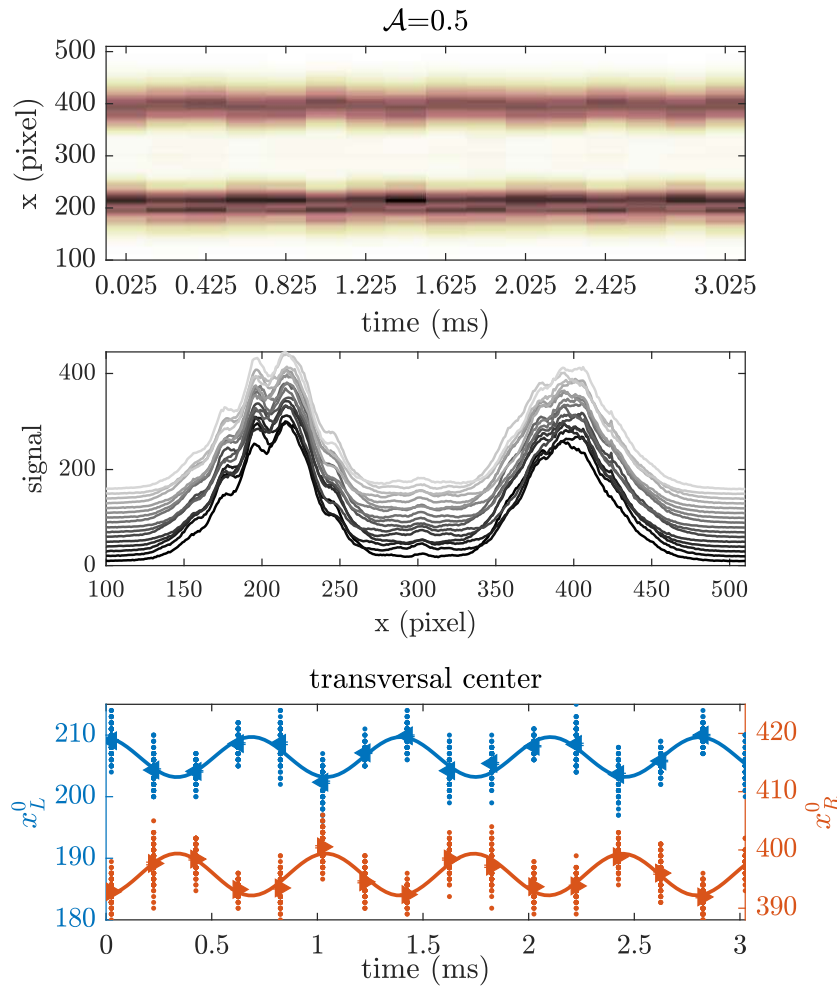


FIGURE 6.10: **Transversal sloshing after kicking** Upper panel: Integrated transversal density as a function of hold time after fast splitting to strongly coupled double well, $\mathcal{A} = 0.5$. Middle panel: stacked transversal profiles as line plots for better visualisation (darker to lighter with increasing time instances). Bottom panel: Fitted Gaussian centre of the left cloud x_L^0 and the right cloud x_R^0 of single shots (dot marker) and averaged values (triangle marker).

as parametric amplification. Most generally, the parametric resonances are at multiple integers of the natural frequency, which is plasma frequency in the case of tunnel-coupled BECs. Experimentally, this corresponds to applying a modulation on tunnel coupling at twice the plasma frequency, which is close to what we achieve in a splitting quench to $\mathcal{A} = 0.48$ trap (upper left panel in Fig. 6.11).

In the $\mathcal{A} = 0.48$ double well, the observed squeezing oscillation frequency after splitting quench is estimated to be $f_\xi = 1857(138)$ Hz, which is significantly higher than the transversal trap frequency measured to be $1390(60)$ Hz. Comparing to the squeezing oscillation in a stationary bosonic Josephson junction (no modulation on J) as shown in Fig. 6.7 with fitted frequency $f_\xi =$

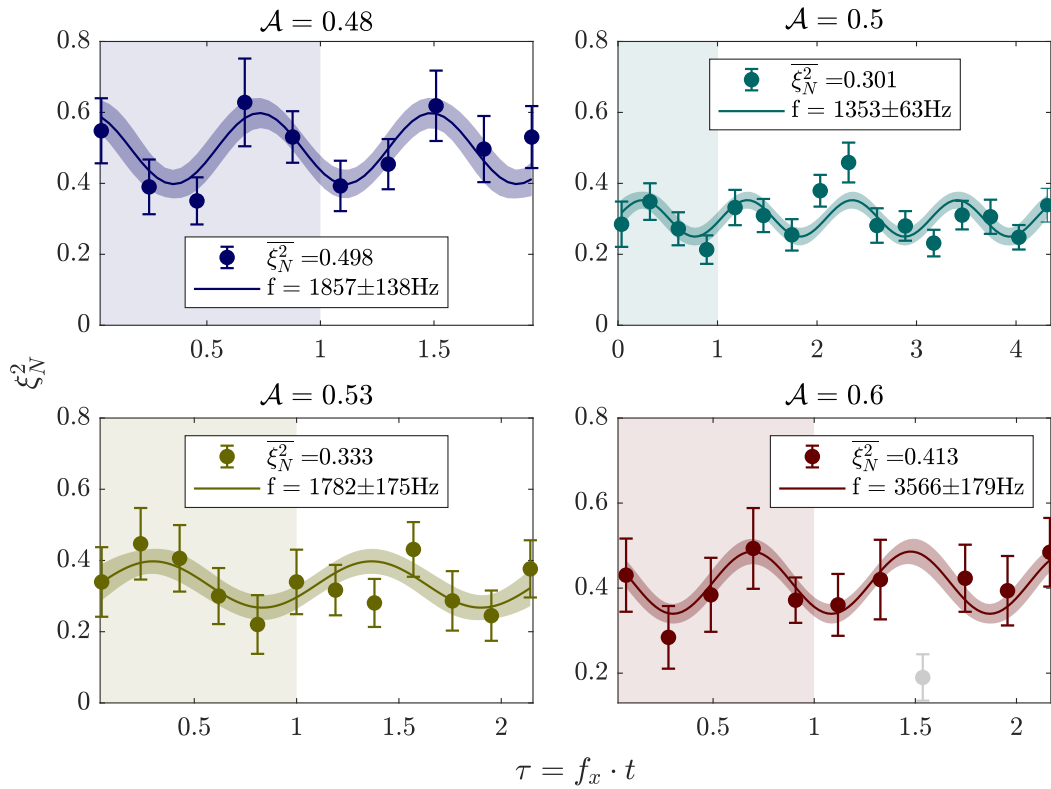


FIGURE 6.11: **Drive number squeezing oscillations in double wells.** By performing a splitting quench from a single well at split speed $\kappa = 0.08 \text{ ms}^{-1}$, we observe enforced squeezing oscillations at the order of transversal trap frequencies. The hold time τ is rescaled to the transversal trap frequency f_x of each double well. The grey marker represents the neglected data point (an outlier) for the fitting. Shaded regions remark $1/f_x$.

1300(142) Hz. In this exact double well, where f_ξ in the stationary bosonic Josephson junction coincides with the trap frequency f_x , we are realising a parametric amplification routine. In theory, the amplitude of the squeezing oscillation will be enhanced with modulated J . What we observed is rather a boost in oscillation frequency than an amplification in oscillation amplitude. It is not yet clear why this is the case, but could be attributed to the strong nonlinear Mathieu equation [85].

The upper right panel in Fig. 6.11 shows the squeezing oscillations observed in the modulated double well at $\mathcal{A} = 0.5$. This is the same experimental data that produces transversal profiles after kick in Fig. 6.10. We observe oscillation at a frequency $f_\xi = 1353(63) \text{ Hz}$, which is very comparable to the trap frequency $f_x = 1423(60) \text{ Hz}$. This means that the modulated tunnel coupling $J(t)$ enforces a squeezing oscillation at the trap frequency.

In less tunnel-coupled double wells, where $f_x \gg 2f_p$, we also observe driven squeezing oscillation at comparable frequencies with the trap frequency f_x . But as shown in the two lower panels in Fig. 6.11, the enforced squeezing oscillations damp much faster. As measurements on squeezing oscillations are very sensitive,

we are not ruling out the possibility that the experimental sets are simply less stable. But this could also suggest that the splitting quench works best in the strongly tunnel-coupled regime, where $f_x \sim f_p$.

The splitting quenches present themselves as an easily implementable experimental protocol for modulating tunnel coupling. The regime of the double wells can be further explored to best employ the trap frequencies as the modulation frequency. The amplitude of modulation can be controlled by tweaking parameters involved in the splitting quench. Recently there have also been some experimental works on Floquet engineering of tunnel-coupled 1D condensates [86] and theoretical studies on many-body parametric resonances in a driven SG model [87]. It could be interesting in the future to explore how active drive influences quantum fluctuations in our 1D multimode system. In the next chapters, we will present some observations revealing the multimode dynamics with the current experimental status.

Chapter 7

Optimised spin-squeezed states

Spin-squeezed states are highly attractive in quantum metrology for their enhanced sensitivity [3, 88]. Creating spin-squeezed states with ultracold atoms in the internal degree of freedom [4, 5, 89, 90] and external degree of freedom [3] has been explored in the last decades. Motivated by the observed squeezing oscillations, we will show in Sec. 7.1 an experimentally feasible approach to optimise the spin squeezing in the decoupled double well ($J = 0$). Furthermore, we will investigate how the enhanced spin squeezing prolongs the phase coherence in both the global degree of freedom in Sec. 7.2, as well as, protecting the decay of the spatial phase correlations in our extended multimode system in Sec. 7.3.

7.1 Optimisation with two-step

Single linear ramps from a single well to the decoupled double well have been used to create spin-squeezed states [3, 65]. Such procedures are also routinely performed on the experiment. However, the limitation with a single linear ramp-up is quite clear, as there is a direct trade-off between improving number squeezing (with a slower ramp-up) and better phase coherence (with a faster ramp-up). This is exactly what motivates us to develop alternative splitting methods to achieve optimal spin-squeezed states.

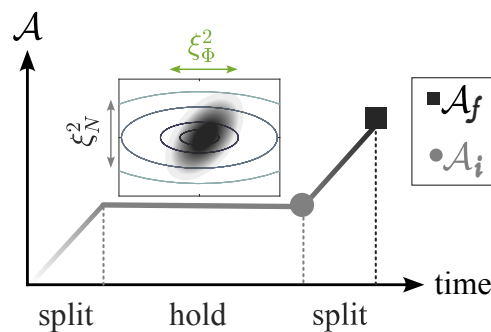


FIGURE 7.1: **Schematic of the two-step splitting procedure.** The first ramp is from a single well to a tunnel-coupled double well \mathcal{A}_i , allowing a certain hold time at \mathcal{A}_i and applying a second ramp to the decoupled trap \mathcal{A}_f . The inset shows out-of-equilibrium quantum state distribution in the classical phase space from the two-mode BH model in Eq. (6.1).

Conceptually, nonlinear ramps with the help of an optimal control algorithm can be generated for optimising spin squeezing. Numerous theoretical studies based on two-mode models for optimizing number squeezed states with the help of optimal control algorithm have been conducted [91, 92]. However, constructing a many-body simulation on the dynamics of 1D multimode systems has proven to be extremely challenging (in Sec. 6.2.2). Thus, we developed an experimentally tractable approach for optimization, on account of the observed squeezing oscillations, presented in Chpt. 6. We refer to this as a two-step approach.

A two-step sequence is illustrated in Fig. 7.1. The idea behind this approach is to optimise the hold time in the tunnel-coupled double well to achieve an improved spin-squeezed state before transferring the state to the decoupled trap with a second linear ramp. This is an efficient way to prohibit phase diffusion during the second ramp, thus generating better spin-squeezing in the decoupled trap.

7.1.1 Two-step with number readout

For the experimental implementation of the two-step approach, we add a second ramp after the initial splitting to tunnel-coupled double well after certain hold times. During the hold time, the dynamics in Fig. 6.1 and Fig. 6.7 are observed. The obtained number squeezing factors in the decoupled trap $\mathcal{A} = 0.65$ is shown in Fig. 7.2 as a function of hold time in the strongly coupled trap at $\mathcal{A} = 0.5$. Note that we keep the split speed of the first and the second ramp the same for a more straightforward comparison. But in general, the split speeds do not need to be the same.

After the second ramp-up, the measured number squeezing factor is further reduced compared to the coupled double-well in Fig. 6.1. The best-achieved number squeezing factor combined with the complementary measurement in

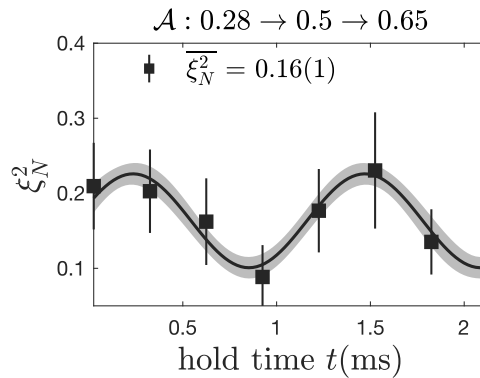


FIGURE 7.2: **Optimised number squeezing with two-step.** The oscillation stems from the hold time in the coupled double well at $\mathcal{A}_i = 0.5$. The measurement is performed after two-step splitting to $\mathcal{A}_f = 0.65$ with ramp speed $\kappa = 0.02 \text{ ms}^{-1}$.

phase quadrature¹, we obtain a squeezing factor of

$$\xi_S^2 = -9.2_{-3.0}^{+1.9} \text{ dB}, \quad (7.1)$$

which is a significant gain compared to a single ramp from a single well to the decoupled double well with the same duration. The single ramp results in a spin squeezing factor $\xi_S^2 \approx -2$ dB. The main contributing factor to the large distinction between the spin squeezing factors with two-step and single ramp is the phase coherence factor. The two-step yields $\langle \cos \Phi \rangle = 0.86(2)$ while single linear ramp gives $\langle \cos \Phi \rangle = 0.73(4)$.

In Sec. 6.3, we investigated how splitting quenches lead to modulation on the tunnel coupling so that squeezing oscillations are driven at the transversal trap frequency. Built on this, we implement a two-step quench to the decoupled trap and explore how the squeezing oscillations behave after adding a second quench. We show the experimental results of two-step quench in Fig. 7.3b with splitting speed $\kappa = 0.085 \text{ ms}^{-1}$ from the single well $\mathcal{A} = 0.28$. For completeness, we also plotted the driven squeezing oscillation in the tunnel-coupled trap in a. Here we rescale the time to the inferred plasma frequency $f_p = 326 \text{ Hz}$ in $\mathcal{A} = 0.5$ trap to demonstrate the boosted efficiency with the modulated tunnel coupling compared to the stationary case.

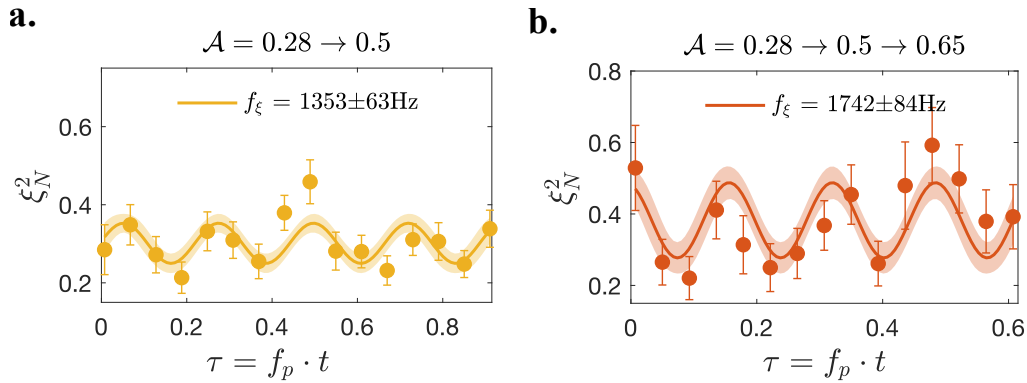


FIGURE 7.3: **Optimised number squeezing with two-step quench.** **a.** Measured ξ_N^2 (orange circle) in $\mathcal{A} = 0.5$ trap with enforced oscillation at the trap frequency $f_x \gg f_p$ after a splitting quench with $\kappa = 0.085 \text{ ms}^{-1}$ from a single well. **b.** Transferred squeezing oscillation after two-step quench to decoupled double well $\mathcal{A} = 0.65$. τ indicates hold time in strongly coupled $\mathcal{A} = 0.5$. Inferred plasma frequency $f_p = 326 \text{ Hz}$ is used here.

As one can see, the driven squeezing oscillation still persists after adding the second splitting quench. But the overall level of number squeezing in the final decoupled trap is slightly worse compared to after a single splitting quench in a. Nevertheless, due to the fast ramp-up, the phase coherence factor as a two-step

¹with an imaging pulse length of 1 ms, instead of typical 5 ms for number squeezing measurement. This is to enhance the fringe visibility, as there seems to be a vertical tilt between the fringes and the LS plane.

quench is very high, $\langle \cos \Phi \rangle \approx 0.95$. This ensures a best-attained spin squeezing factor of $\xi_S^2 \approx -6.5$ dB with the two-step quench.

7.1.2 Two-step with phase readout

Detecting squeezing oscillation with a two-step sequence is more challenging with relative phase readout. This is due to the phase diffusion during the splitting process, especially during the second ramp from coupled to decoupled trap. This washes out the phase squeezing oscillation observed in the strongly coupled trap in Fig. 6.1. As discussed earlier, speeding up the ramp is an effective way to prevent phase diffusion during the splitting. We also learned in Sec. 6.3 that the quench introduces transversal motion between the two condensates. Thus, we investigate in this section how a two-step quench influences the phase quadrature.

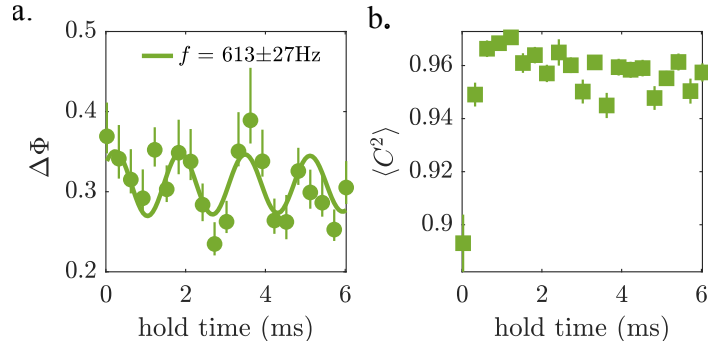


FIGURE 7.4: **Phase squeezing oscillation with two-step quench** **a.** Circular standard deviation $\Delta\Phi$ evolution as a function of hold time in strongly coupled double well $\mathcal{A} = 0.5$. The fitted sinusoidal function infers an oscillation frequency of 613(27) Hz. **b.** The spatial phase coherence factor $\langle C^2 \rangle$.

By performing a two-step quench: splitting $\mathcal{A} = 0.28$ to $\mathcal{A} = 0.5$ at speed $\kappa = 0.1067 \text{ ms}^{-1}$, allowing a variable hold time there, and splitting to $\mathcal{A} = 0.65$ at $\kappa = 0.075 \text{ ms}^{-1}$, we observe a dynamics in the global phase fluctuations, $\Delta\Phi$, shown in Fig. 7.4b. The extracted oscillation frequency by fitting a sinusoidal function on the global relative phase fluctuation is $f = 613(27) \text{ Hz}$. This frequency is comparable to the observed phase squeezing oscillation in $\mathcal{A} = 0.5$ trap after a slow splitting, shown in Fig. 6.1. For reference, the average phase squeezing factors are $\xi_\Phi^2 = N \cdot \Delta\Phi^2 \approx 20$ in Fig. 7.4, which is larger than the measured $\xi_\Phi^2 \approx 8$ in the $\mathcal{A} = 0.5$ trap without the second ramp-up to the decoupled double well (see Fig. 6.1).

With a two-step quench, the frequency of the observed squeezing oscillation in the phase quadrature is a bit surprising. From the obtained two-step quench measurements in the number quadrature (see Fig. 7.3), we intuitively expect the squeezing oscillation to be driven at the transversal trap frequency in the phase quadrature as well. But first of all, Fig. 7.4 is a validation that the squeezing oscillations in the stationary BJJ are still preserved despite a modulated tunnel coupling. Now let us naively express the motion of the equation for squeezing

factors as

$$\frac{\partial^2}{\partial t^2}\xi + \omega_0\xi = A \cos(\omega_x t), \quad (7.2)$$

where $\omega_0 = 2\omega_p = 4\pi f_p$ is the squeezing oscillation frequency in a stationary Josephson junction. The equation has a solution of type

$$\xi(t) = \frac{A}{\omega_0^2 - \omega_x^2} \cos(\omega_x t). \quad (7.3)$$

And since $\xi(t) = B \cos(\omega_0 t)$ is a solution to the undriven pendulum equation ($A = 0$ in Eq. (7.2)), the two solutions can be superimposed and lead to beating between stationary squeezing oscillation frequency ω_0 and trap frequency ω_x , such that the resulting squeezing oscillations

$$\xi(t) \propto \tilde{A} \cos(\omega_x t) + B \cos(\omega_0 t). \quad (7.4)$$

The interplay between the amplitude \tilde{A} and B can lead to very different patterns. For instance, the oscillation in Fig. 7.3 **a** could possibly originate from a superimposed solution between trap frequency and squeezing oscillation frequency in the stationary trap.

The resulting dynamics of an interplay between these two dynamics depend on the regime of the BJJ and the strength of the transversal excitations. In another experimental set, we perform a two-step quench in the MZI trap configuration, shown in Fig. 7.5. With finer time steps, we resolve an oscillation of $\Delta\Phi$ at $f_\xi = 849(36)$ Hz, which is similar to the trap frequency $f_x \approx 966(11)$ Hz. The dynamics match with what we expect with a two-step quench. The surprising finding is the significant magnitude of phase fluctuation oscillation.

The standard circular deviation $\Delta\Phi$ increases to 2 from 0.5 within ~ 0.6 ms. $\Delta\Phi \approx 2$ corresponds to a nearly completely random phase distribution (within finite statistics). This time scale is much shorter than the typical time scales of phase diffusion, as shown in Fig. 7.7. The exact governing physics behind this rapid growth in phase distribution is yet unknown. There might be a connection to higher-mode excitations. We show in Fig. 7.6 the dynamical evolution of the two-point correlation function $\langle \cos[\phi(z) - \phi(z')] \rangle$. Stronger correlations between two symmetric points z and $-z$ are observed, which resembles the observation of a generalized Gibbs ensemble [80]. The difference is that our system is evolving in a strongly tunnel-coupled double well, in contrast to the decoupled trap where the previous experimental findings are made.

7.2 Suppressed phase diffusion

It has long been known that split BECs have initially very highly correlated relative phases $\Delta\Phi_0 \ll 1$, but inter-atomic interactions randomise the relative phase over time. This phenomenon is known as phase diffusion. Studies have been conducted to characterize the phase diffusion rate [93, 94]. It has been derived that the distribution of the relative phase fulfils the following relation

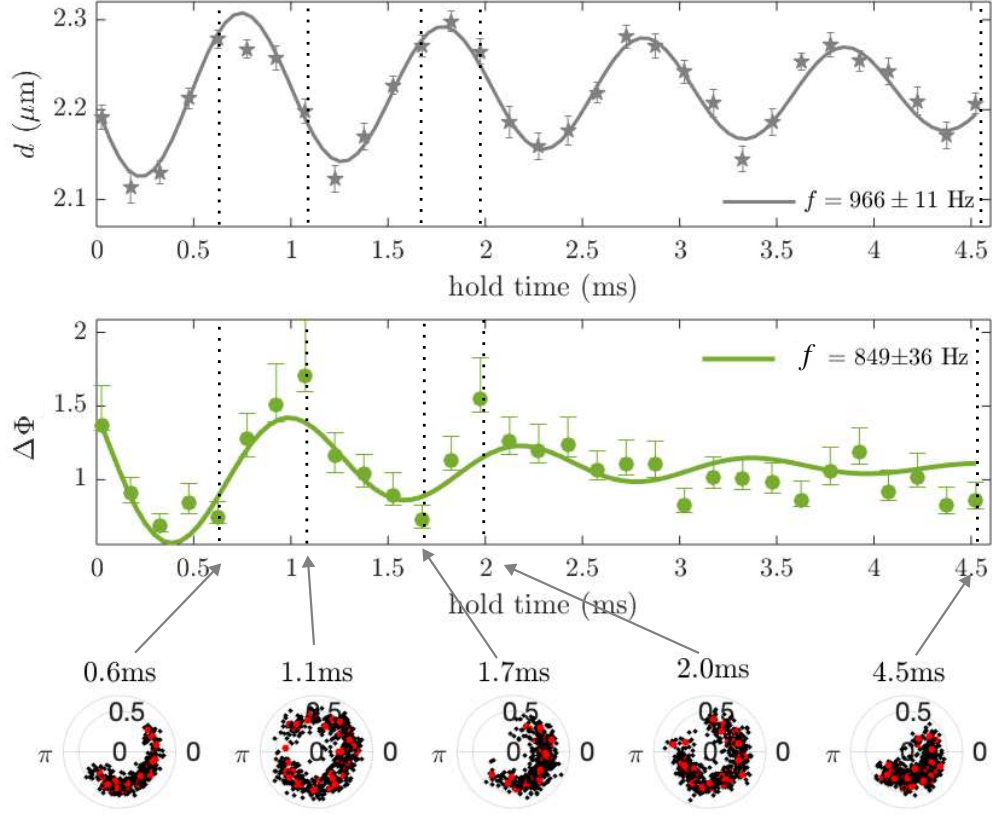


FIGURE 7.5: **Drive global phase distribution with two-step quench.** Performing two-step quench ($\mathcal{A} : 0 \rightarrow 0.552 \rightarrow 0.7$) with speed $\kappa \approx 0.1 \text{ ms}^{-1}$ in the MZI trap configuration (with $\beta = 20^\circ$) with hold time in the coupled double well and switch off right after two-step splitting. Here d is the inferred inter-condensate distance from the fringe spacing (grey star) and $\Delta\Phi$ is the extracted standard deviation of the global phase distribution inferred from the Fourier transform with the fixed centre of the Gaussian envelope. The polar plots are the distribution of ensemble measurements of the local phases (black) over the central region of $\pm 20 \mu\text{m}$ and the global phases as its circular mean (red) at various hold times marked as vertical dotted lines.

in decoupled double wells,

$$\Delta\Phi(t) = \sqrt{\Delta\Phi_0^2 + R^2 t^2}, \quad (7.5)$$

where R is the phase diffusion rate, expressed as

$$R = \frac{\xi_N \sqrt{N}}{\hbar} \left. \frac{\partial \mu}{\partial N} \right|_{N=N/2} = \frac{\xi_N}{\hbar} \frac{g_{1D} \rho(0)}{\sqrt{N}}, \quad (7.6)$$

for symmetric splitting ($N_L = N_R = N/2$), where we used the chemical potential of equilibrium states

$$\mu = g_{1D} \rho(0). \quad (7.7)$$

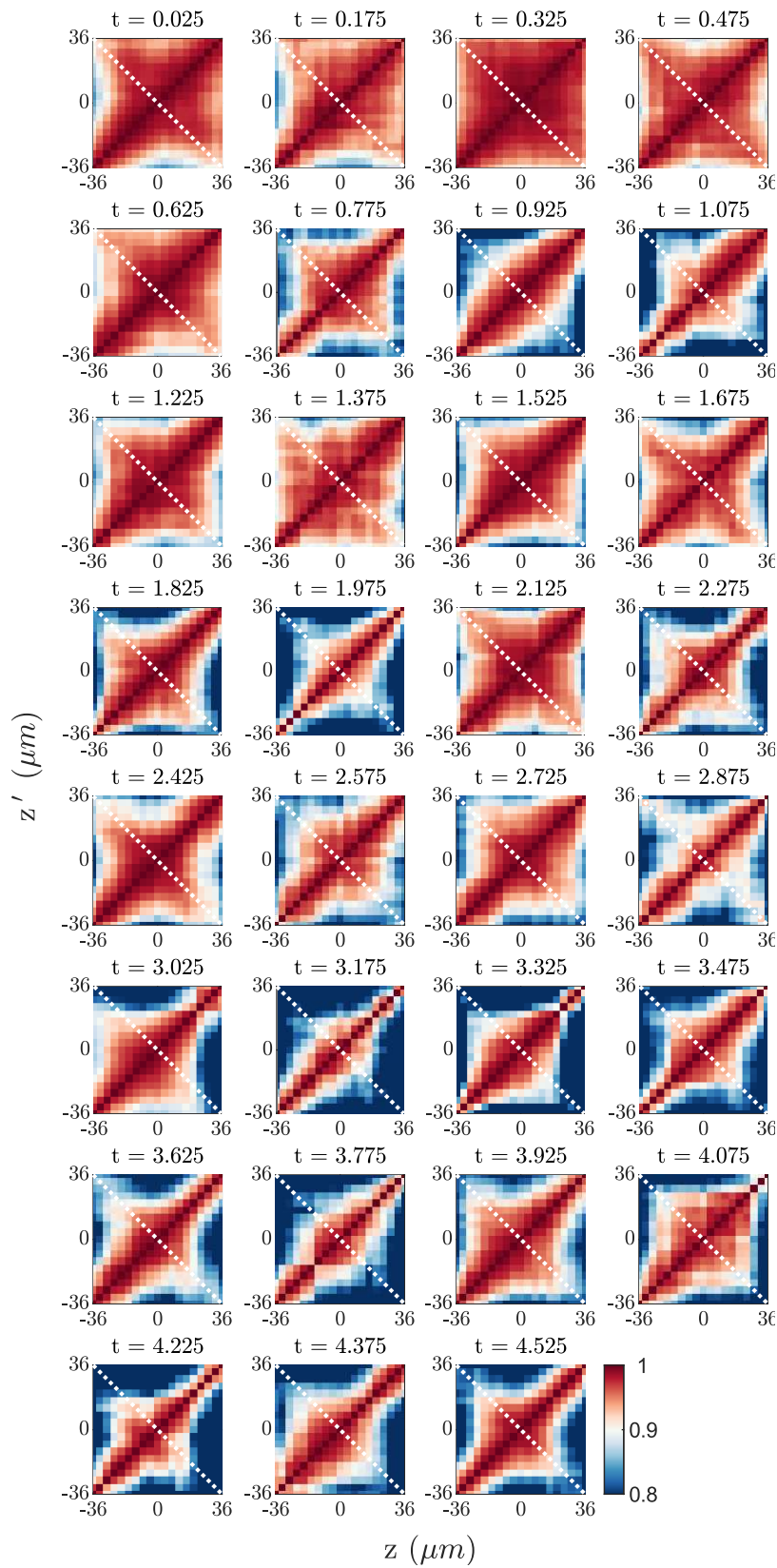


FIGURE 7.6: **Two-point phase correlation function (PCF)** Evolution of PCF as a function of hold time t (ms) in the strongly coupled double well with the two-step quench (MZI trap). Same experimental set as Fig. 7.5.

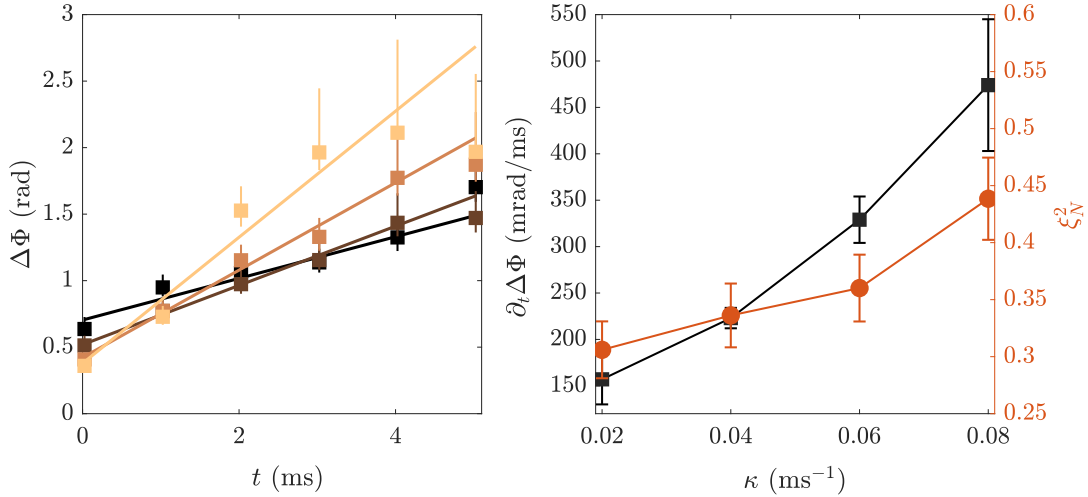


FIGURE 7.7: **Phase diffusion vs number squeezing** Left panel: Evolution of circular standard deviation of the relative phase, $\Delta\Phi$, in weakly coupled $\mathcal{A} = 0.6$ trap with varying splitting speed, κ , from the initial $\mathcal{A} = 0.28$ trap. Right panel: Number squeezing factor ξ_N^2 as a result of splitting speeds κ . 400 shots per data point are taken. The extracted phase diffusion rates $\partial_t\Delta\Phi$ from left panel are also displayed as comparison.

The expression in Eq. (7.6) is a direct indicator that number-squeezed states suppress phase diffusion and thus prolong the phase coherence time. Previous experiments have shown indirect evidence [95] and later an earlier project on this setup demonstrated directly the measured number squeezing factor to the phase diffusion rate [53]. Following up on these observations, we intend to show how different levels of number squeezing influence the phase diffusion rates in an effectively decoupled trap in Fig. 7.7. By effectively decoupled, we mean that the phase diffusion time is much shorter than Josephson oscillation. We prepare the different levels of number squeezing by controlling the splitting speed κ of a single linear ramp from the single well to the double well $\mathcal{A} = 0.6$. In the left panel in Fig. 7.7, we let the system evolve in the decoupled trap for up to 5 ms. We can infer the rate $R = \partial_t\Delta\Phi$ by linearly fitting on the time evolution of $\Delta\Phi$.

For weakly coupled double well $\mathcal{A} = 0.6$, the experimentally measured trap frequencies are $[\omega_x, \omega_y, \omega_z] = 2\pi \cdot [2.59, 2.65, 0.015]$ kHz. With $N = 3000$ atoms, we can calculate the effective 1D coupling strength along the longitudinal direction from Eq. (2.46) to be $g_{1D}/h = 28 \text{ Hz} \cdot \mu\text{m}$. With peak density of the original single condensate, $\rho(0) \approx 50 \mu\text{m}^{-1}$, we obtain $\mu/h = g_{1D}\rho(0)/h \approx 1.5 \text{ kHz}$. By plugging this into Eq. (7.5) and with the estimated R , we can in principle infer the number squeezing factor. Conversely, we can infer from the measured number squeezing factors the expected phase diffusion rates. We plot in the right panel in Fig. 7.7 the measured phase diffusion rates and the measured number squeezing factors.

With number squeezing factor $\xi_N^2 = 0.3$, we expect a phase diffusion rate at $R \approx 100 \text{ mrad/ms}$. This value matches very well with the observed diffusion rate as shown in the right panel in Fig. 7.7 with split speed $\kappa = 0.02 \text{ ms}^{-1}$. However, at faster splitting speeds, the measured phase diffusion rate is much

higher than what we expect from the measured number squeezing factors. This could originate from a non-zero energy difference in terms of tilted double well, $\Delta E \neq 0$, or a nonzero imbalance $n \neq 0$, such that the estimation of the chemical potential in Eq. (7.7) is not valid. In addition, the splitting speed is typically very abrupt in the time scale of the longitudinal dynamics, this means that the effective chemical potential right after the splitting is also different from the equilibrium one.

7.3 Protected spatial phase correlations

As introduced in Sec. 2.3.2.2, in 1D weakly interacting Bose gases, the phase correlation is preserved over finite lengths and lower energy excitations are populated after the Bose-Einstein statistics in the thermal equilibrium. The dynamics of out-of-equilibrium states have been previously investigated [16, 21, 80]. The two-point phase correlations are decoupled from the global phase dynamics and reveal interesting quantum correlations of the 1D system.

In this section, we will investigate how the spatial phase coherence between decoupled BECs evolves as a result of different levels of number squeezing. First, we look into the short-time dynamics, when the system relaxes into semi-stable states, known as prethermalisation [96]. We compare the relaxation dynamics for states with different levels of number squeezing and attribute this to the local dephasing. Then we investigate how improved spin squeezing protects the spatial phase coherence over longer times.

7.3.1 Evolution in decoupled double well

First, we will clarify that phase diffusion exclusively refers to the randomization of the global phase, $k = 0$ mode. For $k \neq 0$ modes, we refer to the randomization of the relative phase as dephasing. Here we assume quasicondensates confined in a box potential with length L , thus having homogeneous atomic density ρ_{1d} . An important distinction between these two is that phase diffusion ($k = 0$) leads to decay of the phase coherence factor [94, 97, 98]

$$\langle \cos \Phi(t) \rangle \propto \exp(-t^2/\tau_0^2), \quad \tau_0 = \hbar/g_{1D}\sqrt{L/\rho_{1d}}. \quad (7.8)$$

While the dephasing of all $k \neq 0$ modes leads to decay of the spatial phase coherence [99]

$$\langle C^2(t) \rangle \propto \exp(-t/\tau), \quad \tau = \frac{8K^2}{c\rho_{1d}\pi^2} \quad (7.9)$$

where the Luttinger parameter K is defined as

$$K = \frac{\hbar\pi}{2} \sqrt{\frac{\rho_{1d}}{mg_{1D}}}, \quad (7.10)$$

and the integrated squared contrast is

$$\langle C^2 \rangle = \sum_{z, z'} C(z, z') = \sum_{z, z'} \langle \cos \theta(z, z') \rangle. \quad (7.11)$$

For time evolution over longer time scales, as described in Sec.2.3.2.2, the Tomonaga-Luttinger liquid Hamiltonian in Eq. (2.71) is a good description of the relative degree of freedom dynamics of 1D quasicondensates in a decoupled double well. The Hamiltonian of quasicondensates with homogeneous atomic density is expressed in the Bogoliubov basis,

$$\hat{H}_- = \sum_k \frac{\hbar^2 k^2}{4m} \rho_{1d} \hat{\phi}_k^\dagger \hat{\phi}_k + \frac{g_{1D}}{4} \hat{\rho}_{-,k}^\dagger \hat{\rho}_{-,k}. \quad (7.12)$$

The time evolution of the relative phase and relative density field in the mode expansion is given by

$$\begin{aligned} \hat{\phi}_j(t) &= \hat{\phi}_j(0) \cos(\omega_j t) - \frac{\sqrt{m g_{1D}}}{\hbar k_j} \hat{\rho}_{-,j}(0) \sin(\omega_j t), \\ \hat{\rho}_{-,j}(t) &= \hat{\rho}_{-,j}(0) \cos(\omega_j t) + \frac{\hbar k_j}{\sqrt{m g_{1D}}} \hat{\phi}_j(0) \sin(\omega_j t) \end{aligned} \quad (7.13)$$

where $t = 0$ is the timing of adiabaticity breaking. The resulting evolution of the variance of local observables are

$$\begin{aligned} \langle \hat{\phi}_j^2(t) \rangle &= \langle \hat{\phi}_j^2(0) \rangle \cos^2(\omega_j t) + \frac{m g_{1D}}{\hbar^2 k_j^2} \langle \hat{\rho}_{-,j}^2(0) \rangle \sin^2(\omega_j t), \\ \langle \hat{\rho}_{-,j}^2(t) \rangle &= \langle \hat{\rho}_{-,j}^2(0) \rangle \cos^2(\omega_j t) + \frac{\hbar^2 k_j^2}{m g_{1D}} \langle \hat{\phi}_j^2(0) \rangle \sin^2(\omega_j t), \end{aligned} \quad (7.14)$$

where the cross terms disappear due to commutation relation $[\hat{\phi}_{j'}^\dagger, \hat{\rho}_{-,j}] = -2i\delta_{j,j'}$. From here, we can see that over time the density fluctuations convert into phase fluctuations and vice versa. A period of conversion for each k -mode scales inversely with mode frequency $1/\omega_k$. For the $k = 1$ mode of the harmonic trap, in Eq.(2.65), this corresponds to a period of ~ 50 ms. Thus at shorter times, the evolution of the fluctuations appears as dephasing.

The initial fluctuation of phase $\langle \hat{\phi}_j^2(0) \rangle$ and density $\langle \hat{\rho}_{-,j}^2(0) \rangle$ depend on the exact preparation procedure. At thermal equilibrium, the fluctuations fulfil Eq. (2.73). With splitting quenches, where no number squeezing is expected, $\Delta N_-^2 = N$, the local density fluctuations are also binomially distributed $\Delta \rho_-^2 = \rho_0$, where $\rho_0 = \rho(0)$ is the peak atomic density of the original unsplit condensate. Right after the splitting quench, the phases of the two split condensates are almost identical copies of each other. Presuming minimum uncertainty of relative phase fluctuations obeying the Heisenberg uncertainty principle, we obtain

$$\langle \hat{\rho}_{-,j}^2(0) \rangle = \rho, \quad \langle \hat{\phi}_j^2(0) \rangle = \frac{1}{\rho}. \quad (7.15)$$

This leads to non-equilibrium states far from the thermal equilibrium. In other situations, where the prepared state is out-of-equilibrium but not resulting from a quench, the initial fluctuations are difficult to predict analytically. In the next subsections, we stick to the experimental observations of the short-term and long-term dynamics of various non-equilibrium states in the decoupled trap and only provide some heuristic theoretical explanations.

Furthermore, we would like the readers to keep in mind that, in the low-energy description, the modes are independent of each other, hence no true relaxation and thermalisation is expected in integrable 1D systems. But in reality, there are other mechanisms [100–102] not considered in the Luttinger theory that could lead to the thermalisation of 1D systems. Thus this section just aims to provide some analytical insights that help us understand the experimental observations in the remainder of this section.

7.3.2 Short term dynamics: prethermalisation

Within a short timescale, split BECs relax to prethermal states [21, 96, 103, 104], which are non-thermal steady states that exhibit some thermal-like features. In previous works on prethermal states [21, 105], it has been found that the effective temperature T^- between two condensates are identified as the energies stored in each momentum mode. And within each mode, the energy is equally distributed between relative phase fluctuations $\Delta\phi^2 = \langle\phi^2\rangle - \langle\phi\rangle^2$ and the relative atomic density fluctuations, $\Delta\rho_-^2 = \langle\rho_-^2\rangle - \langle\rho_-\rangle^2$, as expressed in Eq. (2.73) for Gaussian states². Thus we express the effective temperature as

$$k_B T^- = \frac{g_{1D} \Delta\rho_-^2}{4}. \quad (7.16)$$

In the presence of number squeezing, the relative density fluctuations can be substituted by assuming equal number squeezing in all modes and using a single (global) number squeezing factor $\Delta\rho_-^2 = \xi_N^2 \rho_{1d}$. Thus Eq. (7.16) can be rewritten as

$$k_B T^- = \frac{g_{1D} \xi_N^2 \rho_{1d}}{4}. \quad (7.17)$$

where we remind the reader that ρ_{1d} is the atomic density in the original single condensate $\rho_{1d} = \rho_L + \rho_R$. With the typical experimental atomic densities, we estimate the effective temperature to be $T_B^- \approx 20$ nK resulting from a splitting quench ($\xi_N^2 = 1$). This temperature is lower than the typical thermal temperatures of our condensates 30 – 100 nK.

In Fig. 7.8, we investigate the two-point phase correlation (PCF) decay up to 4 ms after the BEC splitting. The PCF between two spatial points z and z' along the condensates is defined as

$$\langle \cos(\phi(z) - \phi(z')) \rangle = \langle \cos \theta(z, z') \rangle. \quad (7.18)$$

²fully characterized by up to second order correlation functions

In Fig. 7.8a, we display the two-point phase correlation correlation $C(z, z')$ at $t = 0$ ms and $t = 4$ ms after a linear ramp from the single well to $\mathcal{A} = 0.6$. The upper panels represent the number-squeezed state with $\xi_N^2 = 0.31(3)$ (orange colour) and the lower panels represent the number-squeezed state with $\xi_N^2 = 0.44(4)$ (green colour). By averaging over two-point PCFs with $\bar{z} = z - z'$ in Fig. 7.8a, we plot the averaged $\langle \cos \theta(\bar{z}) \rangle$ in Fig. 7.8b. We see that despite an initially high PCF (green square), the phase correlation decays much faster to lower values compared to the PCF decay of enhanced number-squeezed states (orange square). This decay is due to light-cone propagation of thermal correlations from shorter distances \bar{z} outwards at the phonon speed $l = 2ct$. Outside the transition length $\bar{z} = l$, the relative phase is locked [29]. In the homogeneous density limit, we expect the time derivative of the two-point phase variance to obey [47, 103, 106]

$$\partial_t \langle \Delta \theta^2(z, z') \rangle = \frac{2c}{l_\phi} \cdot \Theta(2ct - \bar{z}), \quad (7.19)$$

where $\Theta(x)$ is the Heaviside step function³ and l_ϕ is the phase coherence length

$$l_\phi = \frac{\hbar^2 \rho_{1d}}{2mk_B T^-}, \quad (7.20)$$

which is basically the effective thermal coherence length of the relative phase between the two quasicondensates. Here again ρ_{1d} is the density of the original single condensate prior to splitting. For number squeezed states, we substitute the effective temperature with Eq. (7.16) and rewrite the phase coherence length as

$$l_\phi = \frac{2\hbar^2}{\xi_N^2 m g_{1D}}. \quad (7.21)$$

This means that l_ϕ is larger for states with enhanced number squeezing. The time it takes before the thermal correlation establishes itself across the phase coherence length, $l = l_\phi$, is referred to as the prethermalisation time [96, 103]

$$\tau \approx \frac{l_\phi}{2c}. \quad (7.22)$$

Thus it also takes longer before the number-squeezed states prethermalise. The phase coherence length is estimated to be $l_\phi = 8 \mu\text{m}$ with $\xi_N^2 = 1$. Combined with Eq. (7.22), we estimate a prethermalisation time $\tau \approx 3$ ms. With number squeezing $\xi_N^2 = 0.3$, we estimate the prethermalisation time $\tau = 10$ ms. However, we need to emphasise that the prethermalisation time in Eq. (7.22) is based on a splitting quench where the thermal correlation propagation starts at separation $\bar{z} = 0$. To achieve number squeezed states as shown in Fig. 7.8, we perform BEC splitting at a slower speed. Thus at the end of the ramp $t = 0$, the thermal correlation has already propagated for some time t' . Thus we need to revise $\tau = t + t'$. It is not straightforward to verify the prethermalisation time for split condensates resulting from slow ramps experimentally, as t' is hard to

³ $\Theta(x) = 1$, if $x > 0$, and 0 otherwise.

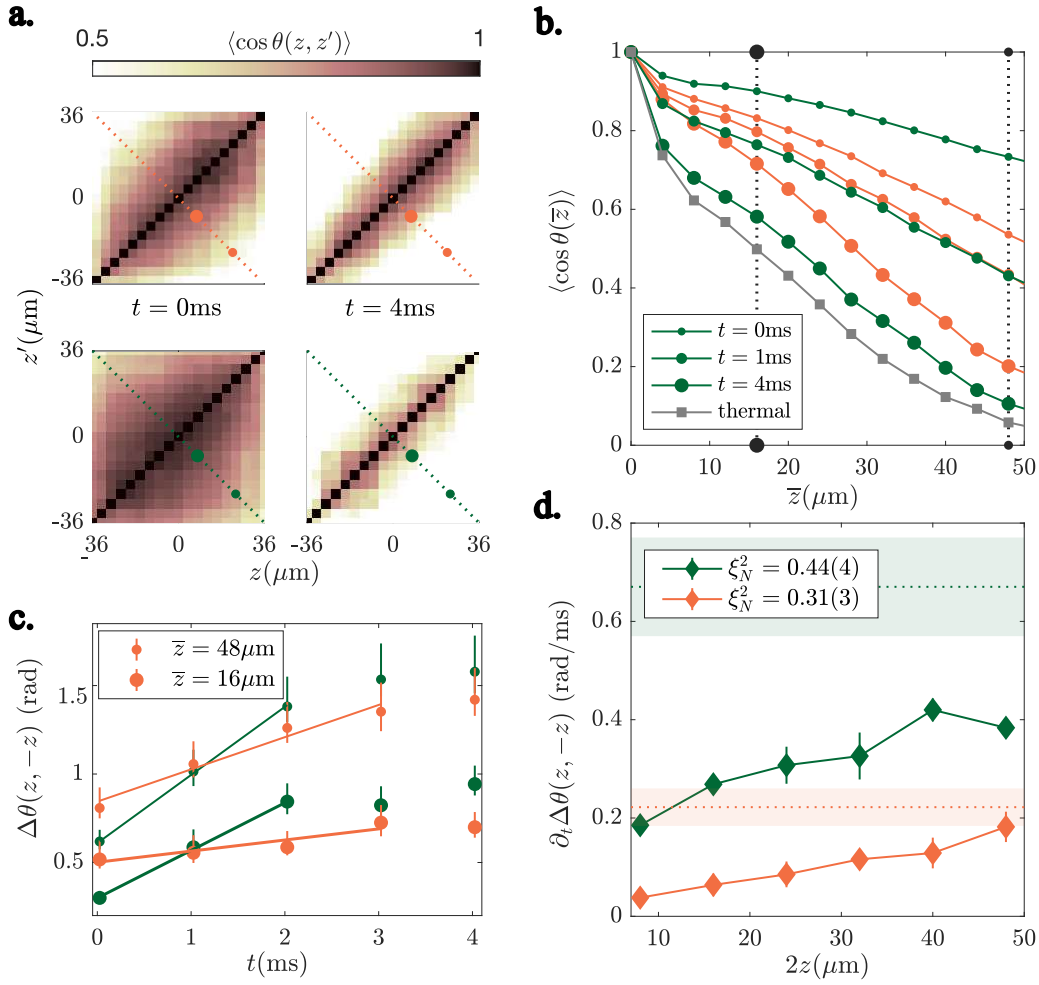


FIGURE 7.8: **Influence of number squeezing on multimode phase correlation function.** **a.** Phase correlation function (PCF) $\langle \cos \theta(z, z') \rangle$ between two spatial positions z and z' along the condensates. Upper and lower panels show PCF of a state with $\xi_N^2 = 0.44(4)$ (orange) and $0.31(3)$ (green) at time t after splitting to DW at $\mathcal{A} = 0.6$. **b.** Spatially averaged PCF, $\langle \cos \theta(\bar{z}) \rangle$, with $\bar{z} = |z - z'|$ from **a.** visualises how number squeezing suppresses decay of PCF. The grey line is the obtained PCF with direct cooling into this trap. **c.** Evolution of $\Delta\theta(z, -z)$ for $z = 8\mu\text{m}$ (big circle) and $z = 24\mu\text{m}$ (small circle). We infer the dephasing rate $\partial_t \Delta\theta(z, -z)$ with a linear fit and plot the extracted rates in **d** (see Fig. 7.9 for all distances z). The shaded regions represent the extracted global phase diffusion rate. We observe a spatial dependence of $\partial_t \Delta\theta(z, -z)$ along the condensates, which hints at local number squeezing originating from the multimode dynamics of quasicondensates.

infer.

After the state has prethermalised, the two-point PCF between the two split condensates behaves like two decoupled condensates at thermal equilibrium with an effective temperature T^- with the phase coherence length l_ϕ ,

$$\langle \cos(\theta(z, z')) \rangle = \exp(-|z - z'|/l_\phi). \quad (7.23)$$

Typically the effective temperature $T^- < T$, we expect the prethermal states to exhibit a higher phase correlation compared to the thermal states. However, the measured PCFs of the prethermalised states are actually not too far from the experimentally measured thermal equilibrium state of the double well from directly cooling (grey line in Fig. 7.8b). See Sec. 4.1 for discussions on direct cooling. The first possibility is that the temperature of the BECs is comparable to the effective temperature T^- . From the PCF of direct cooling, we estimate $l_\phi \approx 15 \mu\text{m}$, which gives $T \approx 10 \text{ nK}$. Even though, we do not have a precise measure of the temperature. It is less likely that the BECs are cooled to below 20 nK from empirical experiences.

Another possibility is that the tunnel coupling is non-vanishing, $J > 0$, so that the finite phase restoration length between two coupled condensates

$$l_J = \sqrt{\hbar/4mJ}, \quad (7.24)$$

protects the spatial phase coherence. For $\mathcal{A} = 0.6$ trap, even though the estimated J based on single particle eigenstates gives $J \approx 10^{-2} \text{ Hz}$. We know from the measured plasma and squeezing oscillation frequency in Fig. 6.7 that the real tunnel coupling is stronger due to the interaction broadened wavefunction. Plugging the measured plasma frequency $f_p = 15 \text{ Hz}$ into Eq. (5.3), we can infer that the tunneling strength is $J \approx 0.1 \text{ Hz}$. This gives a phase restoration length $l_J \approx 40 \mu\text{m}$, which is shorter than the condensate length. This is thus a contributing factor to the comparable PCFs between prethermal states and thermal states.

Another cause is that the limited imaging resolution smears out the correlation⁴. The imaging resolution of $\delta z = 4 \mu\text{m}$ is comparable to the phase coherence length l_ϕ . In reality, the resolution is poorer due to the random walk of atoms in the Light Sheet. From evaluation Fig. 8.3, we estimate the width of the point spread function to be 3 – 5 pixels, namely 12 – 15 μm . For more details see Sec. 8.1. It has been shown in the [107] that an imperfect imaging system smoothens out the phase correlation function. The smearing together with the inhomogeneous atomic density leads to the smoothing of PCF. Thus during the relaxation to the prethermal states, the PCFs present themselves as an overall lowering of the exponentially decaying $\cos\theta(z, z', t)$ over time. This is in contrast to the propagation of the thermal correlations as demonstrated in [103], where the plateau outside the light cone ($z = ct$) decreases exponentially over time.

In addition to the two-point PCF, one can also employ the two-point phase standard deviation $\Delta\theta(z, z')$ between two points z and z' in the relative phase field $\phi(z)$ to better quantify the local dephasing, see Fig. 2.2. We display in Fig. 7.8c, the evaluated $\Delta\theta(z, -z)$ between the symmetric points z and $-z$ and its evolution over time with a linear fit. At different separations $\bar{z} = 2z$, the linear fit gives different dephasing rates $\partial_t \Delta\theta$. The full set of $\Delta\theta(z, -z)$ evolution at spatial separations $\bar{z} = 2z$ with $z = 4 - 24 \mu\text{m}$ is plotted in Fig. 7.9. And the fitted linear dephasing rates are plotted in Fig. 7.8d. The overall dephasing rates are lower for enhanced number-squeezed states. This means that number

⁴2 ms of the imaging pulse was used in this data set

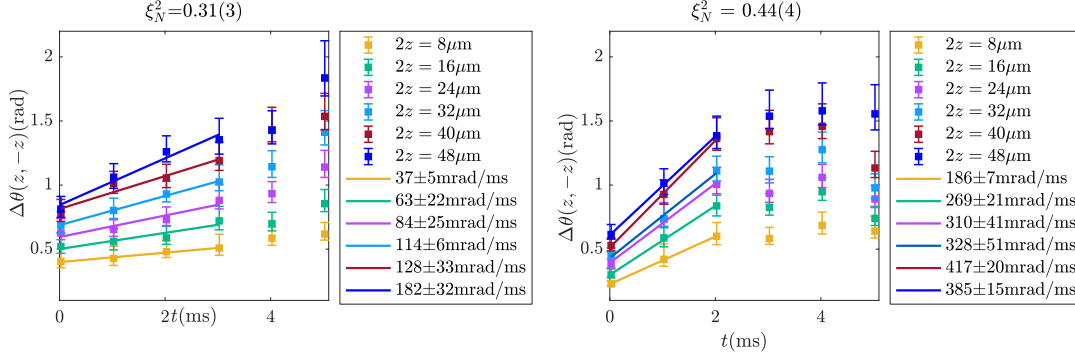


FIGURE 7.9: Evolution of fluctuations of the two-point relative phase $\Delta\theta(z, -z)$ between two symmetrically located points around the longitudinal centre of the BEC. Left panel: $\Delta\theta(z, -z)$ evolution with global number squeezing $\xi_N^2 = 0.31(3)$ and a linear fit on the time instances up to 3 ms. Right panel: $\Delta\theta(z, -z)$ evolution with global number squeezing $\xi_N^2 = 0.44(4)$ and a linear fit on time instances up to 2 ms.

squeezing suppresses spatial dephasing. In addition, we observe a spatial dependence of the dephasing rates. The origin of this trend is not very clear. And no explicit dependence on z is expected. We make two simple arguments in the following on the experimental observation of spatial dependence of dephasing rate. In both cases, further verifications are needed.

In [24, 47], the relaxation dynamics of harmonically trapped condensates are studied. For harmonically trapped BECs, the longitudinal density profile can be approximated with the Thomas-Fermi profile $\rho(z) = \rho_0(1 - (z/R_{TF})^2)$, where R_{TF} is the Thomas-Fermi radius. In the case of splitting (non-quench), the fluctuations are instead

$$\langle \rho_-(z)^2 \rangle = \xi_\rho^2(z)\rho(z), \quad \langle \phi(z)^2 \rangle = \frac{1}{\xi_\rho^2(z)\rho(z)}, \quad (7.25)$$

where ξ_ρ^2 is the local squeezing factor. The mode occupation n_j on the other hand can be shown to be very similar to the homogeneous density case [47], which is what we based our most analytical insight on. The evolution of the two-point phase variance is

$$\Delta\theta^2(z, z', t) = \frac{\pi\nu_N}{2R_{TF}} \sum_{j \geq 1} \frac{[f_j(z) - f_j(z')]^2}{\omega_j} (1 + 2n_j), \quad (7.26)$$

where $f_j(z)$ is expressed to the Legendre polynomials $P_j(z/R_{RF})$ [79]

$$f_j(z) = \sqrt{j+1/2} \cdot P_j(z/R_{RF}). \quad (7.27)$$

We refer to Fig. 4 in [106] for the evolution of PCF of trapped condensates. It behaves very similarly to the homogeneous case with some minor deviations. To derive an exact formula of dephasing rate for trapped condensates to fit with our experimental finding in Fig. 7.8d is not very trivial. But the density-dependent fluctuations in Eq. (7.25) and the "curved" plateau outside the light cone both align with our experimental observations in Fig. 7.8.

The second argument is in connection to previous work on the experimental observation of different effective temperatures in even and odd modes [47, 80], we follow the line of thought and define the mode-resolved squeezing ξ_j^2 based on the relation with the global squeezing factor ξ_N^2 ,

$$\Delta N_-^2 = \xi_N^2 N = \sum_k \xi_k^2 \rho_{-,k}. \quad (7.28)$$

Note here that we made the squeezing factor ξ_k^2 explicitly mode dependent. This is based on the observation of mode-dependent effective temperatures derived from generalised Gibbs ensemble [108]. The k -modes in Luttinger liquid theory are independent harmonic oscillators, meaning that the squeezing level in each mode is not necessarily equal. Thus, the mode-resolved effective temperature in Eq. (2.73) can be expressed as

$$k_B T_k^- = \frac{g_{1D} \langle \rho_{-,k}^2 \rangle}{4} = \frac{g_{1D} \xi_k^2 \rho_{-,k}}{4}. \quad (7.29)$$

A general description of the time evolution of the phase variance⁵ based on the Heisenberg equation of motion is

$$\langle \Delta \theta^2(\bar{z}, t) \rangle = \int_0^\infty \frac{dk}{2\pi} \langle \phi_k^2(t) \rangle [1 - \cos(k\bar{z})], \quad (7.30)$$

where the time-dependent phase variance $\langle \phi_k^2(t) \rangle$ is as expressed in Eq.(7.14). As previously mentioned, the initial phase variance depends on the exact preparation of the BECs in decoupled double wells. By assuming a k -dependence of effective temperatures $T_k^- \propto k^\alpha$ and an initial phase fluctuation obeying the thermal equilibrium in Eq. (2.73) at T_k^- , we can express the time evolution of twp-point phase variance as

$$\langle \Delta \theta(\bar{z}, t')^2 \rangle \propto [(\bar{z} + ct')^{1-\alpha} + (\bar{z} - ct')^{1-\alpha}], \quad (7.31)$$

which showcases an explicit connection between spatial dephasing on the spatial separation \bar{z} . With the typical assumption of equal energy stored in each mode, $\alpha = 0$, we recover Eq. (7.19). However, as the power-law scaling of T_k^- is not anticipated, the expression in Eq. (7.31) serves more as an illustration of the potential outcomes resulting from unequal mode temperatures.

The short-term dynamics after BEC splitting as a result of different levels of number squeezing can be well explained by relaxation to the prethermal states. Better number squeezing results in lower effective temperatures and thus lower dephasing rates. We will study the long-term influence of spin squeezing on spatial phase coherence in the next subsection.

⁵ $\int \frac{dk}{2\pi} \frac{A}{k^2} (1 - \cos(k\bar{z})) = \frac{A|\bar{z}|}{2}$

Preparation routine	Phase diffusion rate R (mrad/ms)	Spin squeezing factor $\xi_S^2 = \xi_N^2 / \langle \cos \Phi \rangle^2$
fast two-step	200 ± 18	≈ 0.4
single slow ramp	139 ± 27	≈ 0.63
single fast ramp	255 ± 34	≈ 0.80

TABLE 7.1: **Characterising split BECs with three different preparation routines** The resulting states of the split BECs are characterised with fitted global phase diffusion rates and the estimated spin squeezing factors by performing complementary measurements in number and phase quadrature.

7.3.3 Long term evolution

The experimental outcomes presented in this section primarily serve to demonstrate the prolonged spatial phase coherence attained via fast two-step compared to single linear ramps. As a characterisation of the global observables, we plot in Tab. 7.1 the inferred global phase diffusion rates and the spin squeezing factors with the three different approaches. The most optimal spin squeezing is obtained with the fast two-step approach (discussed in Sec. 4.1).

In Fig. 7.10, we show the evolution of fluctuation of the two-point relative phase $\Delta\theta(z, z')$ in the decoupled trap $\mathcal{A} = 0.65$ with three different preparation routines: **a.** a fast single ramp with $\kappa = 0.08 \text{ ms}^{-1}$ **b.** a slow single ramp with $\kappa = 0.08 \text{ ms}^{-1}$ and **c.** a fast two-step⁶. In **d** we plot collectively the fitted dephasing rates from **a** (blue), **b** (orange) and **c** (black). Fast two-step yields comparable dephasing rates $R_z = \partial_z \Delta\theta(z, z')$ as the slow single ramp. This is evidence for the comparable number squeezing factors of these two approaches. While the fast single ramp results in significantly larger dephasing rates.

After the initial dephasing (up to ~ 5 ms after the splitting), the states relax to the prethermal states, as discussed in Sec. 7.3.2. No obvious change in $\Delta\theta(z, z')$ is observed beyond these time instances. We note that in the dephased limit, the final $\Delta\theta(\bar{z} = 48 \mu\text{m}) \approx 1.5$ with fast two-step approach is smaller than obtained with single ramps $\Delta\theta(\bar{z} = 48 \mu\text{m}) \approx 2$. This means that the spatial phase coherence is overall higher in states prepared with two-step splitting.

To quantify the overall spatial phase coherence, we use the mean squared contrast $\langle C^2 \rangle$ defined in Eq. (7.11) and plot in Fig. 7.11 the evolution of $\langle C^2 \rangle$ with the three approaches (Fig. 7.10.) Compared to the two single linear ramps, the fast two-step sequence results in higher $\langle C^2 \rangle$ and its decay is more suppressed over a longer time. With similar levels of number squeezing between the fast two-step and the slow single ramp, the decay rates of $\langle C^2 \rangle$ are also comparable. But since thermal correlation already propagates (aka dephasing) during the slow ramp-up, the initial $\langle C^2 \rangle$ right after the splitting is much lower with a slow ramp. We conclude from this that enhanced spin squeezing leads to

⁶The two-step quench sequence: ramping up from single well $\mathcal{A} = 0.28$ to strongly coupled double well $\mathcal{A} = 0.5$ in 3ms, hold for 1.65ms and ramp to decoupled double well $\mathcal{A} = 0.65$ in 2ms.

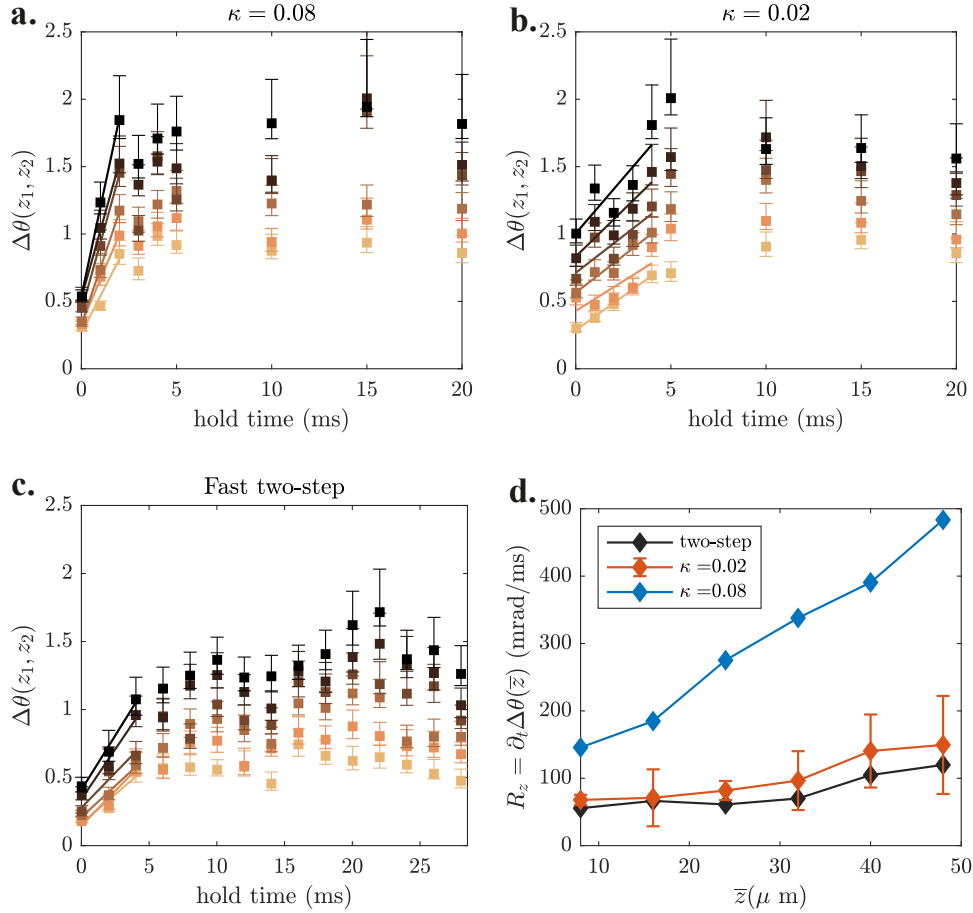


FIGURE 7.10: **Comparison on local dephasing rate of two-point relative phase $\theta(z, z')$** Measured local dephasing over time $\Delta\theta(z, z')$ in the decoupled trap $\mathcal{A} = 0.65$ with (a) a single ramp at splitting speed $\kappa = 0.08 \text{ ms}^{-1}$, with (b) a single ramp at splitting speed $\kappa = 0.02 \text{ ms}^{-1}$ and (c) with fast two-step at $\kappa = 0.08 \text{ ms}^{-1}$. The fitted dephasing rates R_z at different separation $\bar{z} = z - z'$ in a. to c. are plotted in d.

higher spatial phase coherence, in terms of better initial phase coherence and subsequent suppressed decay in the decoupled trap. Effectively, longer phase coherence time is obtained with optimal spin-squeezed states.

In Fig. 7.11, we notice a not completely steady behaviour of $\langle C^2 \rangle$ from fast two-step (black) after the initial decay due to dephasing. At longer evolution times, we observe a revival-like trend that coincides with previously observed recurrence phenomenon in 1D Bose gases [22, 47, 66]. This phenomenon is typical for non-equilibrium states, where the rotation between phase and density fluctuations (Eq. (2.73)) leads eventually to rephasing at time instances coinciding with the period of the first k -mode, $\Delta T = 1/\omega_1$. For harmonically trapped condensates, the period of rephasing is $\Delta T = 1/\omega_z$ for the $k = 1$ mode, see Eq. (2.65). In addition, the revival peak in PCF is broadened [47, 66] caused by the incommensurate energy spectrum of the modes. But as we will see, this is hard to disentangle from the induced longitudinal breathing motion from BEC splitting.

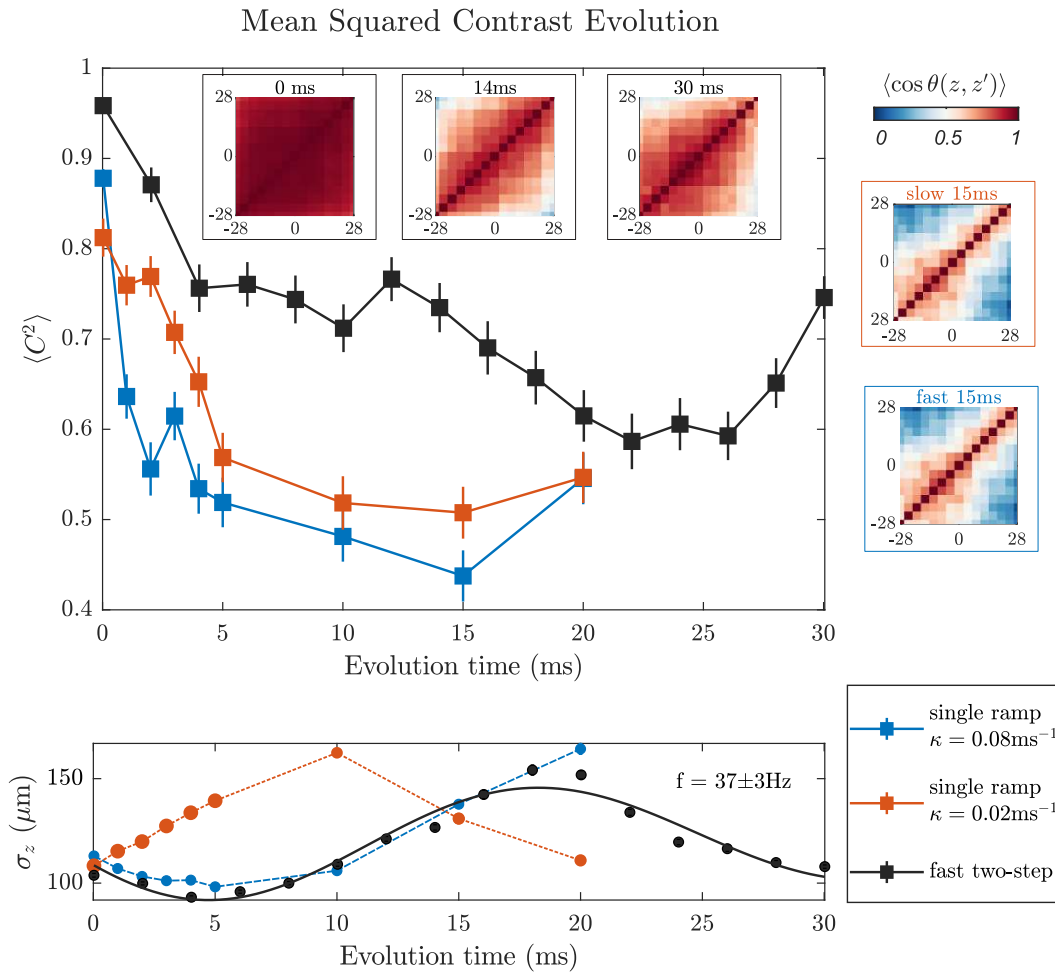


FIGURE 7.11: $\langle C^2 \rangle$ evolution of spin squeezed states in decoupled double wells. We compare three different preparation routines resulting in different spin squeezing factors (shown in Tab. 7.1). **Upper panel:** We show the evolution of the mean squared contrast $\langle C^2 \rangle = \sum_{z, z'} \langle \cos(\theta(z, z')) \rangle$ in the decoupled trap $\mathcal{A} = 0.65$. The best spin-squeezed state is achieved with the fast two-step and yields higher $\langle C^2 \rangle$ over longer times. **Lower panel:** we display the longitudinal widths σ_z evolution over time, where the width from fast two-step (black dots) is fitted with a sinusoidal function. The width oscillates at $f = 37(3)$ Hz after TOF, which corresponds to twice the longitudinal trap frequency, $f = 2f_z$. We display the two-point phase correlation function at some time instances in the insets.

We plot the longitudinal width after TOF in the lower panel in Fig. 7.11 and extrapolate a frequency of $37(5)$ Hz. From here we deduce the longitudinal trap frequency $f_z = 18.5$ Hz. The frequency doubling after TOF in the quasi-condensate regime stems from a self-reflection mechanism due to the repulsive interactions [109]. We remark that the induced longitudinal motions (more detail in Fig. B.1) do not coincide with the trend in phase coherence, especially the revival of $\langle C^2 \rangle$ around 25 – 30 ms with fast two-step. To confirm the revival, we need to let the system evolve for a longer time.

Chapter 8

Towards resolving mode dynamics

In this outlook chapter, we present some insights towards resolving number squeezing in higher modes based on the current experimental results. In Sec. 8.1, we characterize our imaging system with respect to resolving local number squeezing. In Sec. 8.2, we present some simulation results on generating 1D quasicondensates at thermal equilibrium based on the Ornstein-Uhlenbeck process [110, 111]. We compare this to the experimental results and identify some resembling features. In Sec. 8.3, we present the emerging local relative density fluctuations with distinctive structures resulting from different preparation schemes. In Sec. 8.4, we summarise and envision future projects in connection to this work.

8.1 Effective imaging resolution

As previously mentioned in Sec. 3.2, when the atoms fall through the light sheet, atoms undergo random walk while absorbing-remitting photons. The effective imaging resolution is then limited by this effect and effectively larger than the camera pixel size in the objective space $\delta z = 4 \mu\text{m}$. Now we focus on locating the lower bound on the longitudinal integration length, namely the effective imaging resolution for number squeezing estimation.

In Fig. 8.1, the longitudinal profile of the two BECs after TOF is plotted, which has a Lorentzian profile. In the middle panel, the number squeezing factor $\xi_N^2(\Delta z)$ as a function of the integration length, Δz , is plotted. Here the integration length is evaluated symmetrically around the longitudinal centre. We see that the calculated ξ_N^2 reaches a steady value with integration lengths above $\Delta z \approx 28 \mu\text{m}$. Below this length, classical correlations from the Fluorescence imaging dominate (see supplementary material in [15]). This length remarks an effective resolution of the imaging system. The length is still a few times smaller than the condensate length. In the right panel of Fig. 8.1, we also plot the total atom number as a function of the integration length. This is used as a reference as total atom number might also have an influence on number squeezing factor estimation.

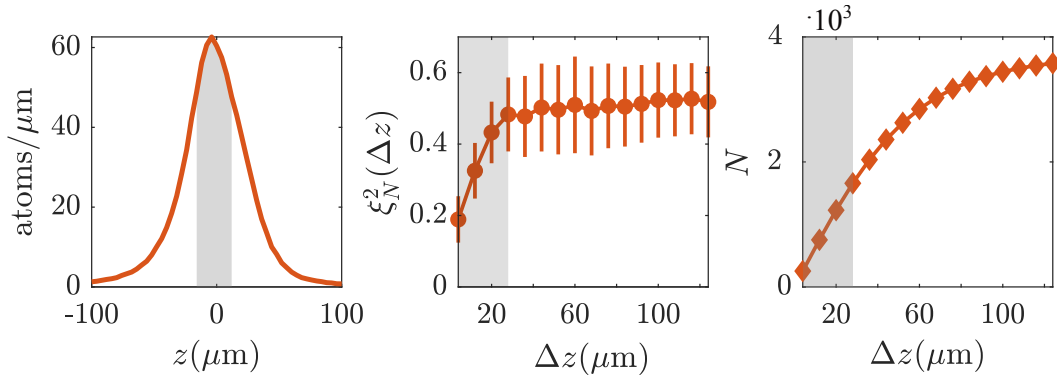


FIGURE 8.1: **Imaging influence on spatial number squeezing.** Left panel: Longitudinal profile of BEC. Δz is evaluated symmetrically around the peak density along the condensate. Middle panel: Influence of finite integration length Δz on evaluation of number squeezing factor ξ_N^2 . Right panel: Atom number N within the integration region Δz . The shaded region indicates the lower bound of Δz for reliable estimation of number squeezing factor ξ_N^2 .

8.2 Local number squeezing estimation

From the previous section, we learn that the imaging system allows us to potentially probe spatial correlations along the condensates. In this section, we would like to explore this possibility and check the influence of the TOF expansion on local number squeezing estimation. We compare the experimental results with simulations and see what further insights this provides us in understanding higher mode dynamics in 1D bosonic Josephson junction.

The simulation is based on the Ornstein-Uhlenbeck process. This process was originally proposed by [110, 111], but later generalized to describe the spatial phase fluctuations [110] and extended further for nonharmonic Hamiltonians [112] which has been used in [16]. Thus we refer to [112] for details on the simulation¹. The simulation allows us to simulate condensates at thermal equilibrium with arbitrary temperatures. For simulating BECs in double wells, we use independent Hamiltonian in discrete form for the common and relative degree of freedom with finite or vanishing tunnel coupling J . On top of that, the smearing effect on the simulated condensates, which is important considering finite imaging resolution; and a ballistic expansion during TOF are also included.

We simulate two 1D quasicondensates at thermal equilibrium with temperature $T = 10$ nK (in both the common and relative degree of freedom) in a double well with total atom number $N = 4000$. The condensates are trapped in a harmonic trap of 15 Hz in the longitudinal direction and radial trap frequency comparable to the experimental double well at $\mathcal{A} = 0.6$. We then switch off the trapping potential and expand the condensates ballistically for the same duration as the experimental TOF $t_F = 43.4$ ms for comparison with the experimental results. We engineer a relative number fluctuation between left and right condensates by sampling from a normal distribution with variance $\Delta^2 N_- = 0.4N$ and zero mean

¹The scripts are mainly developed by Thomas Schweigler during his PhD thesis [72].

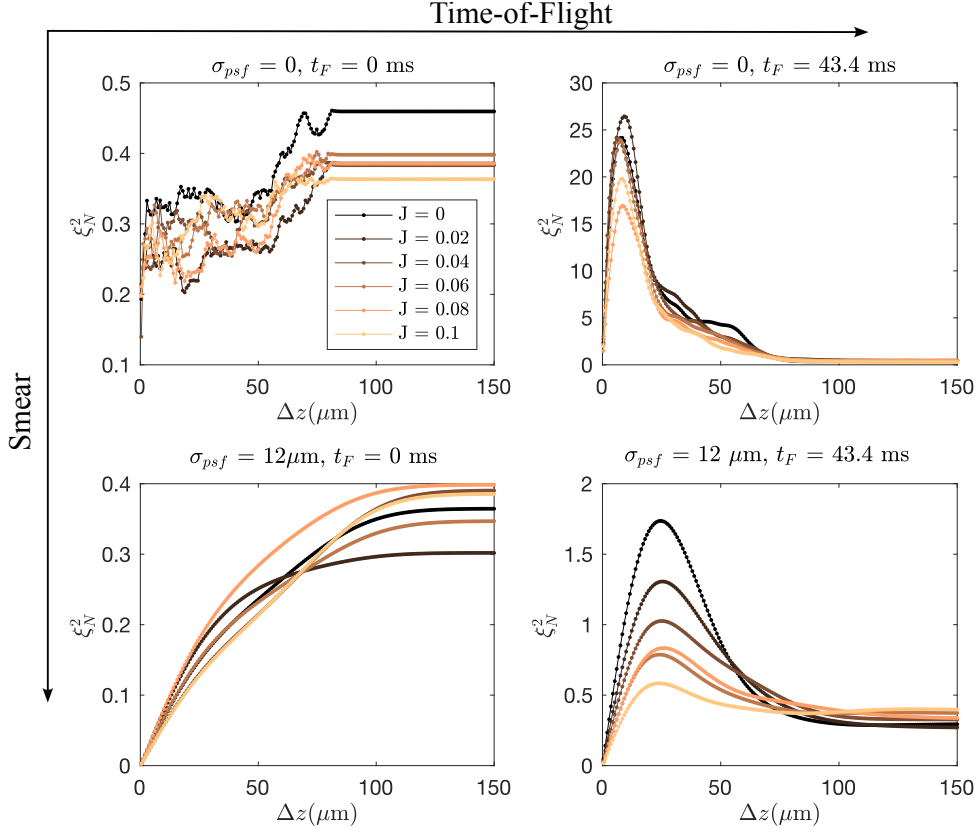


FIGURE 8.2: **Simulated number squeezing factor dependence on integration length.** We plot spatial dependence of ξ_N^2 as a function of tunnelling strength, J , between the BECs and include the effect originating from finite image blurring by adding a Gaussian blur with radius σ_{psf} and Time-of-Flight (TOF) expansion with duration t_F .

$\bar{N}_- = 0$. The atom number in the left and right condensates are respectively $N_L^i = N/2 + N_-^i$ and $N_R^i = N/2 - N_-^i$ for each single realisation i . In other words, we initialise the two condensates with a global number squeezing $\xi_N^2 = 0.4$.

In the upper left panel in Fig. 8.2, we show how the number squeezing factors ξ_N^2 scale with the integration length Δz of *in situ* BECs in a double well. We vary the tunnel-coupling strength J between the two BECs. Similar to Fig. 8.1, the region Δz is evaluated symmetrically around the longitudinal centre of the condensates. The evaluated ξ_N^2 for integration lengths $\Delta z < 80 \mu\text{m}$ appear random. This might be related to some numerical artefacts, for instance, finite simulation resolution. At larger integration lengths, $\Delta z > 80 \mu\text{m}$ (larger than the condensate lengths), the number squeezing factors become constant. These number squeezing factors are essentially the global number squeezing factors, which we initialized to be $\xi_N^2 = 0.4$. The estimated global number squeezing factors for decoupled condensates ($J = 0$) are larger than the imprinted squeezing factors $\xi_N^2 > 0.4$. This originates from the thermal fluctuations in the relative degree of freedom between BECs with finite temperature $T = 10 \text{ nK}$. Since the simulation is constructed in a way that the Ornstein-Uhlenbeck stochastic process is implemented in the relative and common degree of freedom at the

same temperature $T^- = T^+$, and then converted to left- and right- localised basis ($\psi_+, \psi_- \rightarrow \psi_L, \psi_R$). Thus the simulation output of the atom number in the left and right condensates has additional thermal noise on top of the initialized N_L^i and N_R^i . On the other hand, for condensates with finite tunnel coupling ($J > 0$), the estimated global number squeezing factors are smaller than $\xi_N^2 < 0.4$. This possibly stems from the tunnelling of particles between left and right wells seeking to reduce the number fluctuations in the relative degree of freedom (ground state).

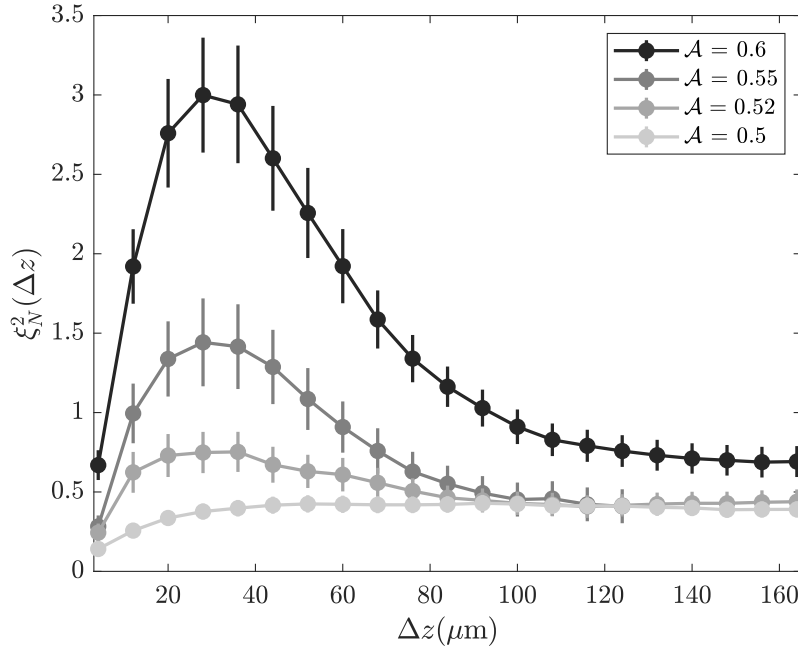


FIGURE 8.3: **Experimentally probed number squeezing factor dependence on integration length in various double wells.** The data is taken after splitting from a single well to various double wells \mathcal{A} with split speed $\kappa = 0.02 \text{ ms}^{-1}$.

We then add smearing and TOF expansion to see how they influence this dependence of number squeezing on integration length. For *in situ* condensates, by adding a Gaussian smearing function with radius $\sigma_{psf} = 12 \mu\text{m}$, we observe in the lower left panel in Fig. 8.2 the same type of classical correlation as observed in experimental results in Fig. 8.1. As pointed out earlier, this originates from the finite imaging resolution. After ballistically expanding the BEC for the same TOF duration as the experiment (upper and lower right panel in Fig. 8.2), the dependence of number squeezing factors on integration length exhibits a peak-like feature at the length around $\Delta z \approx 10 \mu\text{m}$ (without smearing $\sigma_{psf} = 0$). The peak heights increase with decreasing tunnel-coupling strength J . With added smearing $\sigma_{psf} = 12 \mu\text{m}$, the peaks in $\xi_N^2(\Delta z)$ are broadened and their heights are suppressed. The peak heights with smearing are positioned around $\Delta z \approx 25 \mu\text{m}$ and the width $\sim 40 \mu\text{m}$.

These features in the lower right panel in Fig. 8.2 match very well with the experimental results, shown in Fig. 8.3. We obtain the experimental results by splitting a BEC from a weakly dressed single well at the splitting speed $\kappa =$

0.02 ms^{-1} (Eq. (4.6)) into different double wells \mathcal{A} (aka. with different J). In the experimental results, the peak-like feature in $\xi_N^2(\Delta z)$ becomes increasingly more pronounced in less tunnel-coupled condensates. Note however the magnitudes of J used in the simulation (Fig. 8.2) are much smaller than we inferred earlier (in Fig. 3.3) for the experimental traps in Fig. 8.3. We are not so sure whether there might be some additional conversions in the simulation codes that are needed in order to compare with our inferred tunnel coupling. However since this has been known to be an issue, we have not investigated further on this matter for this thesis.

During the TOF expansion, the phase gradient contributes to the velocity field during expansion [46],

$$v(z) = \frac{\hbar}{m} \partial_z \phi(z). \quad (8.1)$$

Therefore the *in situ* fluctuating phases convert into density fluctuations after TOF expansion. This phenomenon is what leads to earlier experimental observations on density ripples [60]. Here, we emphasize that the density ripples originate from either the fluctuating phases in a single quasicondensate or the phase in the common degree of freedom between two quasicondensates [60]. It has been used for thermometry purposes [60, 113], since the pattern of density ripples are connected to the thermal coherence length (see Eq. (2.64)), therefore can be used to estimate the temperature of quasicondensates.

The structures observed in the $\xi_N^2(\Delta z)$ in the experimental result in Fig. 8.3 and the simulation result in Fig. 8.2 resemble the spectrum of density ripples in [113]. But in our case, the density fluctuations originate from the phase fluctuations in the relative degree of freedom between two quasicondensates. For strongly tunnel-coupled BECs, the phase-locking mechanism restores the spatial phase fluctuations. Therefore, the peaks in $\xi_N^2(\Delta z)$ are more suppressed with increasing tunnel coupling. This also matches with the experimental results in Fig. 8.3. The resolved structure of number squeezing over integration length might provide us with an alternative way of extrapolating the effective temperature T^- in the relative degree of freedom after BEC splitting. Further quantitative analysis is needed for this purpose.

8.3 Local relative density fluctuations

In order to prevent fluctuations in relative density $\Delta\rho_- = \sqrt{\langle(\rho_- - \langle\rho_-\rangle)^2\rangle}$ originating from the *in situ* relative phase fluctuations, we keep the double well in the strongly tunnel-coupled regime. In this trap, the relative phase fluctuations are strongly suppressed by phase locking. From the experimental results in Fig. 6.1, we estimate $\Delta\phi \approx 0.05$. This is evidenced by no peak feature in number squeezing estimation with partial integration, as shown in Fig. 8.3. Thus this double well, we expect the experimentally observed density fluctuation $\Delta\rho_-(z)$ after TOF to mainly stem from the *in situ* density fluctuations.

In Fig. 8.4, we show experimental results on the average local densities $\langle\rho_-\rangle$ and their fluctuations $\Delta\rho_-$ from different preparation routines of BEC in strongly

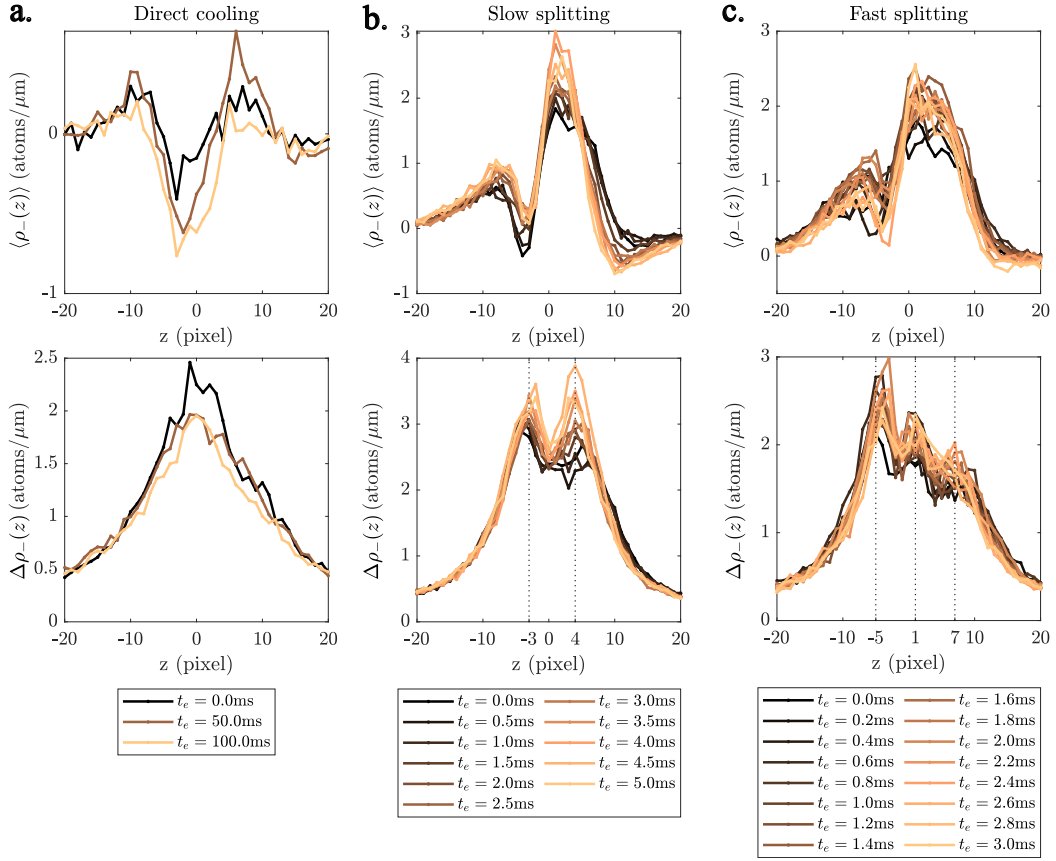


FIGURE 8.4: **Local relative density profile and its fluctuations between two strongly coupled BECs in double well with different preparation routines.**

a. prepare the two condensates in $\mathcal{A} = 0.5$ by direct cooling which signifies the thermal equilibrium states. **b.** and **c.** split from single well to with split speed $\kappa = 0.02 \text{ ms}^{-1}$ and 0.08 ms^{-1} respectively. $\langle \rho \rangle$ represents the mean relative density profile and $\Delta \rho_- = \sqrt{\langle (\rho_- - \langle \rho_- \rangle)^2 \rangle}$ represents the local density fluctuations along the condensates. t_e is the evolution time after initial preparation.

coupled double well, $\mathcal{A} = 0.5$. We plot the evolution of the profiles over hold time t_e in the double well. With direct cooling (see Sec. 4.1), we observe no distinct feature on $\Delta \rho_-(z)$, other than some dependence on the local background atomic density $\rho(z)$. On the contrary, BEC splitting results in pronounced structures in density fluctuations $\Delta \rho_-(z)$ as shown in Fig. 8.4 **b** and **c**.

In case of slow BEC splitting with $\kappa = 0.02 \text{ ms}^{-1}$ (Fig. 8.4**b**), two peaks in $\Delta \rho_-$ with separation $\bar{z}_1 \approx 30 \mu\text{m}$ are observed as shown in lower panel in Fig. 8.4**b**. With faster splitting at $\kappa = 0.08 \text{ ms}^{-1}$, three peaks with inter-peak distance of $\bar{z}_1 \approx 25 \mu\text{m}$ are observed on $\Delta \rho_-(z)$ profiles. These peaks likely originate from populations of specific phonon modes. As long as the k_j -mode can follow the evolving Hamiltonian during splitting, the quantum fluctuation in the relative density $\langle \rho_{-,j}^2 \rangle$ of each mode is minimized (same principle as global relative number). For lower modes the adiabaticity condition, $\dot{J}/J < \omega_j$, is violated at slower splitting speed, aka smaller \dot{J} . This coincides with our observation that fast splitting (Fig. 8.4**c**) leads to pronounced density fluctuations at shorter

wavelengths (higher k modes) compared to slow splitting (Fig. 8.4b). The experimental observations have not been investigated quantitatively. We present these findings mainly as a demonstration of the experimental capability of resolving mode squeezing in the future.

8.4 Outlook

In short summary, we have observed oscillations in the quantum fluctuations in a multimode bosonic Josephson Junction with 1D Bose gases in a double well. In this thesis, we only show results where we read out the system in either of the conjugate quadratures. Recently, we have also acquired some preliminary results on simultaneous readouts of both quadratures via outcoupling. This promises potential implications for performing state tomography and studying quantum backactions.

Building on the dynamical evolution of quantum states in tunnel-coupled BECs, we have developed a more efficient strategy to achieve improved spin-squeezed states. We anticipate a more streamlined method for preparing spin-squeezed states through the utilization of optimal control algorithms, which optimize the classical external dynamics following fast two-step sequences. The ability to monitor the squeezing dynamics offers a novel means of optimizing the preparation of strongly correlated sine-Gordon field simulators with lower effective temperatures. As we approach a regime dominated by quantum fluctuations, the potential for measuring entanglement entropy in quantum fields becomes achievable [114].

For hardware upgrade on the experimental setup, we are planning to use matter wave lensing [115–117] to allow improved imaging resolution on the longitudinal direction and flexibility on reading out the longitudinal dynamics in either momentum or spatial space. Furthermore, a digital micromirror device (DMD) for arbitrary shaping of the longitudinal confinement [118] is currently being implemented on the setup. This allows us to explore the 1D physics with homogeneous atomic densities [22], to prepare initial states for studying generalized hydrodynamics [119] or to investigate quantum field machines [120].

Appendix A

Double well characterisation

A.1 Two trap configurations

Trap configuration	OCT	MZI
small Ioffe (mA)	1.07	1.1705
big Bias (Gauss)	34.1	28.9
80 μm wire (A)	1	1
Hbar wire (A)	0.5	0.5
distance blow chip (μm)	49.5	61.9
RF wire 1 amplitude (mA)	$0.976 \cdot I_{max}$	$0.976 \cdot I_{max}$
RF wire 2 amplitude (mA)	$0.976 \cdot I_{max}$	$0.976 \cdot I_{max}$
RF frequency (kHz)	770	885
RF phase β (deg)	20	0
Trap bottom (kHz)	824	912
Trap frequency [f_{\perp}, f_z] (Hz)	[4.14E3, 20]	[2.94E3, 10]

TABLE A.1: Two trap configurations based on simulation: OCT and MZI, named after historical reasons. $I_{max} = 80.25$ mA is the maximal current for RF wire.

A.2 Double well trap bottom spectroscopy (OCT)

In Fig. A.1, the double well trap bottom spectroscopy of double well with $\mathcal{A} = 0.65$ is performed with varying split angles α . We estimate a symmetric double well at $\alpha = 6.7^\circ$. Note that the linear slope of the trap bottom difference between the left and right well, $\Delta TB = TB_L - TB_R$ is the opposite sign compared to the MZI configuration (see.3.9). The trap simulation in OCT configuration gives also a positive slope. This seems to be due to the exact MATLAB script used for computing the output currents in the two RF wires with split angle α as input. The script fixes the trap distance from the atom chip to be $l_0 = 61.9 \mu\text{m}$ for both OCT and MZI configurations. This results in a small mismatch between the I_1 and I_2 in the two configurations.

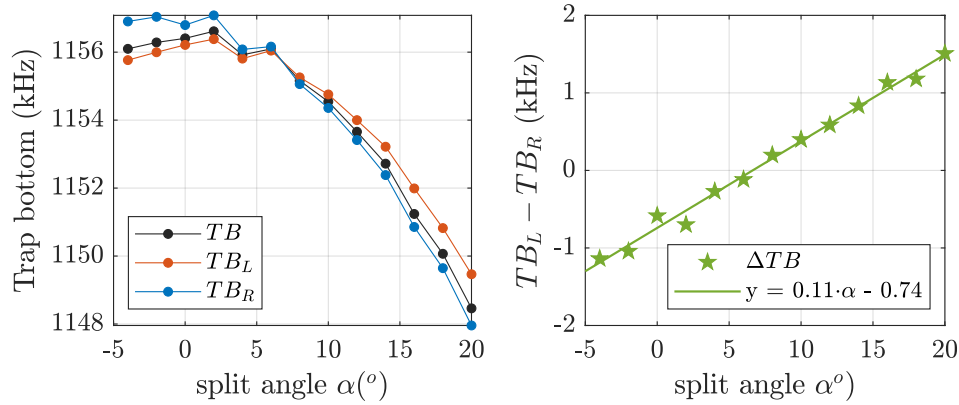


FIGURE A.1: **double well trap bottom at $\mathcal{A} = 0.65$ in OCT trap configuration.** Left panel: trap bottom of the left well, TB_L and right well, TB_R , together with the collective trap bottom, $TB = (TB_L + TB_R)/2$, are plotted as a function of split angle α . Right panel: The trap bottom difference between the left and right well is plotted against α . A linear fit estimate a balanced trap bottom at $\alpha \approx 6.7^\circ$.

Appendix B

Induced longitudinal motion

With our elongated magnetic trap $\omega_{\perp}/\omega_z \approx 200$, all dynamics in the radial direction are considered as a quench in the longitudinal timescale. With BEC splitting, due to a sudden halving of atom number in the original single well to the final double well, the split condensates are too long in the final longitudinal trap. This induces a dipolar excitation on the condensates, as we show in Fig. B.1. This motion is not simple breathing, but the centre-of-mass of the condensates also oscillates around the trap. This could originate from a slight shift of the longitudinal trap centre as a function of RF dressing. We show in Fig. B.2 the measured longitudinal trap frequency at different RF dressing amplitude.

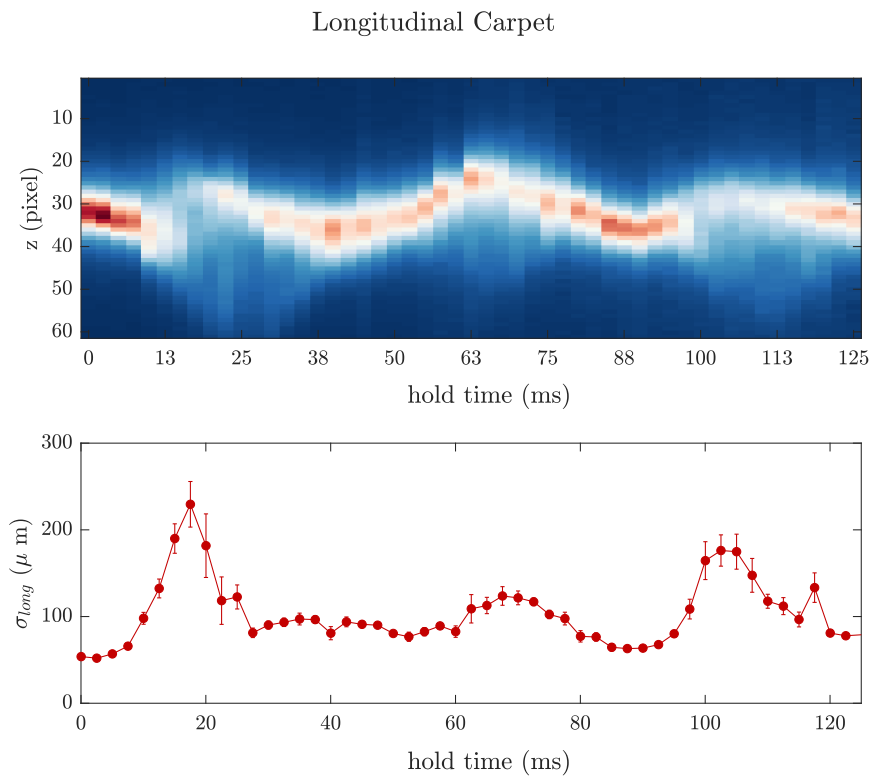


FIGURE B.1: **BEC splitting induced longitudinal motions** In OCT trap configuration, we split from $\mathcal{A} = 0.3$ to 0.57 in 10 ms with relative phase readout (interference pattern) and no Stern-Gerlach separation. The resulting longitudinal profile evolution is displayed (upper panel) with fitted longitudinal widths (lower panel).

We typically directly cool the single condensate in the single well with RF dressing amplitude $\mathcal{A} \sim 0.3$. This is to avoid the sudden change in trap frequency during the RF amplitude ramp-up. Experimentally, we also achieve colder BECs in the weakly dressed single well.

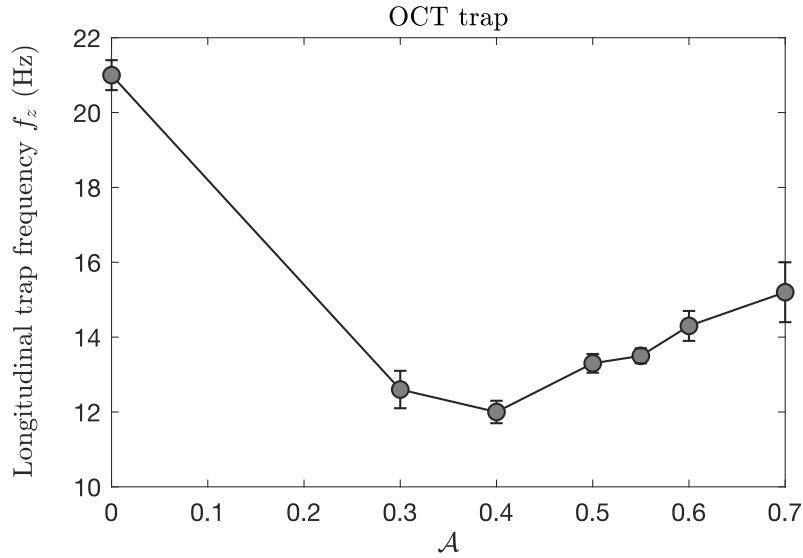


FIGURE B.2: Experimentally measured longitudinal trap frequency as a function of RF dressing amplitude \mathcal{A} . Tabor AWG was used as the RF dressing source.

Bibliography

- [1] Daniel F Walls. “Squeezed states of light”. In: *nature* 306.5939 (1983), pp. 141–146.
- [2] Chad Orzel et al. “Squeezed states in a Bose-Einstein condensate”. In: *Science* 291.5512 (2001), pp. 2386–2389.
- [3] Jerome Esteve et al. “Squeezing and entanglement in a Bose-Einstein condensate”. In: *Nature* 455.7217 (2008), pp. 1216–1219. DOI: <https://doi.org/10.1038/nature07332>. URL: <https://www.nature.com/articles/nature07332>.
- [4] Max F Riedel et al. “Atom-chip-based generation of entanglement for quantum metrology”. In: *Nature* 464.7292 (2010), pp. 1170–1173.
- [5] Bernd Lücke et al. “Twin matter waves for interferometry beyond the classical limit”. In: *Science* 334.6057 (2011), pp. 773–776. DOI: <https://doi.org/10.1126/science.1208798>. URL: <https://www.science.org/doi/10.1126/science.1208798>.
- [6] Masahiro Kitagawa and Masahito Ueda. “Squeezed spin states”. In: *Physical Review A* 47.6 (1993), p. 5138.
- [7] Vittorio Giovannetti, Seth Lloyd, and Lorenzo Maccone. “Advances in quantum metrology”. In: *Nature photonics* 5.4 (2011), pp. 222–229.
- [8] Luca Pezzè et al. “Quantum metrology with nonclassical states of atomic ensembles”. In: *Rev. Mod. Phys.* 90 (3 Sept. 2018), p. 035005. DOI: [10.1103/RevModPhys.90.035005](https://link.aps.org/doi/10.1103/RevModPhys.90.035005). URL: <https://link.aps.org/doi/10.1103/RevModPhys.90.035005>.
- [9] Christian L Degen, Friedemann Reinhard, and Paola Cappellaro. “Quantum sensing”. In: *Reviews of modern physics* 89.3 (2017), p. 035002.
- [10] Andrew D Ludlow et al. “Optical atomic clocks”. In: *Reviews of Modern Physics* 87.2 (2015), p. 637.
- [11] Junaid Aasi et al. “Enhanced sensitivity of the LIGO gravitational wave detector by using squeezed states of light”. In: *Nature Photonics* 7.8 (2013), pp. 613–619.
- [12] Roman Schmied et al. “Bell correlations in a Bose-Einstein condensate”. In: *Science* 352.6284 (2016), pp. 441–444.
- [13] Matteo Fadel et al. “Spatial entanglement patterns and Einstein-Podolsky-Rosen steering in Bose-Einstein condensates”. In: *Science* 360.6387 (2018), pp. 409–413. DOI: [10.1126/science.aao1850](https://doi.org/10.1126/science.aao1850). URL: <https://www.science.org/doi/10.1126/science.aao1850>.
- [14] Karsten Lange et al. “Entanglement between two spatially separated atomic modes”. In: *Science* 360.6387 (2018), pp. 416–418. DOI: [10.1126/science.aao2035](https://doi.org/10.1126/science.aao2035). URL: <https://www.science.org/doi/10.1126/science.aao2035>.

- [15] Philipp Kunkel et al. “Spatially distributed multipartite entanglement enables EPR steering of atomic clouds”. In: *Science* 360.6387 (2018), pp. 413–416. DOI: 10.1126/science.aao2254. URL: <https://www.science.org/doi/10.1126/science.aao2254>.
- [16] Thomas Schweigler et al. “Experimental characterization of a quantum many-body system via higher-order correlations”. In: *Nature* 545.7654 (2017), pp. 323–326. DOI: <https://doi.org/10.1038/nature22310>. URL: <https://www.nature.com/articles/nature22310>.
- [17] Iulia Buluta and Franco Nori. “Quantum simulators”. In: *Science* 326.5949 (2009), pp. 108–111.
- [18] Immanuel Bloch, Jean Dalibard, and Sylvain Nascimbene. “Quantum simulations with ultracold quantum gases”. In: *Nature Physics* 8.4 (2012), pp. 267–276. DOI: 10.1038/NPHYS2259. URL: <https://www.nature.com/articles/nphys2259>.
- [19] Iulia M Georgescu, Sahel Ashhab, and Franco Nori. “Quantum simulation”. In: *Reviews of Modern Physics* 86.1 (2014), p. 153.
- [20] Rainer Blatt and Christian F Roos. “Quantum simulations with trapped ions”. In: *Nature Physics* 8.4 (2012), pp. 277–284.
- [21] M. Gring et al. “Relaxation and Prethermalization in an Isolated Quantum System”. In: *Science* 337.6100 (2012), pp. 1318–1322. DOI: 10.1126/science.1224953. URL: <https://www.science.org/doi/abs/10.1126/science.1224953>.
- [22] Bernhard Rauer et al. “Recurrences in an isolated quantum many-body system”. In: *Science* 360.6386 (2018), pp. 307–310.
- [23] Marine Pigneur et al. “Relaxation to a phase-locked equilibrium state in a one-dimensional bosonic Josephson junction”. In: *Physical review letters* 120.17 (2018), p. 173601. DOI: <https://doi.org/10.1103/PhysRevLett.120.173601>.
- [24] J-F Mennemann et al. “Relaxation in an extended bosonic Josephson junction”. In: *Physical Review Research* 3.2 (2021), p. 023197. DOI: <https://doi.org/10.1103/PhysRevResearch.3.023197>.
- [25] BJ Dalton and S Ghanbari. “Two mode theory of Bose–Einstein condensates: interferometry and the Josephson model”. In: *Journal of Modern Optics* 59.4 (2012), pp. 287–353. URL: <https://doi.org/10.1080/09500340.2011.632100>.
- [26] Sin-itiro Tomonaga. “Remarks on Bloch’s method of sound waves applied to many-fermion problems”. In: *Progress of Theoretical Physics* 5.4 (1950), pp. 544–569.
- [27] JM Luttinger. “An exactly soluble model of a many-fermion system”. In: *Journal of mathematical physics* 4.9 (1963), pp. 1154–1162.
- [28] Daniel C Mattis and Elliott H Lieb. “Exact solution of a many-fermion system and its associated boson field”. In: *Condensed Matter Physics and Exactly Soluble Models: Selecta of Elliott H. Lieb* (2004), pp. 645–653.
- [29] Thomas Betz et al. “Two-point phase correlations of a one-dimensional bosonic Josephson junction”. In: *Physical review letters* 106.2 (2011), p. 020407.

- [30] Pjotrs Grišins and Igor E Mazets. “Coherence and Josephson oscillations between two tunnel-coupled one-dimensional atomic quasicondensates at finite temperature”. In: *Physical Review A* 87.1 (2013), p. 013629.
- [31] Ofir E Alon, Alexej I Streltsov, and Lorenz S Cederbaum. “Multiconfigurational time-dependent Hartree method for bosons: Many-body dynamics of bosonic systems”. In: *Physical Review A* 77.3 (2008), p. 033613.
- [32] Michael H Beck et al. “The multiconfiguration time-dependent Hartree (MCTDH) method: a highly efficient algorithm for propagating wavepackets”. In: *Physics reports* 324.1 (2000), pp. 1–105.
- [33] Axel UJ Lode et al. “Colloquium: Multiconfigurational time-dependent Hartree approaches for indistinguishable particles”. In: *Reviews of Modern Physics* 92.1 (2020), p. 011001.
- [34] Ph Nozieres and D Saint James. “Particle vs. pair condensation in attractive Bose liquids”. In: *Journal de Physique* 43.7 (1982), pp. 1133–1148.
- [35] C. J. Myatt et al. “Production of Two Overlapping Bose-Einstein Condensates by Sympathetic Cooling”. In: *Phys. Rev. Lett.* 78 (4 Jan. 1997), pp. 586–589. DOI: [10.1103/PhysRevLett.78.586](https://doi.org/10.1103/PhysRevLett.78.586). URL: <https://link.aps.org/doi/10.1103/PhysRevLett.78.586>.
- [36] G. Thalhammer et al. “Double Species Bose-Einstein Condensate with Tunable Interspecies Interactions”. In: *Phys. Rev. Lett.* 100 (21 May 2008), p. 210402. DOI: [10.1103/PhysRevLett.100.210402](https://doi.org/10.1103/PhysRevLett.100.210402). URL: <https://link.aps.org/doi/10.1103/PhysRevLett.100.210402>.
- [37] Yuki Kawaguchi and Masahito Ueda. “Spinor bose-einstein condensates”. In: *Physics Reports* 520.5 (2012), pp. 253–381.
- [38] GJ Milburn et al. “Quantum dynamics of an atomic Bose-Einstein condensate in a double-well potential”. In: *Physical Review A* 55.6 (1997), p. 4318. DOI: <https://doi.org/10.1103/PhysRevA.55.4318>.
- [39] Augusto Smerzi et al. “Quantum coherent atomic tunneling between two trapped Bose-Einstein condensates”. In: *Physical Review Letters* 79.25 (1997), p. 4950. DOI: <https://doi.org/10.1103/PhysRevLett.79.4950>. URL: <https://journals.aps.org/prl/abstract/10.1103/PhysRevLett.79.4950>.
- [40] Paul Adrien Maurice Dirac. “The quantum theory of the emission and absorption of radiation”. In: *Proceedings of the Royal Society of London. Series A, Containing Papers of a Mathematical and Physical Character* 114.767 (1927), pp. 243–265.
- [41] P Carruthers and Michael Martin Nieto. “Phase and angle variables in quantum mechanics”. In: *Reviews of Modern Physics* 40.2 (1968), p. 411.
- [42] Fortunato Tito Arecchi et al. “Atomic coherent states in quantum optics”. In: *Physical Review A* 6.6 (1972), p. 2211.
- [43] David Ananikian and Thomas Bergeman. “Gross-Pitaevskii equation for Bose particles in a double-well potential: Two-mode models and beyond”. In: *Physical Review A* 73.1 (2006), p. 013604.
- [44] Anthony J Leggett. “Bose-Einstein condensation in the alkali gases: Some fundamental concepts”. In: *Reviews of modern physics* 73.2 (2001), p. 307.

- [45] David J Wineland et al. “Squeezed atomic states and projection noise in spectroscopy”. In: *Physical Review A* 50.1 (1994), p. 67. DOI: <https://doi.org/10.1103/PhysRevA.50.67>. URL: <https://journals.aps.org/pr/abstract/10.1103/PhysRevA.50.67>.
- [46] Lev Pitaevskii and Sandro Stringari. *Bose-Einstein condensation and superfluidity*. Vol. 164. Oxford University Press, 2016.
- [47] Sebastian Anton Erne. “Far-From-Equilibrium Quantum Many-Body Systems: From Universal Dynamics to Statistical Mechanics”. PhD thesis. 2018. DOI: 10.11588/heidok.00025106. URL: <http://www.ub.uni-heidelberg.de/archiv/25106>.
- [48] Elliott H Lieb. “Exact analysis of an interacting Bose gas. II. The excitation spectrum”. In: *Physical Review* 130.4 (1963), p. 1616.
- [49] Mohammadamin Tajik et al. “Experimental observation of curved light-cones in a quantum field simulator”. In: *Proceedings of the National Academy of Sciences* 120.21 (2023), e2301287120.
- [50] DS Petrov, GV Shlyapnikov, and JTM Walraven. “Regimes of quantum degeneracy in trapped 1D gases”. In: *Physical Review Letters* 85.18 (2000), p. 3745.
- [51] Robert Bücke. “Twin-atom beam generation in a one-dimensional Bose gas”. PhD thesis. 2013.
- [52] Sandrine van Frank. “Coherent control over the motional states of a Bose-Einstein condensate and applications”. PhD thesis. 2015.
- [53] Tarik Berrada. “Mach-Zehnder interferometry with interacting Bose-Einstein condensates in a double-well potential”. PhD thesis. 2014. DOI: <https://doi.org/10.34726/hss.2014.24705>.
- [54] Jean Dalibard and Claude Cohen-Tannoudji. “Laser cooling below the Doppler limit by polarization gradients: simple theoretical models”. In: *JOSA B* 6.11 (1989), pp. 2023–2045.
- [55] William H Wing. “On neutral particle trapping in quasistatic electromagnetic fields”. In: *Progress in Quantum Electronics* 8.3-4 (1984), pp. 181–199.
- [56] Daniel A Steck. “Rubidium 87 D line data”. In: (2001).
- [57] Wolfgang Ketterle and NJ Van Druten. “Evaporative cooling of trapped atoms”. In: *Advances in atomic, molecular, and optical physics*. Vol. 37. Elsevier, 1996, pp. 181–236.
- [58] I Lesanovsky et al. “Adiabatic radio-frequency potentials for the coherent manipulation of matter waves”. In: *Physical Review A. Atomic, Molecular, and Optical Physics* 73.3 (2006).
- [59] S Hofferberth et al. “Radiofrequency-dressed-state potentials for neutral atoms”. In: *Nature Physics* 2.10 (2006), pp. 710–716. DOI: <https://doi.org/10.1038/nphys420>. URL: <https://www.nature.com/articles/nphys420>.
- [60] Stefanie Manz et al. “Two-point density correlations of quasicondensates in free expansion”. In: *Physical Review A* 81.3 (2010), p. 031610.
- [61] G Reinaudi et al. “Strong saturation absorption imaging of dense clouds of ultracold atoms”. In: *Optics letters* 32.21 (2007), pp. 3143–3145.

- [62] Robert Bücker et al. “Single-particle-sensitive imaging of freely propagating ultracold atoms”. In: *New Journal of Physics* 11.10 (2009), p. 103039.
- [63] R Bücker et al. “Single-particle-sensitive imaging of freely propagating ultracold atoms”. In: *New Journal of Physics* 11.10 (Oct. 2009), p. 103039. DOI: 10.1088/1367-2630/11/10/103039. URL: <https://dx.doi.org/10.1088/1367-2630/11/10/103039>.
- [64] AG Basden, CA Haniff, and CD Mackay. “Photon counting strategies with low-light-level CCDs”. In: *monthly notices of the royal astronomical society* 345.3 (2003), pp. 985–991.
- [65] T. Berrada et al. “Integrated Mach–Zehnder interferometer for Bose–Einstein condensates”. In: *Nature Communications* 4.1 (June 27, 2013), p. 2077. ISSN: 2041-1723. DOI: 10.1038/ncomms3077. URL: <https://doi.org/10.1038/ncomms3077>.
- [66] Bernhard Rauer. *Non-equilibrium dynamics beyond dephasing: Recurrences and loss induced cooling in one-dimensional Bose gases*. Springer, 2019.
- [67] Anders Sørensen et al. “Many-particle entanglement with Bose–Einstein condensates”. In: *Nature* 409.6816 (2001), pp. 63–66. DOI: <https://doi.org/10.1038/35051038>.
- [68] AG Martin et al. “RF spectroscopy of trapped neutral atoms”. In: *Physical review letters* 61.21 (1988), p. 2431.
- [69] MR Andrews et al. “Observation of interference between two Bose condensates”. In: *Science* 275.5300 (1997), pp. 637–641.
- [70] Gh-S Paraoanu et al. “The Josephson plasmon as a Bogoliubov quasiparticle”. In: *Journal of Physics B: Atomic, Molecular and Optical Physics* 34.23 (2001), p. 4689.
- [71] Michael Gring. “Prethermalization in an isolated many body system”. PhD thesis. Technische Universität Wien, 2012.
- [72] Thomas Schweigler. “Correlations and dynamics of tunnel-coupled one-dimensional Bose gases”. In: *arXiv preprint arXiv:1908.00422* (2019).
- [73] Carlo Ottaviani et al. “Adiabatic splitting, transport, and self-trapping of a Bose-Einstein condensate in a double-well potential”. In: *Physical Review A* 81.4 (2010), p. 043621.
- [74] Anthony J Leggett and Fernando Sols. “On the concept of spontaneously broken gauge symmetry in condensed matter physics”. In: *Foundations of physics* 21.3 (1991), pp. 353–364.
- [75] Tiantian Zhang et al. “Squeezing oscillations in a multimode bosonic Josephson junction”. In: *arXiv preprint arXiv:2304.02790* (2023).
- [76] M. J. Steel and M. J. Collett. “Quantum state of two trapped Bose-Einstein condensates with a Josephson coupling”. In: *Phys. Rev. A* 57 (4 Apr. 1998), pp. 2920–2930. DOI: 10.1103/PhysRevA.57.2920. URL: <https://link.aps.org/doi/10.1103/PhysRevA.57.2920>.
- [77] Brian David Josephson. “Possible new effects in superconductive tunnelling”. In: *Physics letters* 1.7 (1962), pp. 251–253. DOI: [https://doi.org/10.1016/0031-9163\(62\)91369-0](https://doi.org/10.1016/0031-9163(62)91369-0).

- [78] Alexandre Avraamovitch Golubov, M Yu Kupriyanov, and E Il'ichev. "The current-phase relation in Josephson junctions". In: *Reviews of modern physics* 76.2 (2004), p. 411.
- [79] Milton Abramowitz and Irene A Stegun. *Handbook of mathematical functions with formulas, graphs, and mathematical tables*. Vol. 55. US Government printing office, 1968.
- [80] Tim Langen et al. "Experimental observation of a generalized Gibbs ensemble". In: *Science* 348.6231 (2015), pp. 207–211. DOI: <https://doi.org/10.1126/science.1257026>. URL: <https://www.science.org/doi/10.1126/science.1257026>.
- [81] Thomas Schweigler et al. "Decay and recurrence of non-Gaussian correlations in a quantum many-body system". In: *Nature Physics* 17.5 (2021), pp. 559–563. DOI: 10.1038/s41567-020-01139-2. URL: <https://www.nature.com/articles/s41567-020-01139-2>.
- [82] Matthias M Müller et al. "One decade of quantum optimal control in the chopped random basis". In: *Reports on Progress in Physics* 85.7 (2022), p. 076001.
- [83] Phila Rembold. "Quantum Optimal Control of Spin Systems and Trapped Atoms". PhD thesis. Universität zu Köln, 2022.
- [84] Julian Grond et al. "Optimal control of number squeezing in trapped Bose-Einstein condensates". In: *Physical Review A* 80.5 (2009), p. 053625.
- [85] Gamal M Mahmoud. "Periodic solutions of strongly non-linear Mathieu oscillators". In: *International journal of non-linear mechanics* 32.6 (1997), pp. 1177–1185.
- [86] Si-Cong Ji et al. "Floquet engineering a bosonic Josephson junction". In: *Physical Review Letters* 129.8 (2022), p. 080402. DOI: 10.1103/PhysRevLett.129.080402. URL: <https://journals.aps.org/prl/abstract/10.1103/PhysRevLett.129.080402>.
- [87] Izabella Lovas et al. "Many-body parametric resonances in the driven sine-Gordon model". In: *Phys. Rev. B* 106 (7 Aug. 2022), p. 075426. DOI: 10.1103/PhysRevB.106.075426. URL: <https://link.aps.org/doi/10.1103/PhysRevB.106.075426>.
- [88] Vittorio Giovannetti, Seth Lloyd, and Lorenzo Maccone. "Quantum-enhanced measurements: beating the standard quantum limit". In: *Science* 306.5700 (2004), pp. 1330–1336. DOI: 10.1126/science.1104149. URL: <https://www.science.org/doi/full/10.1126/science.1104149>.
- [89] Christian Gross et al. "Nonlinear atom interferometer surpasses classical precision limit". In: *Nature* 464.7292 (2010), pp. 1165–1169. DOI: <https://doi.org/10.1038/nature08919>. URL: <https://www.nature.com/articles/nature08919>.
- [90] Chris D Hamley et al. "Spin-nematic squeezed vacuum in a quantum gas". In: *Nature Physics* 8.4 (2012), pp. 305–308. DOI: <https://doi.org/10.1038/nphys2245>. URL: <https://www.nature.com/articles/nphys2245>.
- [91] Julian Grond et al. "Optimal control of number squeezing in trapped Bose-Einstein condensates". In: *Phys. Rev. A* 80 (5 Nov. 2009), p. 053625.

- DOI: 10.1103/PhysRevA.80.053625. URL: <https://link.aps.org/doi/10.1103/PhysRevA.80.053625>.
- [92] Georg Jäger et al. “Parametric-squeezing amplification of Bose-Einstein condensates”. In: *Phys. Rev. A* 92 (5 Nov. 2015), p. 053632. DOI: 10.1103/PhysRevA.92.053632. URL: <https://link.aps.org/doi/10.1103/PhysRevA.92.053632>.
- [93] M Lewenstein and Li You. “Quantum phase diffusion of a Bose–Einstein condensate”. In: *Physical Review Letters* 77.17 (1996), p. 3489. DOI: <https://doi.org/10.1103/PhysRevLett.77.3489>. URL: <https://journals.aps.org/prl/abstract/10.1103/PhysRevLett.77.3489>.
- [94] Juha Javanainen and Martin Wilkens. “Phase and phase diffusion of a split Bose-Einstein condensate”. In: *Physical Review Letters* 78.25 (1997), p. 4675. DOI: 10.1103/PhysRevLett.78.4675.
- [95] G-B Jo et al. “Long phase coherence time and number squeezing of two Bose-Einstein condensates on an atom chip”. In: *Physical Review Letters* 98.3 (2007), p. 030407.
- [96] Jürgen Berges, Sz Borsányi, and Christof Wetterich. “Prethermalization”. In: *Physical review letters* 93.14 (2004), p. 142002.
- [97] Yvan Castin and Jean Dalibard. “Relative phase of two Bose-Einstein condensates”. In: *Physical Review A* 55.6 (1997), p. 4330.
- [98] AJ Leggett and F Sols. “Comment on “phase and phase diffusion of a split Bose–Einstein condensate””. In: *Physical review letters* 81.6 (1998), p. 1344. DOI: <https://doi.org/10.1103/PhysRevLett.81.1344>. URL: <https://journals.aps.org/prl/abstract/10.1103/PhysRevLett.81.1344>.
- [99] Rafi Bistritzer and Ehud Altman. “Intrinsic dephasing in one-dimensional ultracold atom interferometers”. In: *Proceedings of the National Academy of Sciences* 104.24 (2007), pp. 9955–9959. DOI: <https://doi.org/10.1073/pnas.0608910104>. URL: <https://www.pnas.org/doi/full/10.1073/pnas.0608910104>.
- [100] I. E. Mazets, T. Schumm, and J. Schmiedmayer. “Breakdown of Integrability in a Quasi-1D Ultracold Bosonic Gas”. In: ().
- [101] Shina Tan, Michael Pustilnik, and Leonid I. Glazman. “Relaxation of a High-Energy Quasiparticle in a One-Dimensional Bose Gas”. In: *Phys. Rev. Lett.* 105 (9 Aug. 2010), p. 090404. DOI: 10.1103/PhysRevLett.105.090404. URL: <https://link.aps.org/doi/10.1103/PhysRevLett.105.090404>.
- [102] Rodrigo G. Pereira, Steven R. White, and Ian Affleck. “Exact Edge Singularities and Dynamical Correlations in Spin-1/2 Chains”. In: *Phys. Rev. Lett.* 100 (2 Jan. 2008), p. 027206. DOI: 10.1103/PhysRevLett.100.027206. URL: <https://link.aps.org/doi/10.1103/PhysRevLett.100.027206>.
- [103] Tim Langen et al. “Prethermalization in one-dimensional Bose gases: description by a stochastic Ornstein-Uhlenbeck process”. In: *The European Physical Journal Special Topics* 217 (2013), pp. 43–53. DOI: <https://doi.org/10.1140/epjst/e2013-01752-0>. URL: <https://link.springer.com/article/10.1140/epjst/e2013-01752-0>.

- [104] Takuya Kitagawa et al. “The dynamics and prethermalization of one-dimensional quantum systems probed through the full distributions of quantum noise”. In: *New Journal of Physics* 13.7 (2011), p. 073018. DOI: 10.1088/1367-2630/13/7/073018. URL: <https://iopscience.iop.org/article/10.1088/1367-2630/13/7/073018/meta>.
- [105] Takuya Kitagawa et al. “Ramsey interference in one-dimensional systems: the full distribution function of fringe contrast as a probe of many-body dynamics”. In: *Physical Review Letters* 104.25 (2010), p. 255302. DOI: <https://doi.org/10.1103/PhysRevLett.104.255302>. URL: <https://journals.aps.org/prl/abstract/10.1103/PhysRevLett.104.255302>.
- [106] Remi Geiger et al. “Local relaxation and light-cone-like propagation of correlations in a trapped one-dimensional Bose gas”. In: *New Journal of Physics* 16.5 (2014), p. 053034.
- [107] Tim Langen. *Non-equilibrium dynamics of one-dimensional Bose gases*. Springer, 2015.
- [108] Tim Langen, Thomas Gasenzer, and Jörg Schmiedmayer. “Prethermalization and universal dynamics in near-integrable quantum systems”. In: *Journal of Statistical Mechanics: Theory and Experiment* 2016.6 (June 2016), p. 064009. DOI: 10.1088/1742-5468/2016/06/064009. URL: <https://iopscience.iop.org/article/10.1088/1742-5468/2016/06/064009>.
- [109] Bess Fang et al. “Quench-Induced Breathing Mode of One-Dimensional Bose Gases”. In: *Phys. Rev. Lett.* 113 (3 July 2014), p. 035301. DOI: 10.1103/PhysRevLett.113.035301. URL: <https://link.aps.org/doi/10.1103/PhysRevLett.113.035301>.
- [110] H.-P. Stimming et al. “Fluctuations and Stochastic Processes in One-Dimensional Many-Body Quantum Systems”. In: *Phys. Rev. Lett.* 105 (1 July 2010), p. 015301. DOI: 10.1103/PhysRevLett.105.015301. URL: <https://link.aps.org/doi/10.1103/PhysRevLett.105.015301>.
- [111] George E Uhlenbeck and Leonard S Ornstein. “On the theory of the Brownian motion”. In: *Physical review* 36.5 (1930), p. 823.
- [112] Stefan Beck, Igor E. Mazets, and Thomas Schweigler. “Nonperturbative method to compute thermal correlations in one-dimensional systems”. In: *Phys. Rev. A* 98 (2 Aug. 2018), p. 023613. DOI: 10.1103/PhysRevA.98.023613. URL: <https://link.aps.org/doi/10.1103/PhysRevA.98.023613>.
- [113] A. Imambekov et al. “Density ripples in expanding low-dimensional gases as a probe of correlations”. In: *Phys. Rev. A* 80 (3 Sept. 2009), p. 033604. DOI: 10.1103/PhysRevA.80.033604. URL: <https://link.aps.org/doi/10.1103/PhysRevA.80.033604>.
- [114] Mohammadamin Tajik et al. *Experimental verification of the area law of mutual information in quantum field theory*. 2022. DOI: 10.48550/ARXIV.2206.10563. URL: <https://arxiv.org/abs/2206.10563>.
- [115] Tim Kovachy et al. “Matter wave lensing to picokelvin temperatures”. In: *Physical review letters* 114.14 (2015), p. 143004.

- [116] Christian Deppner et al. “Collective-Mode Enhanced Matter-Wave Optics”. In: *Phys. Rev. Lett.* 127 (10 Aug. 2021), p. 100401. DOI: 10.1103/PhysRevLett.127.100401. URL: <https://link.aps.org/doi/10.1103/PhysRevLett.127.100401>.
- [117] Saurabh Pandey et al. “Atomtronic Matter-Wave Lensing”. In: *Phys. Rev. Lett.* 126 (17 Apr. 2021), p. 170402. DOI: 10.1103/PhysRevLett.126.170402. URL: <https://link.aps.org/doi/10.1103/PhysRevLett.126.170402>.
- [118] Martino Calzavara et al. “Optimizing optical potentials with physics-inspired learning algorithms”. In: *Physical Review Applied* 19.4 (2023), p. 044090.
- [119] Federica Cataldini et al. “Emergent Pauli blocking in a weakly interacting Bose gas”. In: *Physical Review X* 12.4 (2022), p. 041032.
- [120] Marek Gluza et al. “Quantum field thermal machines”. In: *PRX Quantum* 2.3 (2021), p. 030310.